ABSTRACT

Title of Dissertation: CHARACTERIZATION OF NON-LINEAR
                         POLYMER PROPERTIES TO PREDICT
                         PROCESS INDUCED WARPAGE AND
                         RESIDUAL STRESS OF ELECTRONIC
                         PACKAGES

                         Yong Sun, Doctor of Philosophy, 2016

Dissertation directed by: Professor Bongtae Han
                            Department of Mechanical Engineering

Nonlinear thermo-mechanical properties of advanced polymers are crucial to accurate prediction of the process induced warpage and residual stress of electronics packages. The Fiber Bragg grating (FBG) sensor based method is advanced and implemented to determine temperature and time dependent nonlinear properties. The FBG sensor is embedded in the center of the cylindrical specimen, which deforms together with the specimen. The strains of the specimen at different loading conditions are monitored by the FBG sensor. Two main sources of the warpage are considered: curing induced warpage and coefficient of thermal expansion (CTE) mismatch induced warpage. The effective chemical shrinkage and the equilibrium modulus are needed for the curing induced warpage prediction. Considering various polymeric materials used in microelectronic packages, unique curing setups and procedures are developed for elastomers (extremely low modulus, medium viscosity, room temperature curing),

underfill materials (medium modulus, low viscosity, high temperature curing), and epoxy molding compound (EMC: high modulus, high viscosity, high temperature pressure curing), most notably, (1) zero-constraint mold for elastomers; (2) a two-stage curing procedure for underfill materials and (3) an air-cylinder based novel setup for EMC.

For the CTE mismatch induced warpage, the temperature dependent CTE and the comprehensive viscoelastic properties are measured. The cured cylindrical specimen with a FBG sensor embedded in the center is further used for viscoelastic property measurements. A uniaxial compressive loading is applied to the specimen to measure the time dependent Young's modulus. The test is repeated from room temperature to the reflow temperature to capture the time-temperature dependent Young's modulus. A separate high pressure system is developed for the bulk modulus measurement. The time temperature dependent bulk modulus is measured at the same temperatures as the Young's modulus. The master curve of the Young's modulus and bulk modulus of the EMC is created and a single set of the shift factors is determined from the time temperature superposition. The supplementary experiments are conducted to verify the validity of the assumptions associated with the linear viscoelasticity. The measured time-temperature dependent properties are further verified by a shadow moiré and Twyman/Green test.

CHARACTERIZATION OF NON-LINEAR POLYMER PROPERTIES TO PREDICT PROCESS INDUCED WARPAGE AND RESIDUAL STRESS OF ELECTRONIC PACKAGES

By

Yong Sun

Dissertation submitted to the Faculty of the Graduate School of the
University of Maryland, College Park, in partial fulfillment
of the requirements for the degree of
Doctor of Philosophy
2016

Advisory Committee:
Prof. Bongtae Han, Chair/Advisor
Prof. Abhijit Dasgupta
Prof. Patrick McCluskey
Prof. Hugh Bruck
Prof. Kyu Yong Choi

Acknowledgements

I have been helped by many people throughout my PhD study. I know that I may not be able to finish my PhD without the support from them. Although I could not mention everyone who helped me before, I'd like to express my gratitude to a few of them who have been particularly helpful and inspiring.

First and foremost, I would like to express my sincere thanks to my advisor, Dr. Bongtae Han, for giving the opportunity to work with him. I'm really grateful for the huge amount of time he spent with me to guide and inspire me. It was an exciting journey to pursue my PhD with Dr. Han. I'm sure that the valuable lectures and guidance he gave me will be also be greatly helpful for my future career.

Next, I would like to thank our LOMSS members. I thank Hyun-Seop and Michelle for their cooperation and assistance with my experiments. Bong-Min, Kenny, Dae-Suk, Bulong, Sean and Byung are also greatly appreciated for their support and company during my PhD journey.

I would like to thank the members of my dissertation committee, Dr. Abhijit Dasgupta, Dr. Patrick McCluskey, Dr. Hugh Bruck and Dr. Kyu Yong Choi. I really appreciate their valuable comments during my defense.

Finally, I wish to express my gratitude to my parents. I could not finish it without their support behind me. My most heartfelt thanks go to my beloved wife, Yinjun Huang, for her kindness, encouragement and endless support.

Table of Contents

List of Figures

vii

Chapter 1 Motivation and Objective

1.1. Motivation

The warpage and residual stress issues are two important challenges in reliability of current microelectronics packaging. The deviation from the uniform flatness of the IC package may cause the open or shortage of the circuit connection. The residual stress can affect the products' performance by introducing warpage, delamination and even die crack [1-6].

The ball grid array (BGA) packages are typically more susceptible to the warpage during solder reflow since it may cause the open or bridge between adjacent solders as illustrated in Figure 1.1. The JEDEC standard specifies that the coplanarity of the BGA package must be under 6 mils (150 μm) [7]. The warpage issue is becoming more important due to the current trends in industry: a larger package size leading to a large DNP (distance to the neutral point) [8]; green molding compound with higher filler contents [2] and coreless substrate[9].

Solder open   Solder bridge

Figure 1.1 Warpage caused failure of the BGA package

Another important form of package related to the warpage challenge is the package on package (PoP) [10-12]. PoP is a packaging method to stack two or more BGA packages atop each other with standard interface to route signals between them.

It is reported that about 90% of the PoP defects are caused by warpage during solder reflow [13]. The package stack goes through a single reflow, and thus, it is very important to match the warpage of the top and bottom packages. The top and bottom packages should have the same shape of warpage to ensure good quality during reflow as illustrated in Figure 1.2. Typically, the bottom package is a single die BGA and the top package is a multiple die BGA. The mismatch of the warpage between the top package and the bottom package will easily introduce solder opening or bridging.
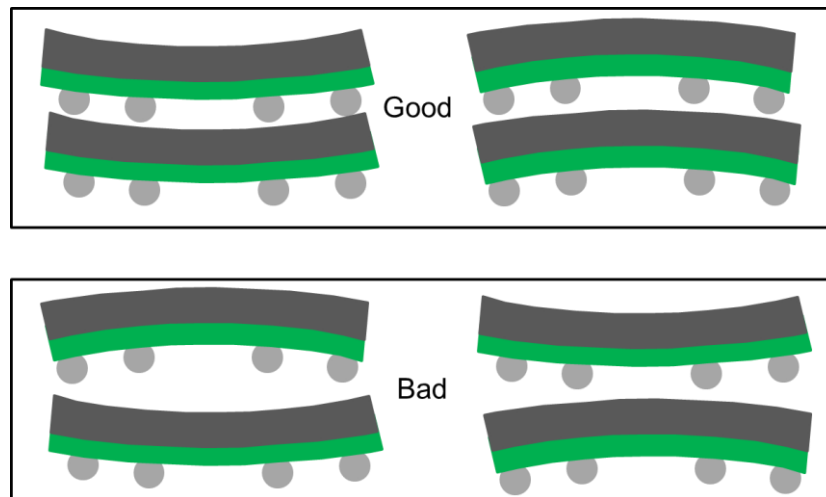
Figure 1.2 Warpage challenge in the PoP

The electronic device becomes thinner and thinner for the mobile application and the warpage issue becomes the main challenge. With the shorter design cycle of the products, an effective and efficient way to predict the warpage for the design and manufacturing process optimization are critically needed. The accuracy of the prediction heavily depends on the properties input of the materials, especially the nonlinear properties of the polymeric materials.

The warpage of a package is usually introduced by two processes: the curing shrinkage of the polymeric material [14-16] and the CTE mismatch of the different

materials during various thermal processes [3, 17-19]. During curing of the polymer, the volume shrinks while the modulus begins to develop. The chemical shrinkage and the modulus evolution will build up residual stress and warpage in the package [20, 21]. After curing the packages have to go through various thermal processes during manufacturing, such as post curing, solder reflow, and cooling down to room temperature. These processes will induce large warpage and residual stress in the package due to the CTE mismatch between different components in the package [7, 22].

1.2. Objective

The objective of this thesis is to develop a technique to predict the warpage and residual stress of the package at different stages by characterizing the non-linear properties of polymeric materials used in the packages. Achieving the objective entails:

a) Characterize the curing properties of various polymeric materials used in microelectronics packaging; considering the distinctive curing conditions and curing properties of the different polymeric materials used in packages, customized curing setup and procedures need to be developed targeting different polymers.

b) Develop a methodology to determine the comprehensive viscoelastic properties of polymeric materials by measuring two time-temperature dependent elastic constants (e.g., bulk modulus and Young's modulus) for the accurate warpage prediction during the temperature change;

c) Investigate the assumptions associated with the linear viscoelastic theory by experiments; linear viscoelasticity is applicable to certain types of polymers with the assumptions that need to be verified.

d) Design test vehicles to verify the measured properties; the measured the properties are used as inputs for the prediction of the warpage and residual stress.

1.3. Organization of Dissertation

This dissertation consists of five chapters. Chapter 1 presents the motivations of the work and lists the four main objectives.

Chapter 2 introduces the background of the dissertation. The two main sources of the warpage and residual stress are discussed in this chapter. The properties needed for the accurate prediction are also discussed in the chapter. The existing techniques for the critical properties measurement are reviewed in the literatures.

Chapter 3 presents the proposed curing properties measurement techniques for three different polymeric materials: silicone elastomer, underfill and epoxy molding compound. The silicone elastomer has low modulus after curing and requires relatively low curing temperature. A large configuration was proposed and a novel setup utilizing a thin plastic wrap was used to hold an uncured specimen. The underfill material has medium modulus but large heat generation during curing. A two-step curing procedure was proposed with a silicone tube to hold an uncured specimen at the first step. The tube was taken off in the second step to ensure free curing of the specimen. The EMC material requires high temperature and high pressure for curing. A novel setup was

developed to accommodate the high temperature and pressure curing condition. The surface of the specimen was also treated to ensure free curing of the specimen.

Chapter 4 focuses on the proposed technique for the properties measurement. The cured specimen from Chapter 3 was further utilized for the viscoelastic properties measurements. The time-temperature dependent Young's modulus and bulk modulus were measured using a single configuration. The uniaxial compressive loading was applied for the Young's modulus measurement. A high pressure system was developed to apply hydrostatic gas pressure to the specimen for the bulk modulus measurement. The master curve was created using time-temperature superposition. A single set of shift factors was fitted by a piecewise shift function. The assumptions associated with the linear viscoelasticity were investigated by supplementary experiments. Shadow moiré and Twyman/Green test were developed to measure the rate dependent warpage of a bi-material specimen. The measured warpage was compared with the predicted value to verify the properties.

Chapter 5 is the summary and contribution of the dissertation. The future work of this topic is also presented in the chapter.

Chapter 2 Background and Literature Review

2.1. Background

Various polymeric materials are used in electronic packaging: epoxy molding compounds (EMC) are used as a protection layer for the IC and die; underfill materials are applied to redistribute the residual stress in the solder layer of the flip-chip package; silicone elastomers are used as potting material for encapsulating electronics. During the curing process, the polymeric material changes from liquid to solid. The volumetric reduction (or chemical shrinkage) and the modulus evolution occur during the phase change process due to a chemical reaction. As a result, residual stress and warpage are built up within the package. After the curing of the polymeric material, the packages go through various thermal processes, such as post curing, solder reflow and etc. Due to the different CTE values between the die, polymeric layer and the substrate, large residual stress and warpage can also be introduced during these processes. Figure 2.1 illustrates the warpage introduced during the molding transfer and solder reflow process. The temperature profile and the EMC volume change is shown in Figure 2.1(a). During the molding transfer, the temperature is constant and the volume of the EMC shrinkages, causing the warpage of the package as shown in Figure 2.1(b). During the solder reflow, the temperature changes and the CTE mismatch introduces warpage to the package. After reflow, the cooling down process can also introduce warpage due to the CTE mismatch. These process induced residual stress and warpage can affect the reliability of the microelectronics products [23-25].
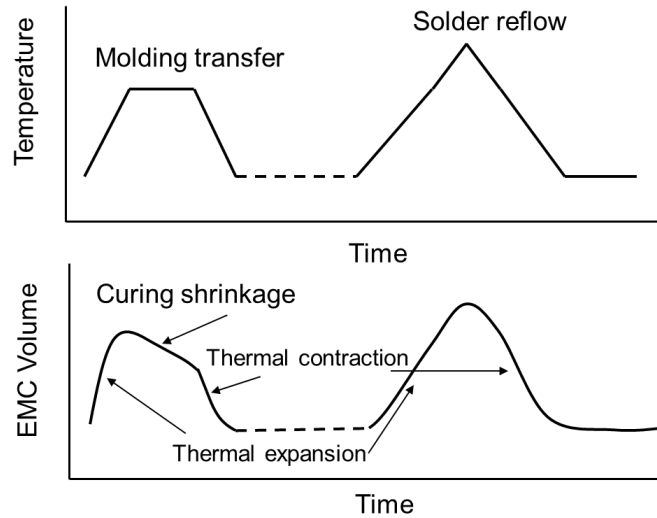
(a)
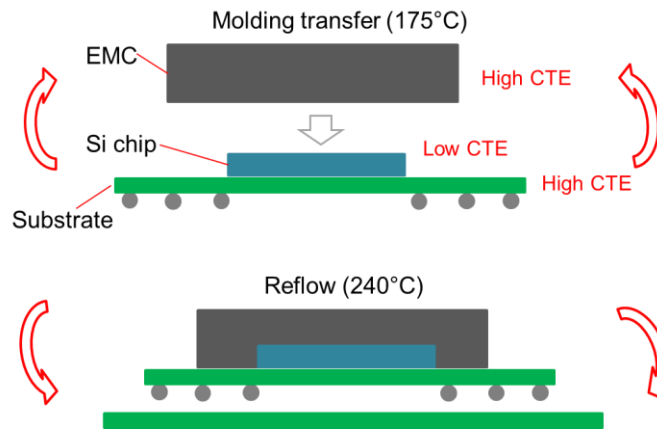
(b)

Figure 2.1 Warpage introduced during molding transfer and solder reflow (a) temperature profile (b) warpage

In order to optimize the design and the manufacturing process, accurate prediction of the process induced warpage and residual stress is required. The accurate non-linear polymer properties are needed to be able to predict the warpage and residual stress. The critical properties obtained during or after curing are the volume shrinkage (or chemical shrinkage) and the equilibrium modulus of the polymer, which is defined

7

as the modulus after curing. During the temperature change process, the comprehensive viscoelastic properties of the polymeric materials, the temperature dependent CTE and glass transition are also required for the prediction. The literature review of the property characterization during the two processes is presented in the following section.

2.2. Literature review

2.2.1. Curing properties measurement

In microelectronics packaging, the most widely used polymeric materials are the thermosetting polymers, which cures irreversibly [26, 27]. During the curing of the thermoset, the single polymer chains crosslink with each other creating the fishnet structure. The bonds between the chains change from van der Waals force to the covalent bonding [28]. The total volume of the structure reduced and the modulus develops during the curing process [29].

Chemical shrinkage occurs at the beginning of the curing as the distance between the molecules changes during crosslinking. Modulus starts to evolve after the gelation point. The evolution properties of a typical material system are illustrated in Figure 2.2, which defines schematically the chemical shrinkage evolution, $\varepsilon(t)$; the effective chemical shrinkage evolution, $\varepsilon^{eff}(t)$, defined as the chemical shrinkage accumulated after the gelation point t_{gel}, before which the modulus is "zero"; and the modulus evolution, $E(t)$, after the gelation point. For the purpose of illustration, the shrinkage and the modulus are normalized by the total chemical shrinkage, ε_{∞}, and the

equilibrium modulus, E_∞, respectively, and the time axis is shown in an arbitrary unit. Before the gelation point, no residual stress can be developed because of the zero modulus; after the gelation point, all chemical shrinkage contributes to the development of residual stresses [21, 30].
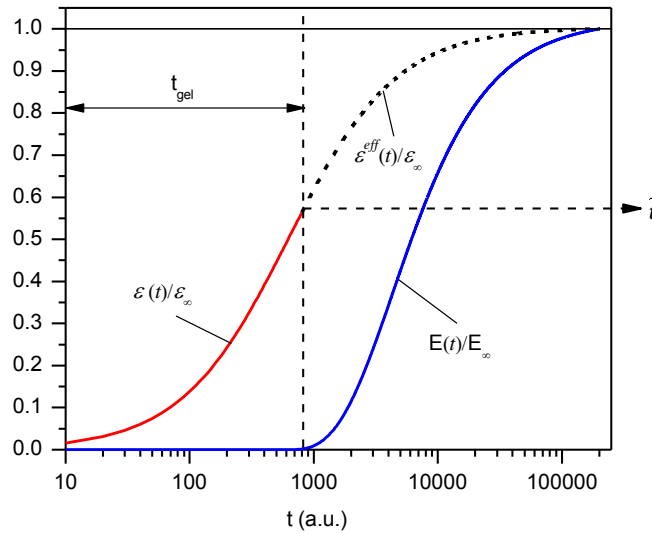
Figure 2.2 Illustration of property evolution in a typical polymer system[21]

Numerous testing methods have been developed for the measurement of the chemical shrinkage. The dilatometer is the most commonly practiced method [1, 31-36], which has been practiced for measuring the shrinkage of different polymeric materials. The advantage of the dilatometer is the direct measurement of the volume change as a function of temperature and pressure. However, the system is relatively complicated and some the toxic materials are used in the system. A laser scanning micrometer was implemented to monitor the length of a polymer specimen during curing [35]. It only applies to the light curing polymers due to the complex optical setup even though it has high accuracy in the length measurement. A gas pycnometer was used to measure the shrinkage of the dental composites [37]. Due to the lack of

9

the active temperature control system, this system cannot maintain the constant curing temperature. The in-situ monitoring the curing shrinkage was realized by an optical fiber sensor during injection molding [38]. Using the cross section analysis technique, the curing shrinkage of the UV-cured adhesives was measured [39]. The uncertainty in the volume determination could introduce significant error to the results. The chemical shrinkage of two epoxy-based NCA materials was studied using a Thermo-mechanical Analyzer (TMA)[40]. However, constant loading was applied to the specimen during curing, which could affect the measured shrinkage. A moiré method was implemented to measure the curing properties of the polymer material with some assumptions [41]. It should be noted that all the methods above only measures the total chemical shrinkage, which includes the shrinkages before the gelation point. Using the total chemical for the prediction would overestimate the warpage and the residual stress [42].

After measuring the total chemical shrinkage (or effective chemical shrinkage) and equilibrium modulus, the residuals stress and warpage was predicted[1, 3, 7, 15, 31, 32, 43, 44]. Only the final value of the shrinkage and modulus were used in these cases. Therefore, only the final warpage is to be predicted. The curing induced strain was assumed to be elastic by curing the polymer above the glass transition temperature [43, 44]. The curing process should also be isothermal in order to eliminate the effect of the thermal expansion. The properties evolution during the curing was not considered in these cases.

The effective chemical shrinkage has also been measured by the bi-material strip [15]. By curing the polymer on top of the substrate, the whole assembly will warp only after the polymer layer starts to develop the warpage. By measuring the warpage

of the assembly, the effective chemical shrinkage can be determined. The gelation point during the curing process can also be determined [40, 45]. For the EMC curing, high pressure and high temperature is needed for the cuing requirement, which is not practical to be done by the biomaterial strip.

The chemical shrinkage and modulus evolution are measured to predict the warpage and the residual stress evolution during the whole curing process [42, 46-48]. It is assumed that the curing process is elastic in these studies. The curing dependent viscoelastic properties were measured for the accurate prediction of the warpage and residual stress [17, 18, 49-53] evolution during curing. The curing dependent viscoelastic model can be used for the isothermal and non-isothermal curing. The time-temperature-conversion superposition model is applied. It should be noted that the curing-time-temperature dependent properties are very difficult to measure experimentally. The special setup was design to measure the modulus at different curing stages [17, 18, 49]. The time-temperature dependent modulus of the polymer at different curing stages was measured by DMA [52-54]. The curing dependent CTE and the shrinkage also have to be measured independently in these studies, which hasn't been presented.

2.2.2. Viscoelastic properties measurement

The viscoelasticity modeling of the polymeric materials is summarized in Figure 2.3. The time dependent mechanical properties are measured at each temperature first. Adopting the assumption of thermorheologically simple (TRS) [55] - all the relaxation time is equally affected by temperature - the time dependent data at different temperatures are shifted and overlapped by time-temperature superposition

and the shift factors and the master curve at the reference temperature are subsequently determined. The shift factors are fitted to a shift function and the master curve is fitted to a prony series. The coefficients of the shift function and the master curve are the inputs for the viscoelastic modeling.
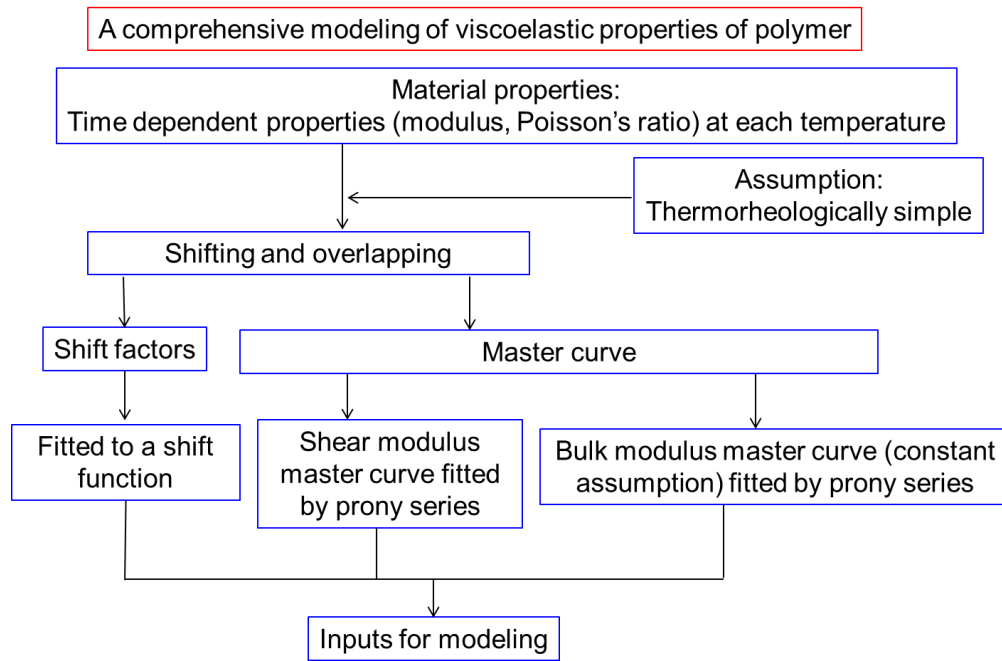
Figure 2.3 Flowchart for viscoelasticity modeling

The thermorheologically simple (TRS) assumption is used to shift and overlapping the time dependent data to the reference temperature. It has been argued that this assumption is not always valid for the certain polymers [55-60]. Even though the EMC is treated as the TRS material, there is not enough data in the literature to validate this assumption. With more and more EMC using different epoxy resin coming out, clear and evident experimental results are needed to further confirm that the EMC used for modelling is truly TRS material.

12

Another important assumption is the linear viscoelastic assumption, which means the model should be in the small strain range and the time dependent modulus should be independent of the applied stress. If the stress level is large enough, the linear viscoelastic assumption will no longer be valid [60, 61].

The constitutive relation of the viscoelasticity which is derived from the Boltzmann superposition principle is [62]:

$$s_{ij}(t) = 2\int G(t-\tau)\frac{\partial e_{ij}(\tau)}{\partial\tau}d\tau$$
$$\sigma_{kk}(t) = 3\int K(t-\tau)\frac{\partial\varepsilon_{kk}(\tau)}{\partial\tau}d\tau \tag{2.1}$$

where s and e is the deviatoric stress and strain, σ and ε is the dilatational stress and strain, G and K are the shear modulus and the bulk modulus. In order to have a comprehensive viscoelastic model of the polymer, two of the four time-temperature dependent properties are to be measured experimentally: they include Young's modulus $E(T,t)$, Poisson's ratio $\nu(T,t)$, bulk modulus $K(T,t)$ and shear modulus. The four elastic constants have the following relationships [63]:

$$K(T,t) = \frac{E(T,t)G(T,t)}{9G(T,t)-3E(T,t)}, \quad G(T,t) = \frac{E(T,t)}{2(1+\nu(T,t))} \tag{2.2}$$

In order to conduct the comprehensive viscoelastic modelling, at least two of the four constants have to be measured experimentally.

For simplicity, it has been often assumed that the bulk modulus is time-independent [64-66] based on the fact that the viscosity only affects the shear motion of the solid [65]. With this assumption, only one of the four time temperature

dependent properties has to be measured for viscoelastic modelling. Young's modulus is usually a preferred choice as it is relatively easy to measure.

The time and temperature dependent Young's modulus has been routinely measured by DMA. The temperature and frequency sweeping [67-69] produces a master curve and the corresponding shift factors. If the Poisson's ratio at room temperature (20 °C) is known, the bulk modulus can be approximated as:

$$K(T,t) \approx K = \frac{E(T = 20°C, t = 0)}{3(1 - 2\nu(T = 20°C, t = 0))} \tag{2.3}$$

It should be noted that the assumption of "time-independent" bulk modulus implies that the bulk modulus also becomes temperature-independent if the EMC is thermorheologically simple [70, 71]. Using the constant K value, the master curve of the shear modulus can be calculated from:

$$G(T,t) = \frac{3K \cdot E(T,t)}{9K - E(T,t)} \tag{2.4}$$

It has been known that the assumption of time-independent bulk modulus is not valid for EMC materials over a large temperature range, especially around the glass transition temperature [63, 72]. This poses challenges in predicting the warpage of packages at the solder reflow temperature, which is much higher than the glass transition of the EMC. This issue becomes more critical as the package on package (PoP) is more widely used, which has to go through several reflow cycles.

The effect of the time-independent bulk modulus assumption on the Young's modulus is shown in Figure 2.4. The Figure 2.4(a) shows the time dependent shear modulus and the Figure 2.4(b) shows the time independent and dependent bulk modulus. Using the Eq.(2.4), the time dependent Young's modulus is calculated for

the two cases. The maximum error of Young's modulus can be as large as 15%. In order to have the accurate prediction of the thermal process induced warpage and residual stress, the comprehensive viscoelastic properties of the polymeric materials should be determined by measuring two of the four time-temperature dependent properties.
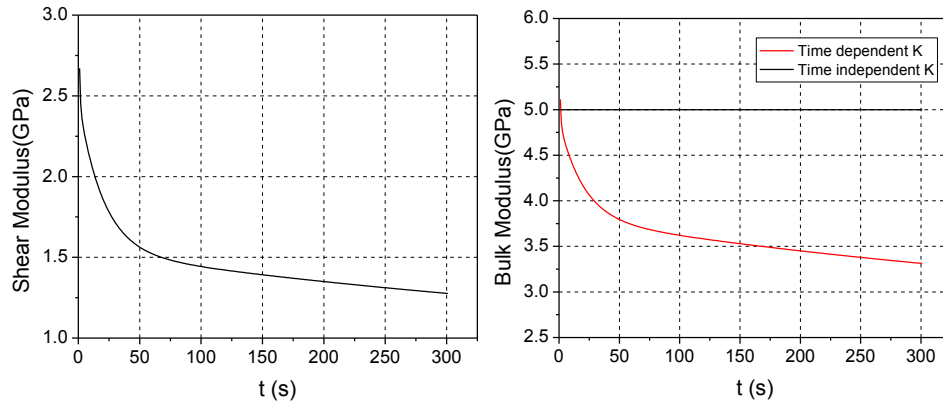
(a)

(b)
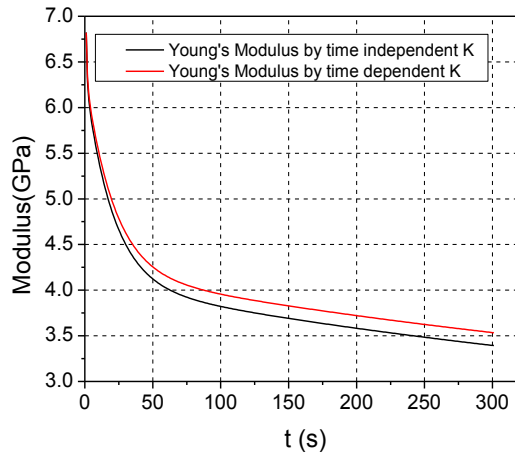
(c)

Figure 2.4 The effect of the time-independent bulk modulus assumption (a) share modulus (b) bulk modulus (c) Young's modulus

The single shift function is commonly practiced for the shift factors. The Arrhenius equation is an empirical equation that can be used for the temperature below

15

the glass transient temperature [73]. The WLF function was developed based on the free volume theory [74] and it has been shown that the WLF function is only strictly applicable in the glass transition range [75]. The polynomial function is also applied as the shift function [76], but it lacks physical meaning. The shift function introduced error is illustrated in Figure 2.5. The figure on the left shows shift factors and the fitted WLF function. Three temperatures are used for the comparison between the experiment data and the shifted data by the shift function. At 28.9 °C and 106°C, the overlapping is relatively good. At 135.8°C, the deviation of the shift function from the shift factors could introduce an error of as much as 50%. The results indicate that the single shift function could not fit the shift factors very well and the predicted modulus will not be accurate.
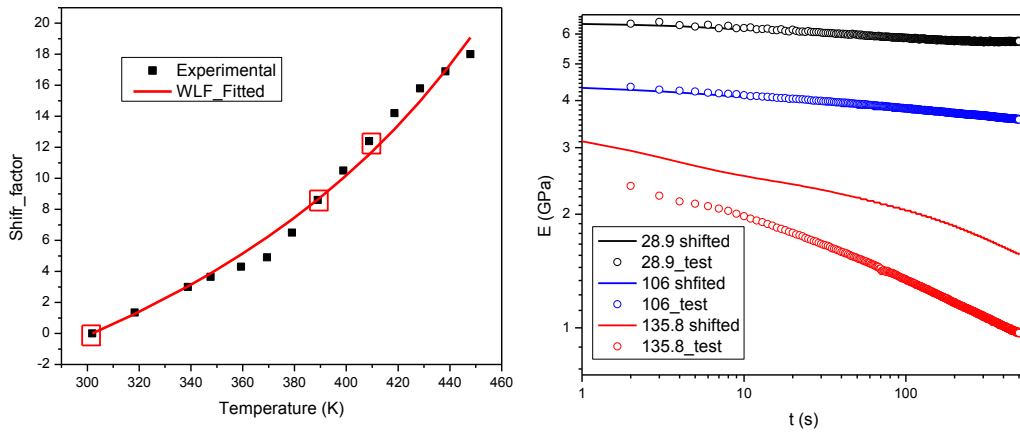
Figure 2.5 shift function introduced error

There were several attempts to measure two properties required for a viscoelastic analysis. In Ref. [63], the time and temperature dependent Young's modulus and Poisson's ratio were measured by strain gauges, from which the bulk modulus and the shear modulus were calculated. The measured data showed

fluctuations caused by the undesired reinforcement of the strain gauge, especially at high temperatures where the modulus was relatively low.

A full-field displacement measurement technique called moire interferometry was employed to measure the axial and transverse strains simultaneously [72], from which the time and temperature dependent Young's modulus and Poisson's ratio were determined. Its practice has been limited due to the stringent requirement of surface preparation including replication of a high frequency diffraction grating.

The frequency-temperature sweeping of DMA was implemented to measure the time and temperature dependent Young's modulus and shear modulus [77]. This technique is time consuming, albeit not impractical. In addition, it is usually very difficult to fabricate test coupons for the shear modulus.

The bulk modulus of the polymer can be measured by the dilatometer [78, 79] using a fluid pressure. The volume change of the polymer is monitored as a function of time after the pressure is applied and the bulk compliance of the polymer is determined. As mentioned in [79], when working at temperature above T_g, the weight of a rod adds undesired additional creep loading to the specimen, which causes to underestimate of the true volume change of the specimen.

The Fiber Bragg Grating (FBG) sensor has been used effectively to characterize the thermal mechanical properties of polymers [20, 80-84]. In the method, an FBG is embedded at the center of a cylindrical specimen. Thermal loading [81] or volumetric shrinkage loading [20, 83] were applied and the properties were determined from the Bragg wavelength (BW) change of the FBG using the predetermined relationship based on the generalized plane strain condition. The FBG method can be further implemented

17

to measure the comprehensive viscoelastic properties of the EMC. A very high hydrostatic pressure is required for the bulk modulus measurement. A new governing equation for a general loading should be developed. The major developments to accommodate the unique requirements of EMC testing are described and the results obtained from implementation with advanced EMC materials are presented.

Chapter 3 Curing Induced Warpage and Residual Stress

The curing properties of three polymers with very different curing conditions and properties are measured by the Fiber Bragg Grating (FBG) method:

- Silicone elastomer: low modulus, low curing temperature, fluid before curing

- Underfill: medium modulus, high curing temperature, fluid before curing

- EMC: high modulus, high curing temperature, high pressure, solid before curing

These polymeric materials are all widely used in electronic packaging. Considering their different curing requirements, different experiment setup and curing procedures are developed. The FBG is used as a strain sensor in our application. The basic principle of the FBG sensors is introduced in the first part. The silicone curing setup and procedure is presented in the second part of this chapter. The third part and the fourth part talk about the underfill curing and EMC curing experiments.

3.1. Fiber Bragg Grating as a Sensor

The Fiber Bragg Grating (FBG) has been used as a sensor for strain measurement for various materials, most notably composite materials [29, 83, 85-92]. The FBG was embedded in the structure to measure strain caused by thermal expansion [85, 86, 91], moisture absorption [88, 89, 93] and curing [83, 90, 92]. A cylindrical configuration was adopted most widely due to its mathematical simplicity [29, 88, 90, 92, 93].

A fiber Bragg grating is formed by a periodic perturbation of refractive index along the fiber length, which is typically created by the exposure to the intense interference pattern of UV energy [94-96]. When a band of the incident light encounters a material of higher index refraction, some of the incident light is reflected and some is transmitted. As shown in Figure 3.1, only small portion of the incident light can be reflected and the peak of the reflected light is called the Bragg wavelength which should satisfies [94-96]

$$\lambda = 2n_{eff}\Lambda \tag{3.1}$$

where λ is the Bragg wavelength, n_{eff} is the effective refractive index and Λ is the grating pith. Each grating serves to reflect a portion of the light signal and the total amount of the light reflected is dependent on the perturbed refractive index and the total grating length.

The grating pitch Λ and the effective refractive index n_{eff} can be changed due to the external disturbances such as the strain and temperature, resulting in the shifting of the Bragg wavelength. This is the basic principle of using FBGs as a sensor or temperature sensor.

The Equation (3.1) can be differentiated,

$$\frac{\Delta\lambda}{\lambda} = \frac{\Delta\Lambda}{\Lambda} + \frac{\Delta n_{eff}}{n_{eff}} = \varepsilon_1 + \frac{\Delta n_{eff}}{n_{eff}} \tag{3.2}$$

where $\Delta\Lambda$ and Δn_{eff} are the changes in the grating pitch and the effective refractive index respectively, and ε_1 is the axial strain along the fiber. For the isotropic and straight Bragg grating, the effective refractive index change can be expressed as[97],

$$\Delta n_{eff} = -\frac{n^3}{2}\left[P_{12}\varepsilon_1 + (P_{11} + P_{12})\varepsilon_2 - \left\{\frac{2}{n^3}\frac{dn}{dT} + (P_{11} + 2P_{12})\alpha_f\right\}\Delta T\right] \tag{3.3}$$

where ε_2 is the transverse strain, P_{ij} are strain-optical coefficients (Prockel's coefficients), $\frac{dn}{dT}$ is the thermal-optical coefficient, α_f is the CTE of the fiber core material, and ΔT is the temperature change. For the uni-axial loading where $\varepsilon_2 = -\nu\varepsilon_1$ with no temperature change, Equations (3.2) and (3.3) can be simplified as

$$\Delta\lambda = \lambda(1 - P_k)\varepsilon_1 \tag{3.4}$$

where P_k is defined as $P_k = -\frac{n^2}{2}\left[P_{12} - \nu(P_{11} + P_{12})\right]$, ν is the Poisson's ratio of the fiber material. Equation (3.4) shows the linear relationship between the applied strain and the BW change.
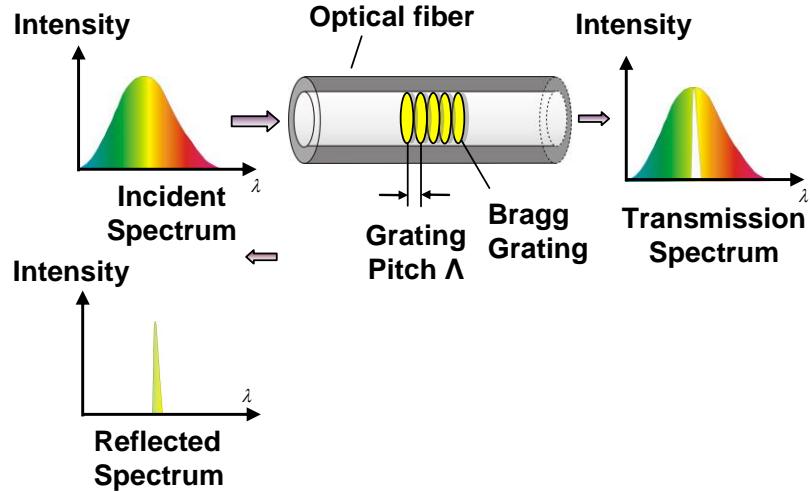
Figure 3.1 Illustration of an FBG spectrum reflection and transition [29]

When both temperature and mechanical loading are incorporated in the grating, the total BW shift can be expressed as:

$$\Delta \lambda = \Delta \lambda_i + \Delta \lambda_d \tag{3.5}$$

Where $\Delta \lambda_i$ is the BW change by the temperature; $\Delta \lambda_d$ is the BW change caused by the mechanical loading. They can be expressed as[20, 98]:

$$\Delta \lambda_i = \lambda_d \left[\left(\alpha_f + \frac{1}{n_{eff}} \frac{dn}{dT} \right) \Delta T + \frac{1}{n_{eff}} \frac{dn}{dT} \cdot \alpha_f \Delta T^2 \right] \tag{3.6}$$

$$\Delta \lambda_d = \frac{1}{E_f} \left\{ \left[1 - \frac{n^2}{2} \left(P_{12} - (P_{12} + P_{11}) \upsilon_f \right) \right] \sigma_{zz}^f - \left[2\upsilon_f + \frac{n^2}{2} \left((1-\upsilon_f) P_{11} + (1-3\upsilon_f) P_{12} \right) \right] \sigma_{rr}^f \right\} \lambda$$

$$\tag{3.7}$$

The material properties can be inversely calculated from the measured deformation induced BW shift based on the analytical relationship between BW shift and the material properties.

The specimen configuration of the FBG technique is illustrated in Figure 3.2, where the radius of the fiber is r_f and the outer radius of the polymer is r_s. The effective chemical shrinkage can be modeled as a piecewise loading condition of

$$\varepsilon_{loading} = \begin{cases} 0 & \text{for } 0 \leq r < r_f \\ \tilde{\varepsilon} & \text{for } r_f < r \leq r_s \end{cases} \tag{3.8}$$

where $\tilde{\varepsilon}$ is the strain of the polymer caused by the effective chemical shrinkage.
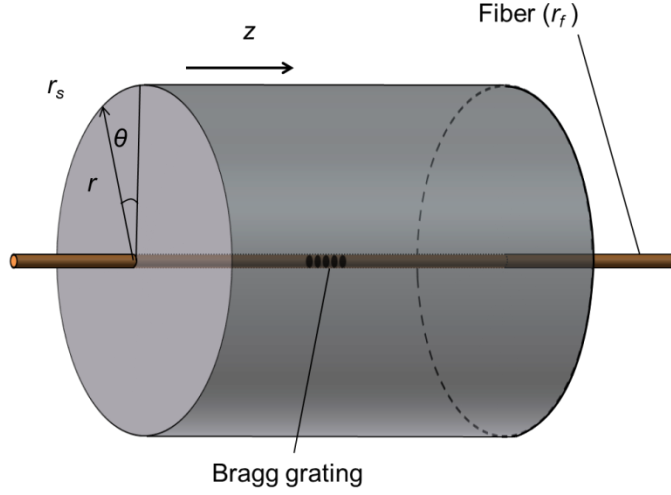
Figure 3.2 Schematic diagram of an FBG sensor embedded in a cylindrical substrate

The generalized plane strain solution of stress components of the fiber can be expressed as[20, 98]:

$$\sigma_{rr}^f = \sigma_{\theta\theta}^f = \frac{E_f}{1+v_f} \cdot \frac{C_{1f}}{1-2v_f}$$

(3.9)

$$\sigma_{zz}^f = \frac{2v_f E_f C_{1f}}{\left(1+v_f\right)\left(1-2v_f\right)} + \frac{\left(\dfrac{r_s^2}{r_f^2}-1\right)\left[\dfrac{E_s}{1-v_s}\Delta\varepsilon - \dfrac{2v_s E_s C_{1s}}{\left(1+v_s\right)\left(1-2v_s\right)}\right] - \dfrac{2v_f E_f C_{1f}}{\left(1+v_f\right)\left(1-2v_f\right)}}{1+\dfrac{E_s}{E_f}\left(\dfrac{r_s^2}{r_f^2}-1\right)}$$

(3.10)

where σ_{zz}^f, σ_{rr}^f and $\sigma_{\theta\theta}^f$ are the axial, radial and hoop stress components of the fiber, respectively; E_f and v_f are the modulus and Poisson's ratio of the fiber material; and E_s, v_s are the modulus and Poisson's ratio of the polymer. The detailed descriptions of the coefficients C_{1f} and C_{1s} can be found in Ref.[20].

23

By substituting Eqs. (3.9) and (3.10) into (3.7), the BW shift can be expressed as

$$\lambda_d = F\left(E_s, \beta\right) \cdot \tilde{\varepsilon} \tag{3.11}$$

where $\beta = \dfrac{r_s}{r_f}$ (will be referred to as "configuration"); and $F\left(E_s, \beta\right)$ is a nonlinear function that can be expressed explicitly [20].

3.2. Silicone elastomer curing

The fiber Bragg grating sensor (FBGS) technique is employed to measure two critical properties of an elastomer to evaluate the residual stress in a potted electronic system: total effective chemical shrinkage and equilibrium modulus. The elastomer has an extremely low modulus, which poses new technical challenges in implementing the FBGS technique. In order to achieve a sufficient Bragg wavelength shift, a very large configuration is needed for the experiment. The large configuration can generate excessive heat during curing and affect the Bragg wavelength measurement. In addition, the free-edge effect also has to be investigated for the required large configuration. A systematic way to overcome these challenges is presented. The equilibrium modulus is measured first directly from the cured specimen. Then the total effective chemical shrinkage is determined from the BW shift documented during curing. The measured total effect chemical shrinkage is confirmed by a test with a different configuration. The assumption made for the measurement of the equilibrium modulus is also validated by a conventional tension test. Using the properties as input variables, the residual stress of a potted electronic system is calculated by FEM.

3.2.1. Configuration selection

It is clear from Eq. (3.11) that a larger configuration will produce a higher BW shift signal. The exothermic heat is one of the most critical properties to be considered for the configuration selection as excessive heat can cause non-uniform curing and thus non-uniform property. The following analysis is conducted to quantify the effect.

The governing equation of the combined curing and heat generation can be expressed as[20]:

$$\frac{k}{\rho}\left(\frac{\partial^2 T}{\partial r^2} + \frac{1}{r}\frac{\partial T}{\partial r}\right) + \frac{dp}{dt}\Delta H = c_p \frac{\partial T}{\partial t} \tag{3.12}$$

where k is the thermal conductivity, ρ is the density, c_p is the specific heat, T is the temperature, ΔH is the exothermic heat per unit mass, and p is the curing extent.

The nth order curing kinetics model is used for the simulation, which can be expressed as [21, 99, 100]:

$$\frac{dp}{dt} = K_c(1-p)^n \tag{3.13}$$

where K_c is a temperature-dependent reaction rate coefficient; and n is a reaction order. Then, Eq.(3.13) becomes:

$$\frac{k}{\rho}\left(\frac{\partial^2 T}{\partial r^2} + \frac{1}{r}\frac{\partial T}{\partial r}\right) + K_c(1-p)^n \Delta H = c_p \frac{\partial T}{\partial t} \tag{3.14}$$

The exothermic heat was first measured by a differential scanning calorimeter (Pyris-1: PerkinElmer). The results (heat flow and temperature profile) obtained from a constant ramping rate test (1 ℃/min) are shown in Figure 3.3. The silicone elastomer cured completely around 100 ℃. The total exothermic heat was determined from the plot by calculating the area between the specimen heat flow and the reference heat flow.

Then the exothermic heat per unit mass was calculated by dividing it by the mass: $\Delta H = 5.5 \text{ J/g}$. The typical properties of silicone materials were used for Eqs. (3.14):

$\rho = 1300 \text{ kg/m}^3$, $k = 1.25 \text{ W/k m}$, $c_p = 1400 \text{ J/kg k}$ and $K_c = 0.00135$.

The results of the thermal analysis using the standard fiber ($r_f = 125 \,\mu\text{m}$) are shown in Figure 3.4, where the temperature difference between the center and the edge after curing is plotted as function of configuration. As expected from the low exothermic heat, the temperature difference was not significant. A configuration with a large β is possible considering a typical temperature measurement accuracy of 0.5 °C. After taking the uncertainties in the curing kinetics constants assumed in the simulation into consideration, a configuration of $\beta = 100$ is selected for experiments, which is expected to produce the temperature difference less than 0.4 °C.
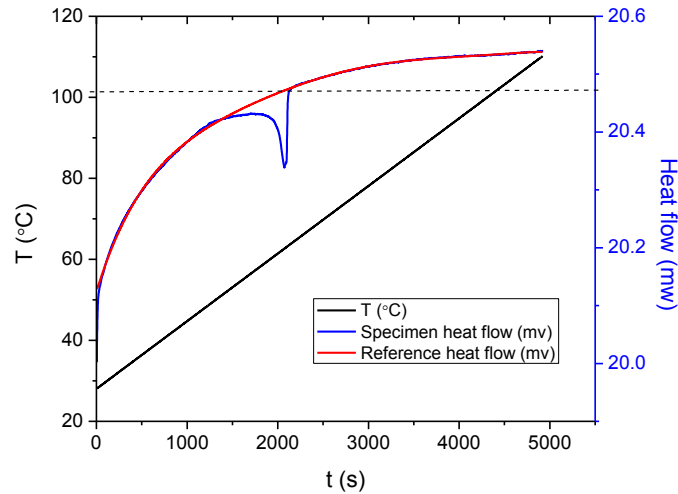
Figure 3.3 Results of a DSC test

The measurement resolution of the BW measurement system ($\approx 1 \text{ pm}$) limits the lower bound of a configuration. Considering the uncertainty within 0.5%, the required BW shift is 200 pm over the entire curing process. A supplementary numerical

analysis using the typical values of the effective chemical shrinkage and modulus of elastomers was conducted to confirm that the selected configuration would produce the BW shift larger than 200 pm, which was further verified by experimental results.
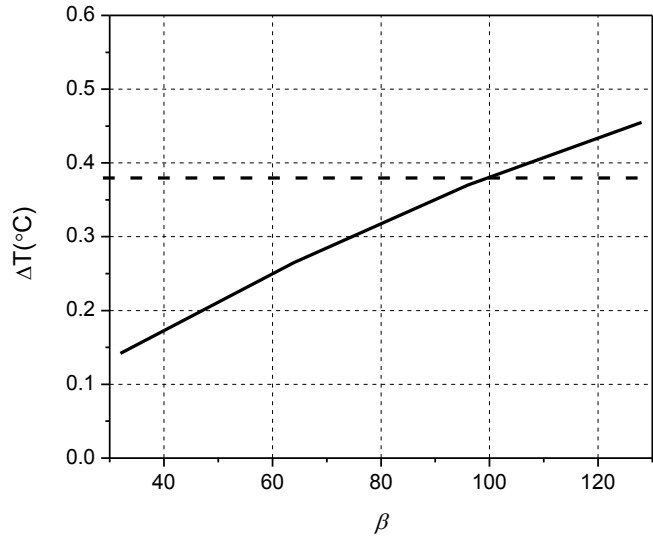
Figure 3.4 Temperature difference between the center and the edge of a
elastomer/fiber assembly after curing as a function of configuration

Another important criterion that should be considered for elastomers is "free-edge effect". The free edge effect is illustrated in Figure 3.5, where a deformed configuration as well as an axial strain along the fiber is shown schematically. The strain distribution over the fiber Bragg grating (FBG) is magnified and shown in the insert, where ε_c and ε_e represent the strains at the center and edge of the grating, respectively. The difference between the two strains is caused by the free edge effect, which becomes significant for a given configuration when the modulus of the specimen becomes small.

If the length of the configuration increases, the values of both ε_c and ε_e will reach the value of the generalized plane strain, ε_{ps}. Since the governing equations are

27

based on the generalized plane strain condition, the actual FBG reading would underestimate the elastomer strain unless the strain over the FBG is uniform; i.e., $\varepsilon_c \approx \varepsilon_e \approx \varepsilon_{ps}$.
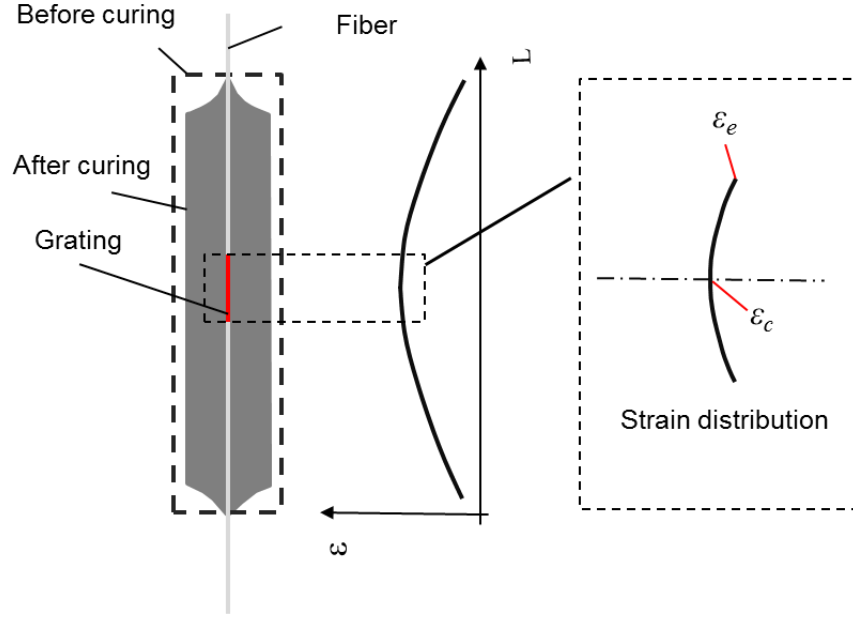
Figure 3.5 Schematic illustration of the strain distribution

The length of the fiber grating used in the current study is 5 mm. The ratio between the edge strain and the generalized plane strain, ζ, is used to quantify the free edge effect; the ratio is defined as:

$$\zeta = \frac{\varepsilon_e}{\varepsilon_{ps}} \tag{3.15}$$

The value ζ is directly affected by the length of the configuration and the outer radius of the configuration (i.e., the fiber radius, r_f, multiplied by the configuration, β).

An FEM simulation was conducted to quantify the effect. The first simulation result of the selected configuration ($\beta = 100$) using the standard fiber ($r_f = 125$ μm) is

28

shown in Figure 3.6, where the ratio, ζ, is plotted with respect to the configuration length. For the selected configuration, the length to achieve the ratio of "unity" is too long to be implemented in practice.

In order to cope with the problem, a special fiber with a smaller radius ($r_f = 80$ µm: Nufern) was used to produce the configuration. The ratio of the configuration with the special fiber is compared with that with the standard fiber in Figure 3.6. The results show that the specimen length of 100 mm completely negates the free edge effect if the specimen is fabricated using the special fiber.
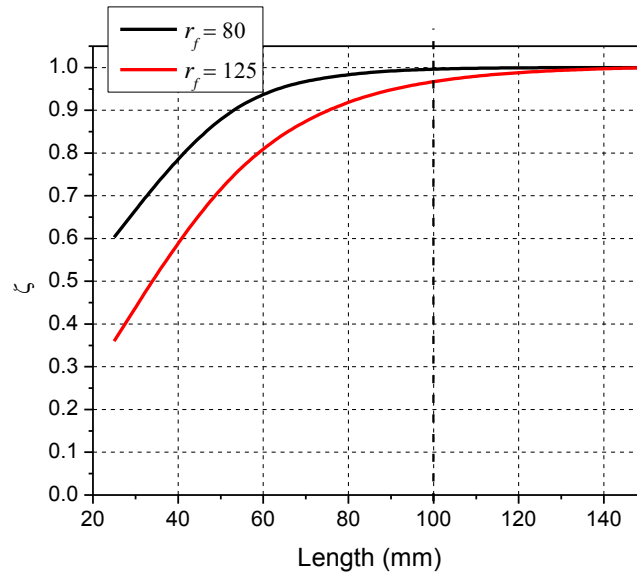
Figure 3.6 Ratio between the edge strain and the generalized plane strain

3.2.2. Experiment

The selected configuration ($\beta = 100$) is fabricated with the special fiber ($r_f = 80$ µm), which produces the specimen with $r_s = 8$ mm. Theoretically, this configuration is sufficient for measurements of the two properties. In order to verify the most critical assumption ("*the curing-induced strains are elastic*"), on which the modified

29

governing equation is based, an extra specimen is fabricated using the standard fiber ($r_f = 125$ μm). Using the same specimen, the configuration of the extra specimen offers $\beta = 64$ (or $= 8000/125$). The two specimens contain the nearly same amount of the elastomer material, and thus can provide similar curing conditions.

3.2.2.1. BW Shift during Curing

In the original implementation, a silicone rubber tube was used as a mold to contain the liquid state of polymers before curing [20]. In spite of its low modulus, the tube is not adequate for elastomers. An extremely flexible circular mold is required in order to provide "zero" constraint during curing.

The procedure to fabricate the flexible mold is illustrated in Figure 3.7. A metal rod was machined to have the diameter required for the desired configuration; the rod was wrapped with a plastic wrap; then the plastic wrap was taken off from the rod.

Metal rod
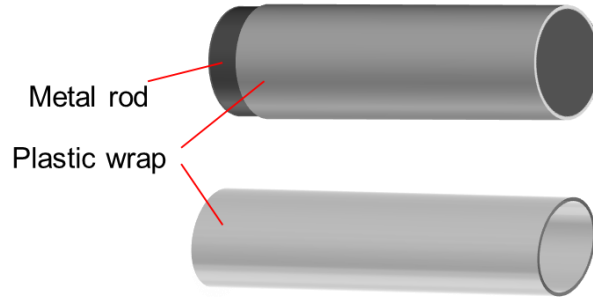
Plastic wrap

Figure 3.7 Fabrication procedure of constraint-free cylindrical molds using plastic wrap

Two plastic-wrap cylinders were mounted on an aluminum base plate and a small rubber plug with a tiny hole at the center was inserted to block the bottom side of the cylinder (see Figure 3.8). The fiber was inserted through the center hole of the

plug and positioned along the center of the plastic mold using an auxiliary alignment

fixture. The silicone elastomer was then injected into the mold from the top.
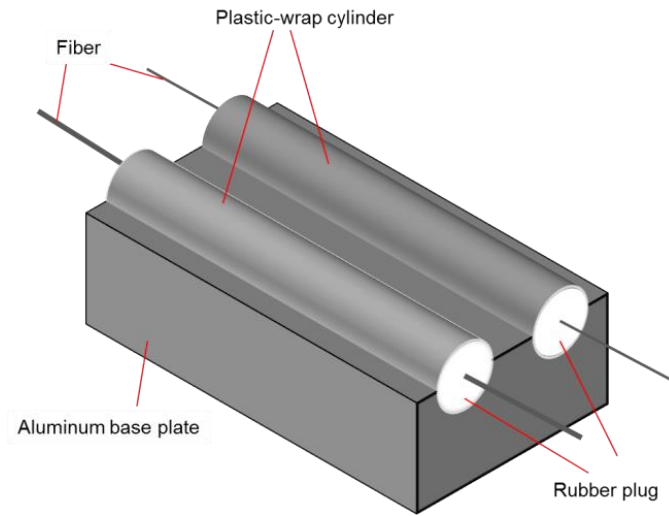
(a)
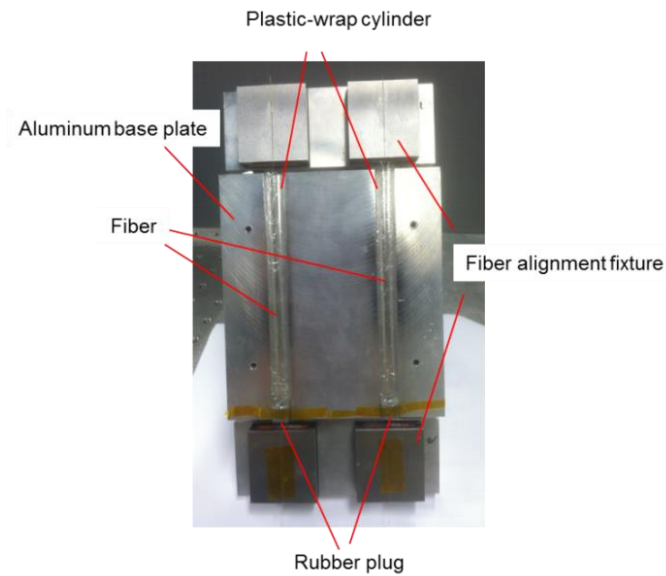
(b)

Figure 3.8 Curing test setup: (a) schematic illustration of the plastic-warp cylinder
mounted on the aluminum base plate and (b) the photo of the actual setup

The measurement setup is shown schematically in Figure 3.9. The mold/base plate assemblies were placed in an environmental chamber to maintain a constant temperature during curing, and the BW shifts were measured by the FBG-IS system. The BW shifts were recorded continuously over 60 hours until the BW signal did not change for half an hour. The chamber maintained the temperature within 0.2 °C during the recording.
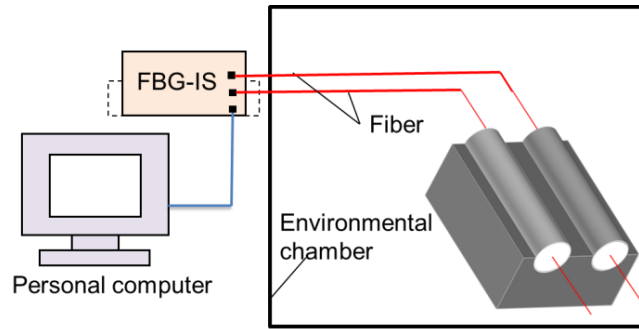
Figure 3.9 Schematic illustration of the experimental setup

The BW shifts of the two configurations are shown in Figure 3.10. The gelation time was around 6 hours. The total BW shift of the main specimen was 0.829 nm while the extra specimen produced the total BW shift of 0.373 nm. The specimens were taken out of the base plate after curing. The cured specimens are shown in Figure 3.11.

3.2.2.2. Equilibrium Modulus and Effective Chemical Shrinkage

The equilibrium modulus can be determined from the cured specimen. Considering two configurations, Eq.(3.11) yields:

$$\frac{\Delta\lambda_d^{\beta=100}}{\Delta\lambda_d^{\beta=64}} = \frac{F\left(E_\infty, \beta=100\right)}{F\left(E_\infty, \beta=64\right)} \tag{3.16}$$
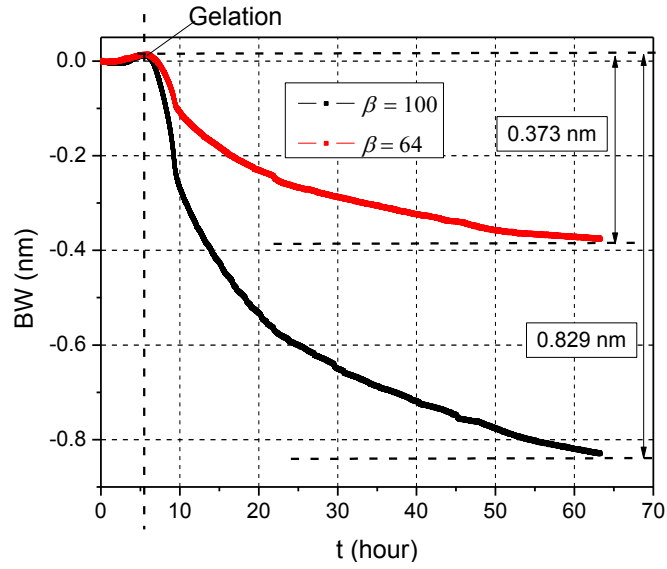
Figure 3.10 BW shift as a function of time obtained during curing
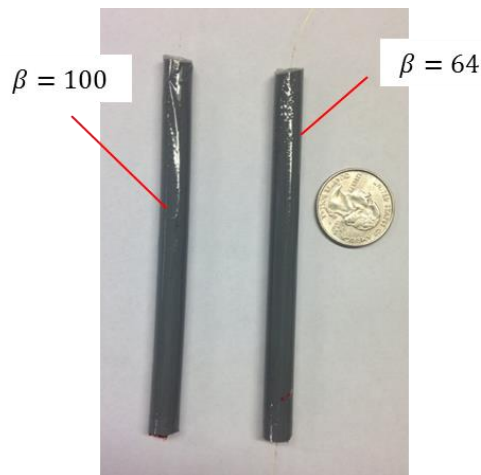
Figure 3.11 Cured specimens

The right hand side of the above equation is only a function of the equilibrium modulus, E_∞. Therefore, the equilibrium modulus can be directly calculated from the experimental data even when the applied loading (or strain) is not known.   The F

33

functions of the two different configurations are plotted as a function of modulus in Figure 3.12(a), while the ratio of the two configurations is plotted in Figure 3.12(b).
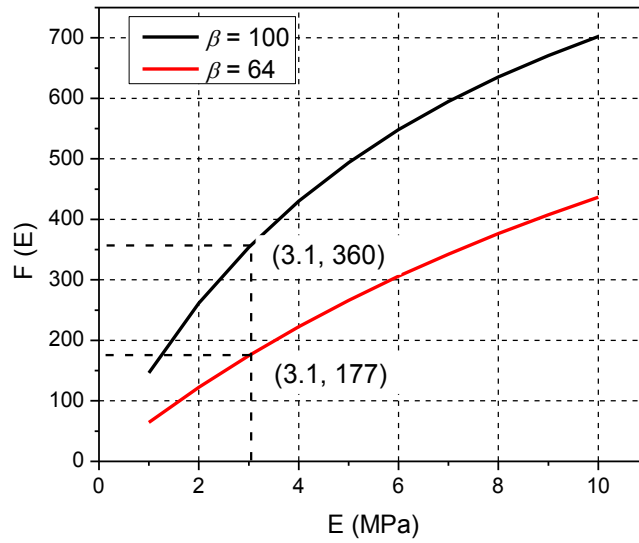
(a)
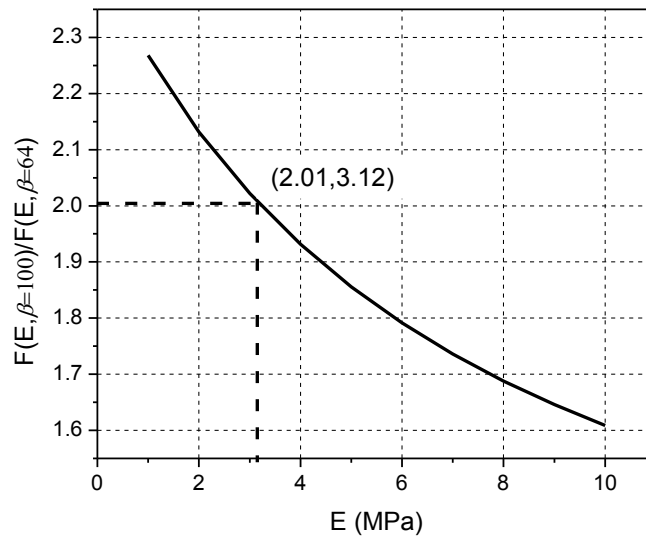
(b)

Figure 3.12 (a) The values of F function and (b) the ratio between two configurations; the dashed lines indicate the values used in the measurements.

The modulus of the elastomer is independent of temperature above its glass transition temperature (around -20 ℃). The thermal strain was used to determine the

equilibrium modulus. The two specimens were subjected to a temperature change from 30 ℃ to 20 ℃. The BW shifts were recorded until the values stabilized at each temperature. The results are shown in Figure 3.13. The BW shifts obtained from Figure 3.13 are 0.790 and 0.393 nm for $\beta = 100$ and 64, respectively, which yields the ratio of the BW shifts of 2.01. Using the ratio, the equilibrium modulus can be determined from Eq. (3.16). This procedure is illustrated in Figure 3.12(b): the equilibrium modulus is 3.12 MPa.
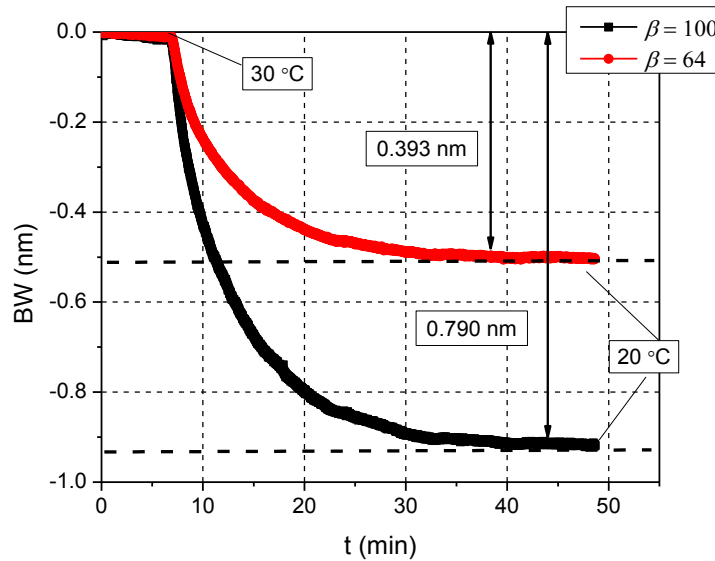
Figure 3.13 BW shifts as a function of time, documented during cooling the cured specimens

Using the equilibrium modulus $E_\infty = 3.12$ MPa, the value of F function for β = 100 is first determined from Figure 3.12 (a): $F(3.1)\big|_{\beta=100} = 360$. Then the total effective chemical shrinkage is determined from Eq. (3.11) using the total BW shift value of 0.829 nm: it is 0.23%.

35

3.2.2.3. Validity of Modified Governing Equations

For the governing equation, the curing-induced strains were assumed to be elastic. It was further assumed that the elastomer behavior above the glass transition temperature was also elastic. The following experimental results are presented to verify the validity of the assumptions.

The second assumption was first verified using a tension test at room temperature. The tension test setup is shown in Figure 3.14, where a long thin specimen is clamped at the top and bottom sides. The gap between the fixtures was $L = 12.86$ mm. The area of the cross section of the specimen was $A = 0.565$ mm^2.
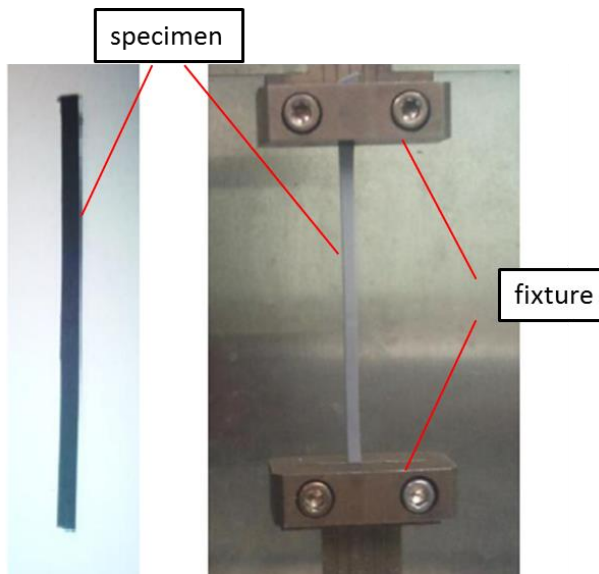
Figure 3.14 Tension test setup

The load vs. displacement curve is shown in Figure 3.15. The curve shows a linear elastic behavior when the strain is within 10%. The slope of the curve is $k = 14.21$ g/mm. The Young's modulus was calculated from the slope $\left(E = \dfrac{9.8kL}{A} \right)$ MPa and it was 3.17 MPa. The value is virtually the same as one measured by the FBGS technique, which confirms the validity of the second assumption.

The first assumption was verified by the extra specimen with the regular fiber ($\beta = 64$). Using the equilibrium modulus $E_\infty = 3.12$ MPa, the value of the F function for $\beta = 64$ was determined from Figure 3.12(a): $F(3.1)|_{\beta=64} = 177$. The effective chemical shrinkage was determined to be 0.21% using the total BW shift of 0.373 nm. The total effective chemical shrinkage differs from the value obtained from the original configuration by less than 10%, which confirms that the assumption is reasonable.

Under an ideal curing condition, the total chemical shrinkage obtained from the two configurations should be identical. The BW measurement uncertainty should be attributed to the small difference. Another possible reason for the difference might be that the initial part of curing may be volatile for the long and large specimen, which may cause the difference, albeit optimized by using two different fibers. The averaged value of 0.22% will be used for the following residual deformation analysis.
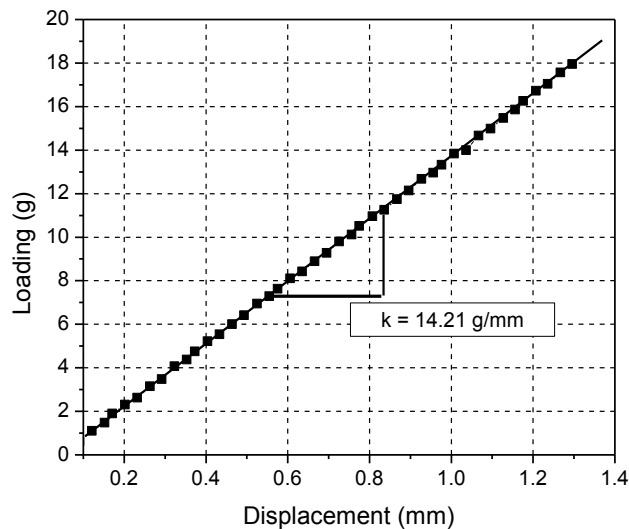
Figure 3.15 Load-displacement curve of the tension test

3.2.3. Application: Potted Driver Electronics

The total effective chemical shrinkage and the equilibrium modulus of the silicone elastomer were used to determine the residual stress of a potted LED driver electronics. The driver electronics is illustrated schematically in Figure 3.16. An electrolytic capacitor sealed with a butyl rubber plug is embedded in a PVC cylindrical holder, which is filled with the silicone elastomer as a potting compound.
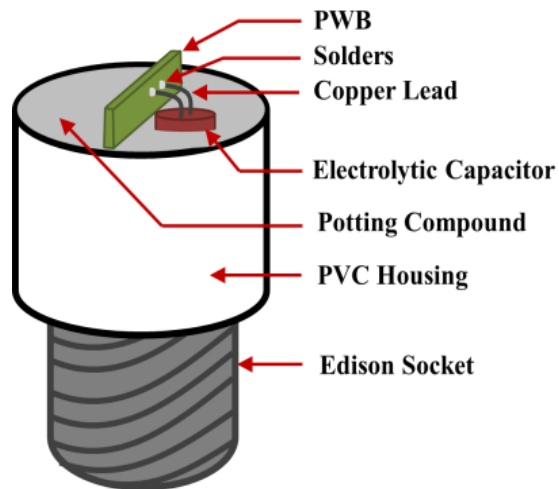
Figure 3.16 Schematic of the LED driver electronics

During curing of the potting compound, the rubber plug is stretched due to the volume shrinkage of the compound. The radial stress tends to separate the plug from the aluminum case of the capacitor, causing the leakage of the electrolyte. The leakage of the electrolyte has been known as one of the main failure modes of the electrolytic capacitor [101, 102]. A numerical analysis was conducted to determine the residual stresses of the rubber plug developed during encapsulation.

The axisymmetric model of the potted system is shown in Figure 3.17. The capacitor, containing the electrolyte, is modelled as an empty aluminum cylinder with

the top end sealed with the plug. The 2-D axisymmetric model is meshed with quadratic linear elements in ABAQUS. The radial displacement of the center is fixed as a boundary condition. The material properties of each component used in the model are listed in Table. 1.

As mentioned earlier, the volumetric shrinkage before the gelation does not contribute to the residual stress. Therefore, the phase change from liquid to solid process is not modelled. The volumetric change caused by the effective chemical shrinkage was simulated using a thermal strain analogy; the elastomer contracts by the total effective chemical shrinkage while other materials do not contract. This was accomplished by applying the pseudo-temperature change to the silicone elastomer as the thermo-mechanical loading.
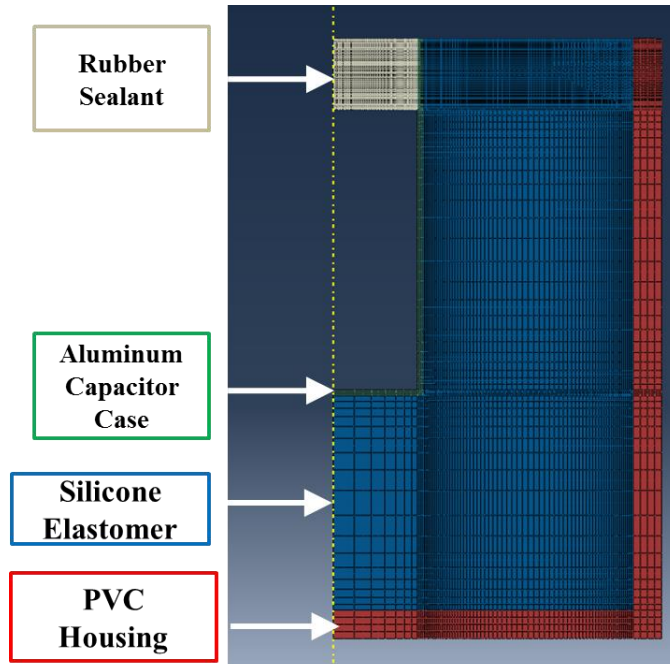
Figure 3.17 Axisymmetric model of the potted electrolytic capacitor

Table 1 Material properties used in the FEA

Layer Type	Elastic Modulus (MPa)	Poisson's Ratio	CTE (ppm/°C)
Aluminum	69,000	0.33	0
Rubber Sealant	2,500	0.49	0
PVC	10,000	0.38	0
Silicone elastomer	3.12	0.49	200

The residual stress and strain after encapsulation curing were calculated from

FEM. The radial components at the rubber sealant are shown in Figure 3.18. The

maximum stress occurred at the top which was directly connected to the aluminum case

(Figure 3.18(a)), and its value was 0.395MPa. The strain in the sealant was also

positive and its maximum value was 0.005%.

The analysis indicates that the small magnitudes of the residual stress and strain

in the rubber sealant produced by the curing shrinkage of the potting compound does

not seem to be cause the leakage of the electrolyte. Other factors like the thermal and

hygroscopic processes are to be further investigated for the electrolytic capacitor failure.

(a)   (b)
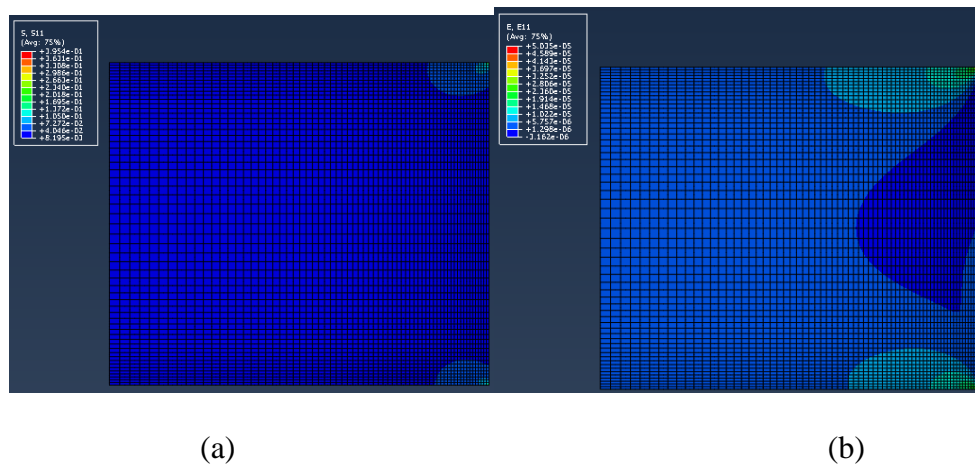
Figure 3.18 Radial component of (a) the residual stress (b) the strain at the rubber
           sealant

3.2.4. Summary

The total effective chemical shrinkage and the modulus of a silicone elastomer were measured by the FBGS technique. The technical challenges encountered due to the extremely low modulus of the elastomer were handled effectively by (1) developing a constraint-free mold and (2) employing a special fiber with a smaller diameter. In the method, the curing-induced strains were assumed to be elastic; and the elastomer behavior above the glass transition temperature was also assumed to be elastic. These critical assumptions were verified by an extra specimen with the standard fiber and a conventional tension test. The measured properties were then used to characterize the residual stress in an electrolytic capacitor developed during encapsulation process. The results revealed that the residual stress caused by curing the potting compound was not significant to cause the electrolytic capacitor failure.

3.3. Underfill curing

The underfill curing using the FBG method has been implemented before [20, 29]. The modulus evolution and chemical shrinkage are measured by the double configurations FBG method [20]. The predicted properties are used as inputs for the warpage prediction of the bi-material strip. Even though this method has been successfully applied to certain underfill materials, some technical challenges are identified in the following part. The new test procedure is proposed to address these challenges.

3.3.1. Challenges with the previous application

3.3.1.1. Friction between the polymer and the silicone tube

The underfill is liquid before curing. In order to maintain the cylindrical shape of the specimen during curing, a silicone tube was used as the mold. The friction between the tube and the material could affect the BW shift as shown in Figure 3.19.

In order to check the repeatability of the test, two tests with the same curing condition were conducted and the BW shifts are shown in Figure 3.20. The data has around 20% difference even though they shared the same curing condition. The poor repeatability could affect the calculated properties. In order to have repeatable data, the friction between the tube and the material should be avoided during curing of the specimen.
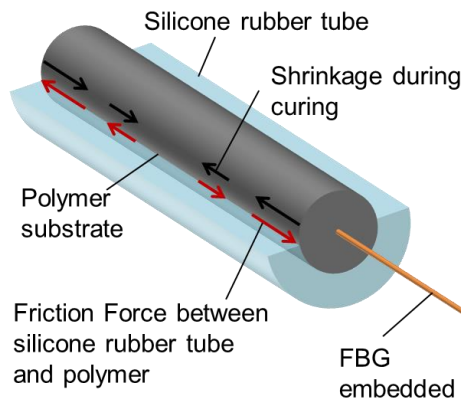
Figure 3.19 Friction between the tube and the material
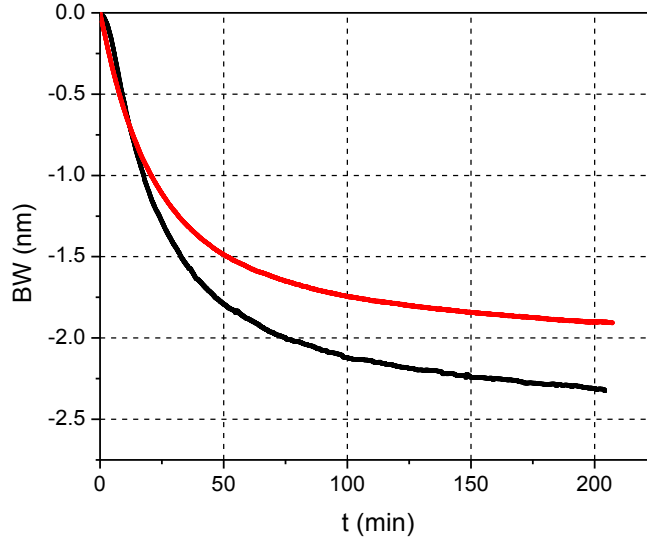
Figure 3.20 BW repeatability of the curing test

3.3.1.2. Calculation procedure

In the derivation of the calculation procedure in the paper [20], a critical assumption was made: the modulus change over a small temperature increment was assumed to be ignorable. Take the derivative of equation(3.11),

$$\Delta\lambda_d = F'(E)\tilde{\varepsilon}\Delta E + F(E)\Delta\tilde{\varepsilon} \approx \frac{F(E+dE)-F(E)}{\Delta E}\tilde{\varepsilon}\Delta E$$

$$+F(E)\Delta\tilde{\varepsilon} = F(E)\Delta\tilde{\varepsilon} + \big(F(E+\Delta E)-F(E)\big)\tilde{\varepsilon} \qquad (3.17)$$

In the derivation, the part $\big(F(E+\Delta E)-F(E)\big)\tilde{\varepsilon}$ was assumed to be "zero", which is not valid during curing of the polymer. Figure 3.21shows the comparison of the calculated BW from the approximation solution and the exact solution. The plot shows that the approximation calculation procedure underestimated the BW around 30%. The accurate analytical equation (3.11) should be used for the property calculation.

43
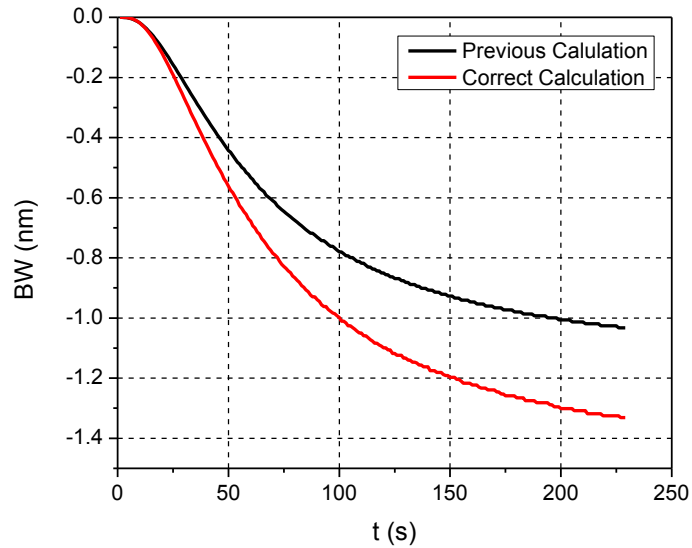
Figure 3.21 Comparison of the calculated BW

3.3.2. Proposed procedure for the underfill curing

A two-stage curing procedure is proposed for the underfill curing. By taking advantage of the liquid phase of underfill before curing, a silicone tube was used to hold the underfill before curing. The FBG sensor is embedded in the liquid underfill before curing. When the underfill reaches near the gelation point, it will become rubbery and the silicone tube can be taken off shown in Figure 3.22. As long as the tube is taken off before the gelation, the curing properties will not be affected.
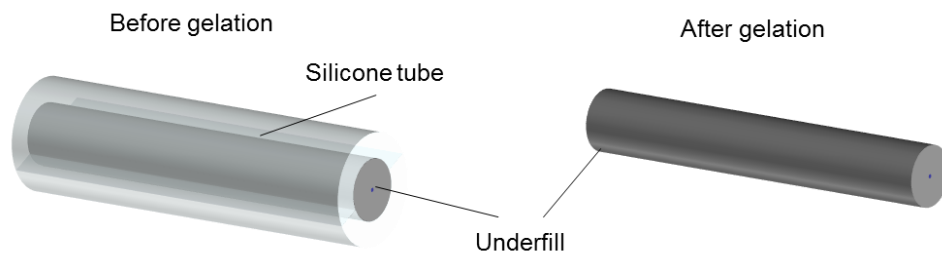
Figure 3.22 Two steps curing procedure

The gelation point of the underfill curing is related to the curing temperature. The glass transition of the cured the underfill material is around 130°C. To ensure the elastic strain assumption, the curing temperature should be above glass transition. The curing time at different curing temperature is tested and shown in Figure 3.23. At 170°C, it takes around 8 min to reach solid status. After reaching the solid status, the fiber will start to pick up BW, which is the gelation point. At 150°C, the gelation point moved to around 30 min. In order to have enough time for operation, the curing temperature will be set as 150°C.

The configuration selection is based on Figure 3.24. The y-axis is the normalized strain, which is fiber strain/applied strain. The modulus of the cured underfill is around 0.2~0.5 GPa. In order to have optimum configuration, the outer diameter 3.1 mm is selected. It will produce: 39X (80 μm), 25X (125 μm) and 18X (175 μm).
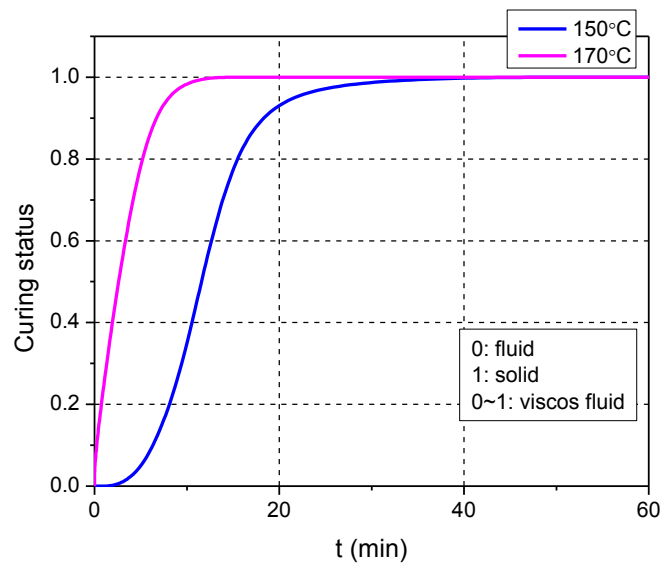
Figure 3.23 Curing status of underfill at different temperatures
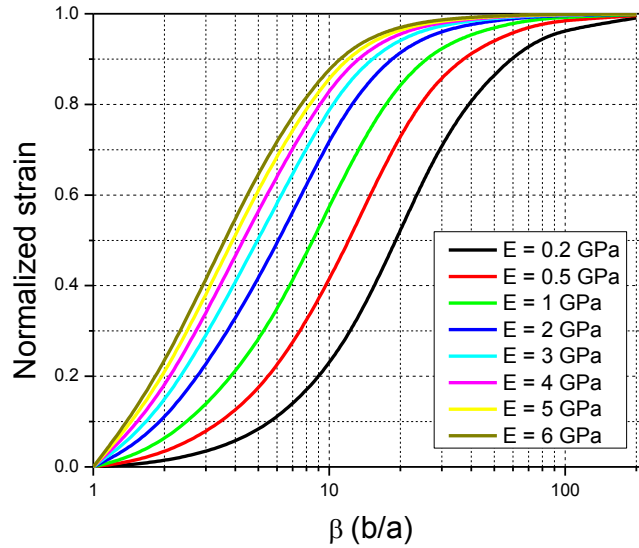
Figure 3.24 Normalized strain with different configurations and modulus

The temperature overshooting is measured by the two thermocouples at 150°C. One thermocouple is embedded in the center; the other thermocouple is embedded at the end of the specimen. The temperature overshooting is shown in Figure 3.25. The maximum temperature different is 3 °C at around 10 min. At 20 min, the temperature different is within 0.5 °C. It will not affect the curing of the material.
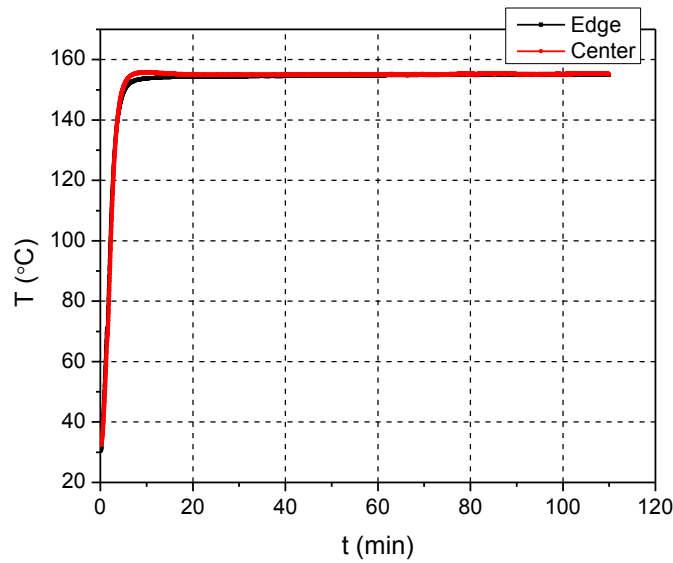
Figure 3.25 Temperature overshooting of the underfill curing

The finalized curing steps for underfill are:

1) Cure the specimen at 150°C with silicone tube for 20 min; specimen will be low modulus rubbery.

2) Cool the specimen to room and take off the tube; specimen is solid.

3) Heat the specimen to 150°C and continue curing; specimen is rubbery again.

3.3.3. Results

The BW change during the two stage curing is shown in Figure 3.28. The first stage takes about 20 mins. After that the specimen cools down to room temperature and the BW also decrease. The silicone tube is taken off at room temperature. The BW change in the first stage is illustrated in Figure 3.27. Before the gelation point, BW keeps constant, indicating that modulus is still 0. The BW starts to pick up at the second stage at around 60 mins. The BW change of the two configurations in stage two is presented in Figure 3.28, and total BW shift is 1.69 nm for the 125 μm fiber and 2.65 nm for the 80 μm fiber.
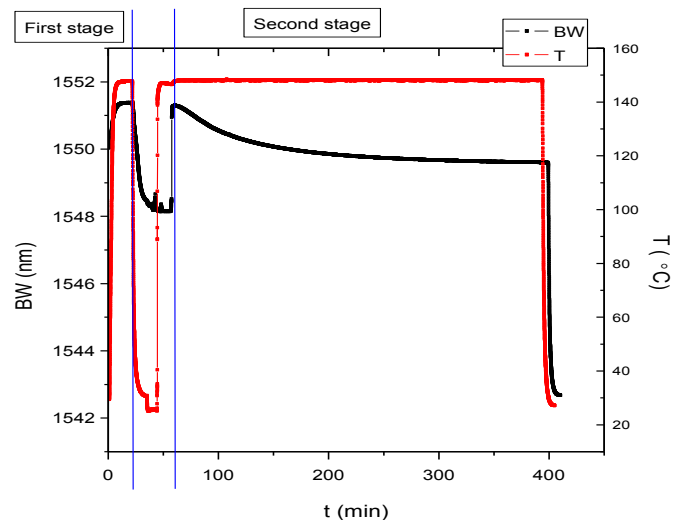
Figure 3.26 BW change during the two stages curing

47
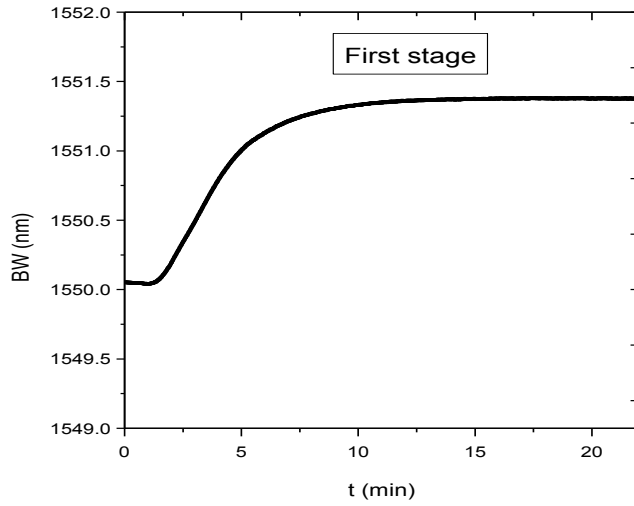
Figure 3.27 BW shift in the first stage
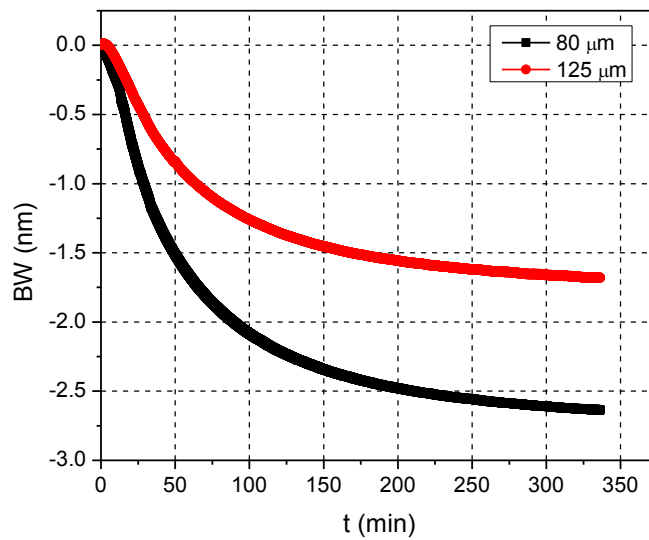
Figure 3.28 BW shift of the underfill curing in for the two configurations

The elastic modulus at 150°C is measured by a supplementary experiment. The two cured specimens are subjected to the temperature change from 145°C to 155°C. The BW change of the two specimens is shown in Figure 3.29. The stress induced BW

change is from the total BW change minus temperature induced BW change and is

0.924 nm for 80 μm fiber and 0.735 nm for the 125 μm fiber. The averaged elastic

Young's modulus can be calculated to be 224 MPa from the equation:

$$\frac{\Delta\lambda_{d1}(t)}{\Delta\lambda_{d2}(t)} = \frac{F(E(t),\beta_1)}{F(E(t),\beta_2)}.$$
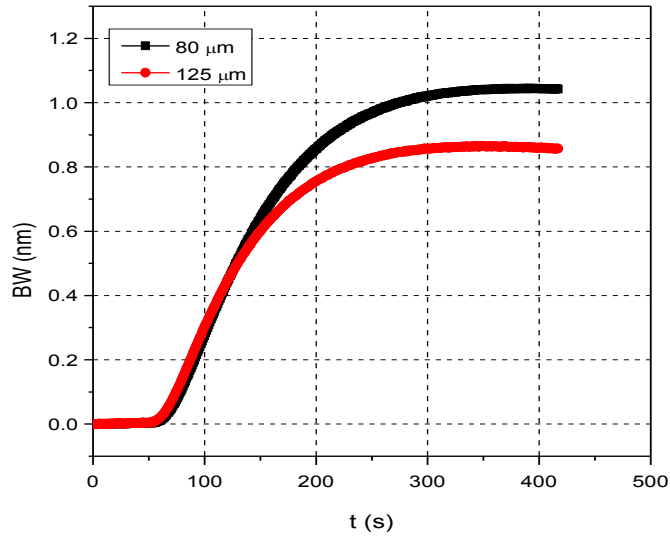
Figure 3.29 BW change of the two specimens subjected to temperature change

The three point bending test is conducted to measure the elastic at 150°C to

verify the measured Young's modulus by the thermal loading. The dimension of the

specimen is: span l =25 mm, width w = 8.4 mm and thickness t = 2 mm. The load-

displacement curve is shown in Figure 3.30. The linear curve indicates the elastic

behavior of the underfill at 150°C. The Young's modulus can be calculated by the

equation:

$$E = \frac{l^3 F}{4wt^3 d} = 206 \, \text{MPa}$$

The effective chemical shrinkage from the two configurations can be calculated: 0.225% for the 125 μm fiber specimen and 0.263% for the 80 μm fiber specimen. The 80 μm fiber specimen has higher shrinkage than the 125 μm fiber specimen, the same trend as the silicone elastomer.
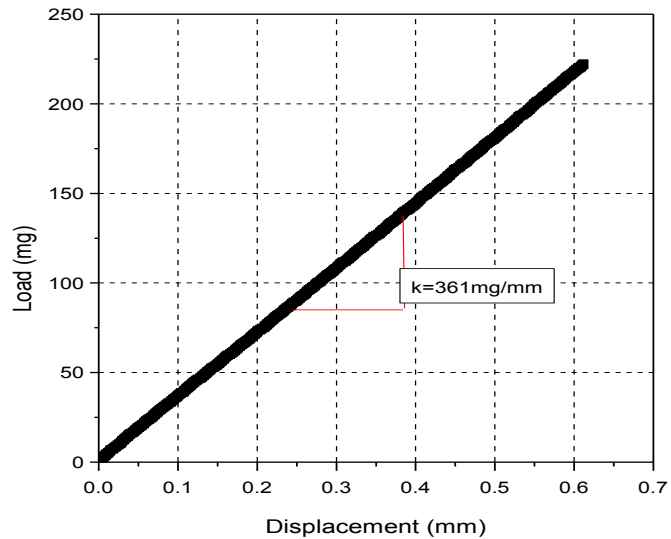
Figure 3.30 Load-displacement of the three point bending test

3.4. EMC curing

The EMC curing requires high pressure around 7 MPa [103] and high temperature about 175°C. It is also challenging to embed the fiber right in the center of the polymer during curing. A novel experiment setup and procedure is developed for the curing of EMC.

3.4.1. Configuration selection

The configuration selection is related to select proper fiber diameter, configuration and length of the specimen. Due to the high modulus of the EMC, the infinite configuration will be used for the test, which means the measured strain is the same as the curing strain. The cured modulus of the EMC is around 2 GPa. From Figure 3.24, the configurations can be considered as infinite configurations when it is bigger than 50X. The configuration 70X (125 μm fiber) was used for the curing test. The length of specimen was selected to be 15 mm considering the practical limitation. The heat generation and the generalized plane strain condition were examined using the same procedure as the silicone elastomer. This configuration can satisfy the temperature overshooting and plane strain requirements.

3.4.2. Experimentation

The stainless-steel mold assembly to fabricate the specimen is shown in Figure 3.31(a). The assembly consists of a bottom mold, a symmetric top mold (not shown in the figure) and two side molds. The uncured EMC specimen pellet sits in the cylindrical chamber of the mold. A small through hole was drilled in the center of the EMC pellet. The optical fiber (diameter of 125 μm) was carefully inserted through the hole shown in Figure 3.31(a). The fiber position was adjusted until the Bragg grating (5 mm long) was placed in the middle of pellet; this was achieved by making a mark on a fiber considering the length of the mold.   A machined plunger and an air cylinder (BIMBA: SR121) was mounted on the mold to apply pressure to the pellet during curing shown in Figure 3.31(b).   The plunger has the same diameter as the chamber and it can apply compressive loading to the specimen. It should be noted that a small

51

notch was machined on the plunger and there is small through hole on the bottom of

the plunger. The notch and the hole were made for the fiber to penetrate the plunger,

so that the fiber can be stretched during curing to ensure straight.
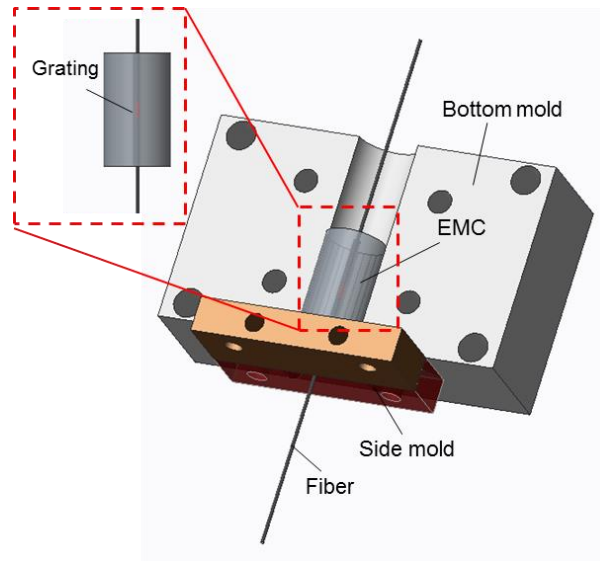
(a)
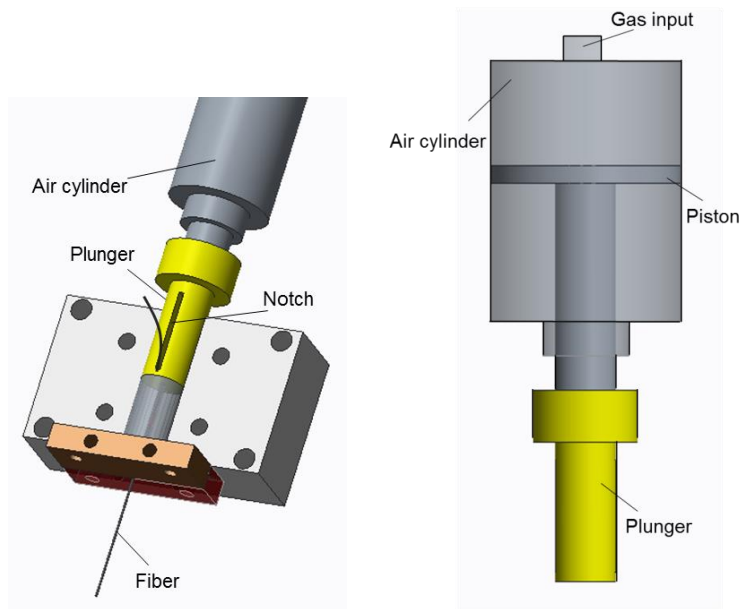
(b)

Figure 3.31 The assembly to fabricate the specimen

The complete system is shown in Figure 3.32(a). The mold (with the pellet) was mounted on a high precision hot/cold plate (HCP304: Instec), which provided a temperature resolution of ± 0.05 °C. The pressure required for curing was provided by the mechanical plunger, which was attached to the air cylinder. The air cylinder converted the gas pressure supplied from the pressure regulator (ER3000: Tescom) to a mechanical pressure. The external pressure source was connected to the pressure regulator, which was controlled by the personal computer.

The grating sensor was placed in the center of the EMC pellet. The surface of the mold was treated with a release agent and the pellet was wrapped with a very thin Teflon tape before the curing process started shown in Figure 3.32(b). This pre-processing ensured (1) unconstrained curing of the EMC (i.e., virtually zero-friction between the mold wall and the EMC) and (2) easy separation after curing. A rubber gasket was also placed between the plunger head and specimen to eliminate the leakage during curing, especially after the high pressure was applied. The fiber was connected to the interrogator (sm125: Micro Optics) and the interrogator was connected to the personal computer to collect data from the FBG sensor.
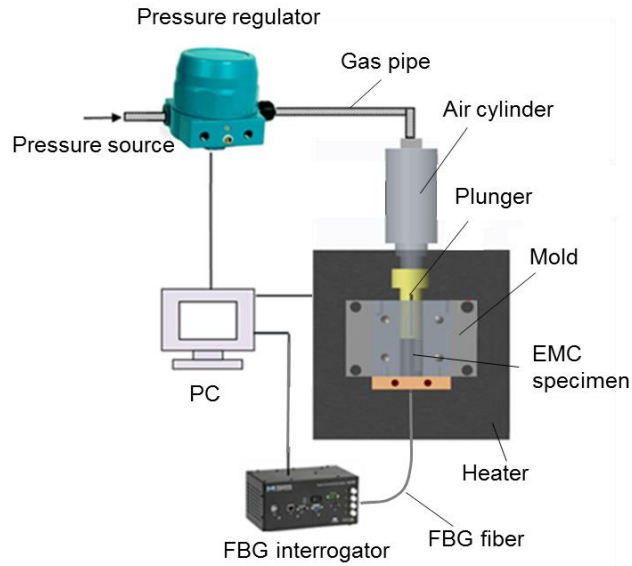
(a)
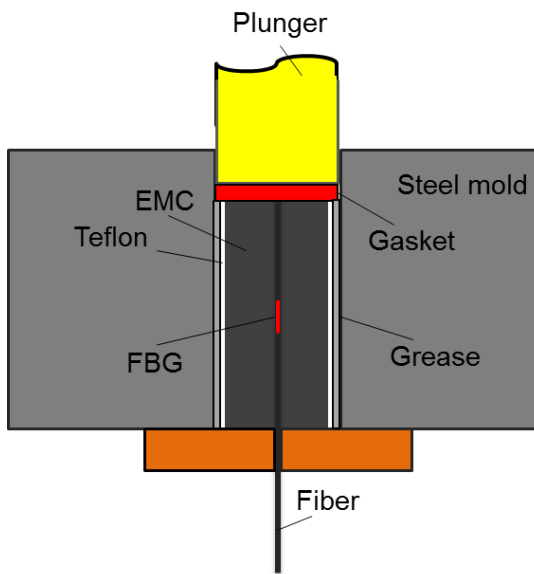
(b)

Figure 3.32 Specimen fabrication Setup

After the specimen temperature reached the curing temperature (175°C), the pressure of 7 MPa was applied and maintained during curing. The required EMC curing pressure was P_{curing} = 7 MPa, but the maximum pressure of the compressed air

line was only $P_{source} = 0.69$ MPa (100 psi).   The required mechanical pressure was achieved by the air cylinder whose piston diameter was much larger than the diameter of the plunger (see Figure 3.31(b)).

The diameter of the piston that can produce the required pressure at P_{source} can be determined as

$$D_{piston} = \sqrt{\frac{P_{curing}}{P_{source}}} \times D_{plunger} = \sqrt{\frac{7 \text{ MPa}}{0.69 \text{ MPa}}} \times 8.8 \text{ mm} = 28.0 \text{ mm} \qquad (3.18)$$

The air cylinder with $D_{piston} = 31.75$ mm (1.25 inch) was selected for the system.   The air pressure to produce P_{curing} was then determined as:

$$P_{source} = \left(\frac{D_{plunger}}{D_{piston}}\right)^2 \times P_{curing} = \left(\frac{8.8 \text{ mm}}{31.75 \text{ mm}}\right)^2 \times 7 \text{ MPa} = 0.54 \text{ MPa (78 psi)} \quad (3.19)$$

The specimen was released from the mold after curing it for 5 minutes and was subsequently subjected to a post mold curing process (for 2 hours at the same temperature) to ensure complete curing. The cured specimen is shown in Figure 3.33. The diameter and the length of the cured EMC was 8.8 mm and 15 mm.

The location of the Bragg grating is very important to obtain a proper signal from the specimen. The cross section of the cured specimen was examined to confirm the fiber location. The cross section images of the specimen cut along the lines shown in Figure 3.33. The results confirmed that the procedure was effective and thus the fiber position was maintained at the center of the specimen after curing.
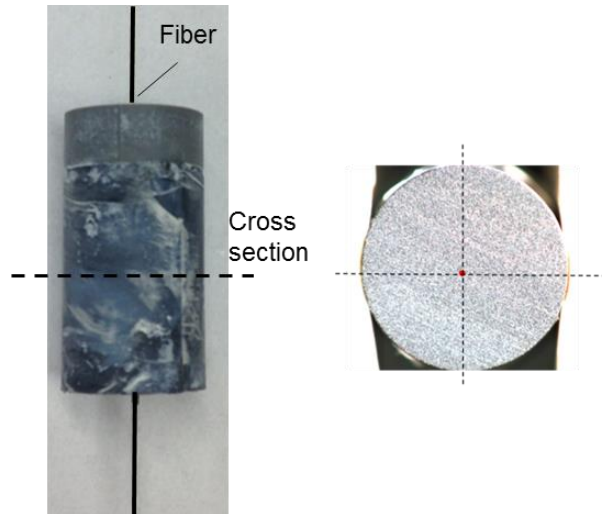
Figure 3.33 Cured EMC specimen and cross section

3.4.3. BW shift of the EMC curing

The BW shift during EMC curing is shown in Figure 3.34. The gelation point is around 20 min. The total BW shift is 2.572 nm. The BW jump after releasing pressure is illustrated in Figure 3.34(b). The pressure induced BW change is 0.2 nm and the curing inducted BW shift is 2.372 nm. The total effective chemical shrinkage is calculated to be 0.20%.
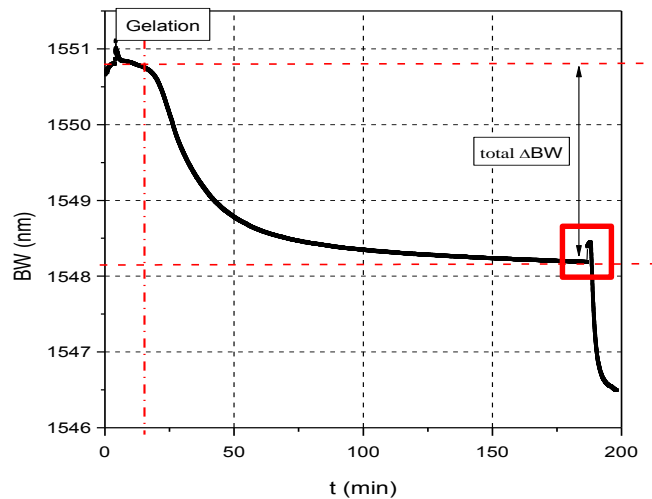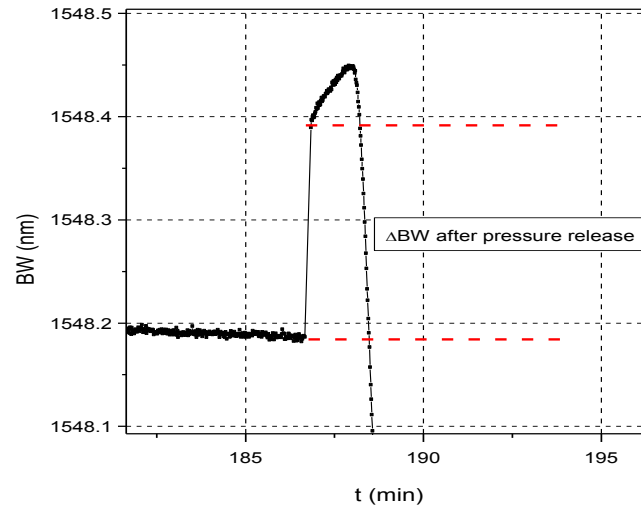
(b)

Figure 3.34 BW shift during curing of EMC

In order to verify that the curing induced strain is independent of the temperature, the curing experiment was repeated at 140°C. BW shift after gelation point is presented in during in Figure 3.35 and compared with the data from 110°C. The curing induced BW change is 2.26 nm, which is close to the value cure at 110°C and the calculated strain is 0.19%. The results confirm that the effective chemical shrinkage is the same at different curing temperatures.
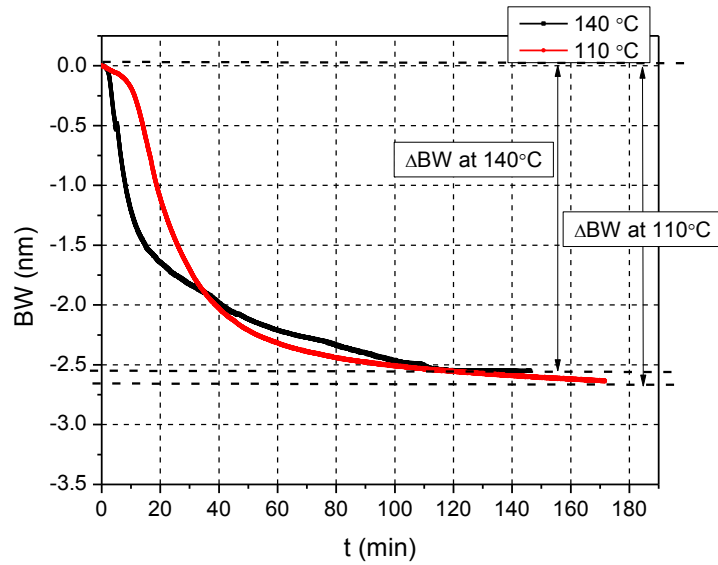
Figure 3.35 BW shift during curing of EMC at 140°C and 110°C

3.4.4. Summary

The effective chemical shrinkage of the EMC was measured by a specially designed setup under the high pressure and high temperature condition. The setup enables applying high temperature and high pressure to the specimen during curing of the EMC. The effective chemical shrinkage of the EMC is measured at 110C to be 0.20% and the curing test is repeated at 140°C. The measured curing shrinkages are close at the two different curing temperatures. The effective chemical shrinkage can be used to estimate the curing induced warpage of package.

3.5. Summary of the Chapter

This chapter presents the proposed curing properties measurement techniques for three different polymeric materials: silicone elastomer, underfill and epoxy molding compound. The silicone elastomer has low modulus after curing and requires relatively low curing temperature. A large configuration was proposed for the silicone specimen. A novel setup utilizing a thin plastic wrap was used to hold the uncured specimen. The underfill material has medium modulus but large heat generation during curing. A two-step curing procedure was proposed with a silicone tube to hold the uncured specimen at the first step. The tube was taken off in the second step to ensure free curing of the specimen. The EMC material requires high temperature and high pressure for curing. A novel setup was developed to accommodate the high temperature and pressure curing condition. The surface of the specimen was also treated to ensure free curing of the specimen. The effective chemical shrinkage of the EMC was determined at two different temperatures.

Chapter 4 Thermal Process Induced Warpage and Residual Stress

After the polymer cures in the package, the package has to go through various temperature change processes, such as the solder reflow, and cooling down to room temperature. These processes will also induce large warpage and residual stress in the package due to the CTE mismatch between different components in the package. In order to predict the warpage and residual stress during these processes, the viscoelastic properties of the polymer need to be determined accurately. Since the temperature change covers the glass transition range of the polymer, the temperature dependent CTE should also be measured.

The constitutive law of the comprehensive viscoelasticity is [62]:

$$s_{ij}(t) = 2\int G(t-\tau)\frac{\partial e_{ij}(\tau)}{\partial \tau}d\tau$$
$$\sigma_{kk}(t) = 3\int K(t-\tau)\frac{\partial \varepsilon_{kk}(\tau)}{\partial \tau}d\tau$$
(4.1)

where $G(t)$ and $K(t)$ are time and temperature-dependent shear and bulk modulus; s_{ij} and e_{ij} are the deviatoric stress and strain tensor; and σ_{kk} and ε_{kk} are dilatational stress and strain tensor.

The four elastic constants have the following relationships [63]:

$$K(T,t) = \frac{E(T,t)G(T,t)}{9G(T,t)-3E(T,t)}, \quad G(T,t) = \frac{E(T,t)}{2(1+v(T,t))}$$
(4.2)

where $E(T,t)$ and $v(T,t)$ are time and temperature-dependent Young's modulus and Poisson's ratio. In order to conduct the comprehensive viscoelastic modelling, at least two of the four constants have to be measured experimentally.

The cured specimen with a FBG sensor embedded in the center is used to measure the viscoelastic properties of EMC materials. A new governing equation for a general loading is presented first. The method to determine the comprehensive viscoelastic properties is described in detail and the results obtained from advanced EMC materials are presented. The results from supplementary experiments are followed to verify the validity of the assumptions associated with the viscoelastic modeling.

4.1. Governing equation for general loading

The mathematical formulations presented in [20, 29] were derived for the curing condition only; i.e., a volumetric strain loading. This section presents a governing equation for a general loading condition that is required for hydrostatic as well as uniaxial compression.

The loading condition is shown in Figure 4.1. An optical fiber is embedded in the center of a cylindrical shaped polymer specimen. The assembly is subjected to an axial pressure, P_1, and a radial pressure, P_2.
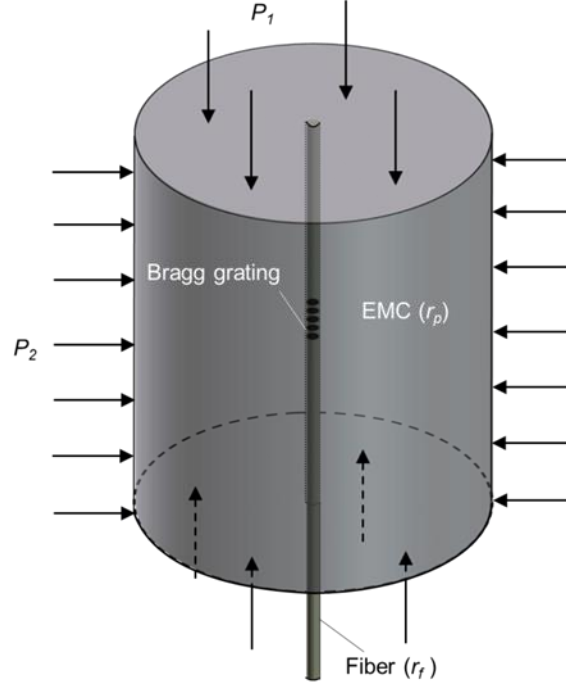
Figure 4.1 Loading condition

The stress distribution in the fiber and polymer are derived and shown in the appendix. The closed-from solution was verified by an axis-symmetric finite element model. The radial stress normalized by the applied pressure are compared in Figure 4.2, where the radius of the fiber, r_f, was 62.5 μm and the applied pressure was $P_1 = 2P_2 = 2P$. The results confirm that the analytical solution is accurate[84, 104].

The BW shift and the stress relation can be expressed as [20]:

$$\Delta\lambda = \frac{1}{E_f}\left\{\left[1 - \frac{n^2}{2}\left(P_{12} - (P_{12} + P_{11})v_f\right)\right]\sigma_{zz}^f - \left[2v_f + \frac{n^2}{2}\left((1 - v_f)P_{11} + (1 - 3v_f)P_{12}\right)\right]\sigma_{rr}^f\right\}\lambda_i$$

(4.3)

where $\Delta\lambda$ is the BW shift, λ_i is the initial BW, n is the effective refractive index, and P_{ij} are strain optic constants [85, 105].
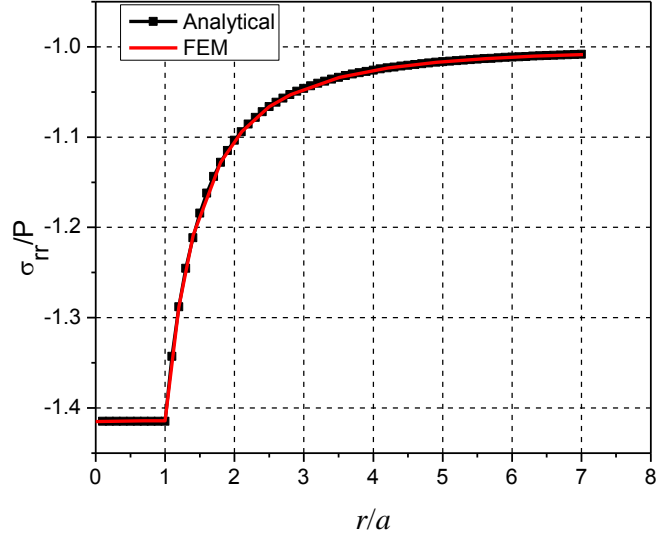
Figure 4.2 Comparison of the analytical solution and the FEM model

By substituting Eqs.(4.2) and (A.4) into (4.3), the BW shift can take the following form:

$$\Delta\lambda = \Pi\left(E_p, \nu_p, \beta\right) \tag{4.4}$$

where $\beta = \dfrac{r_p}{r_f}$ (will be referred to as "configuration"); E_p and ν_p are the Young's modulus and bulk modulus of the polymer; Π is a nonlinear function that can be expressed explicitly.

For a given configuration, β, the BW shift is a function of any two of four elastic constants of the polymer (Equations (4.4)). The two constants can be inversely determined from the BW shifts measured from two independent experiments. Although theoretically possible, determining two unknown parameters from an extremely non-linear equation can be very tricky. A special case arises for uniaxial loading, where the effect of polymer's Poisson's ratio becomes insignificant. The

following analysis provides the equations that are used to determine two required constants sequentially from two sets of experimental data.

The loading condition for uniaxial compression is $P_1 \neq 0; P_2 = 0$. The effect of Poisson's ratio under this loading condition is shown in Figure 4.3. The plots show the BW shifts caused by uniaxial compression as a function of configuration. The applied stress is adjusted to produce a similar vale of the BW shift; in each plot, the modulus is fixed but Poisson's ratios vary from 0.2 to 0.45. The Young's moduli in the three plots are 0.1 GPa, 0.5 GPa and 2.5 GPa. It is clear that the effect of Poisson's ratio on the BW shift is negligible. Thus, by assuming a typical value for Poisson's ratio (e.g., 0.3), the Young's modulus can be determined from:

$$E_p = \Pi^{-1}\left(\Delta\lambda, \beta\right) \tag{4.5}$$

The Matlab code of the inverse function to calculate Young's modulus is added in Appendix.
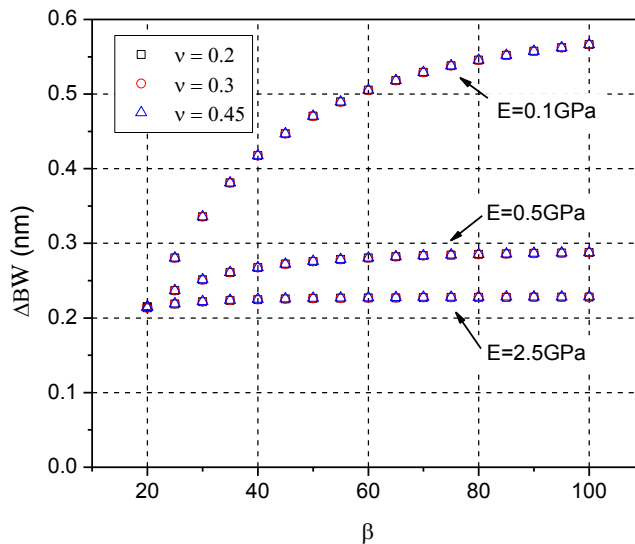
Figure 4.3 BW independent of the Poisson's ratio

The loading condition of hydrostatic testing is $P_1 = P_2 \neq 0$. As mentioned earlier, the BW shift for a given configuration can be expressed in terms of any two elastic constants. With Young's modulus given from the previous step, the bulk modulus can be determined from:

$$K_p = \Pi^{-1}\left(\Delta\lambda, \beta\right) \tag{4.6}$$

where K_p is the bulk modulus of the polymer. The functional form is the same. The Matlab code input to calculate the Bulk modulus is also added in Appendix.

4.2. Experimentation

4.2.1. Time-temperature dependent Young's modulus measurement

The curing setup shown in

Figure 3.31(b) was slightly modified to measure temperature-dependent Young's modulus. The schematic diagram of the setup is shown in Figure 4.4. The difference is that the diameter of the cylindrical chamber is slightly larger than the diameter of the specimen so that there is a gap between the specimen and the mold. The setup was mounted on the same heating system shown in Figure 3.32(a).

For the compressive creep test, the loading application should be as fast as possible to catch the initial part of the creep. The frequency of the data acquisition of the BW is 1Hz. The air cylinder is used to apply pressure to the plunger within 1 second. And then the plunger converts the air pressure to the mechanical loading to the specimen. A pre-determined pressure was applied instantaneously and maintained to

determine the BW change as a function of temperature. Considering the resolution (1pm) of the FBG interrogator, the rule to determine the applied pressure is that initial BW change should be at least 100 pm.
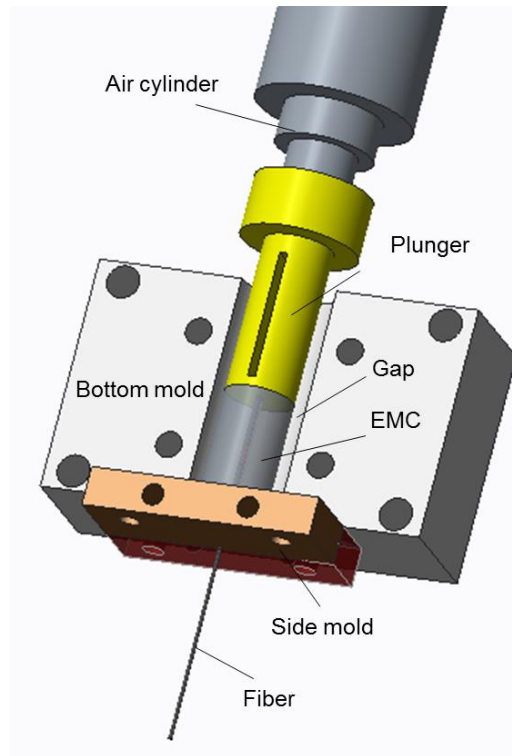
Figure 4.4 Setup of the compressive test

The specimen was heated to a target temperature first. When the BW is stabilized, a constant loading is applied and the BW shift is recorded by the interrogation system for around three minutes. The representative raw data obtained from compressive testing at 45°C, 125°C and 175°C are shown in Figure 4.5. In the plots, the constant BW before the pressure loading confirmed the temperature stability of the specimen. The BW dropped after the pressure was applied, and the ΔBW as a function of time was documented.

It should be noted that at temperature 45°C and 175°C, which were below and above glass transition temperature, the BW remained constant after the pressure was applied. However, at 125°C, which lied within the glass transition range, the BW continued to decrease after the pressure was applied due to the highly time-dependent behavior of the EMC near the glass transition temperature. Considering the resolution of the FBG interrogator about 1 pm, the ΔBW should be at least 100 pm to maintain the measurement uncertainty within 1%. The applied pressure normalized by the BW change (ΔBW) as a function of temperature is shown in Figure 4.6. The curve illustrates the stiffness change of the material as a function of temperature.
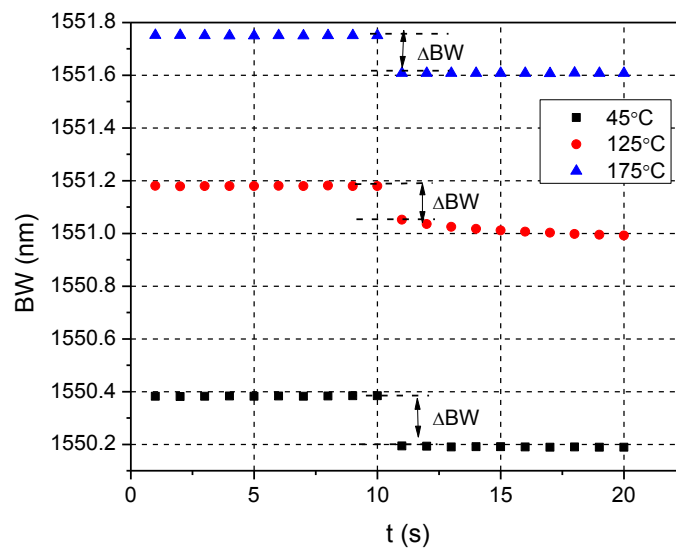
Figure 4.5 Raw data of the BW change at different temperatures

The time-temperature dependent raw data of the compressive creep test is shown in Figure 4.7. The temperature dependent Young's modulus at 1s is calculated using the code in appendix II and shown in Figure 4.8. The time temperature dependent Young's modulus is also calculated using the code shown in Figure 4.9. The modulus

changes rapidly with time over the glass transition range, where the polymer changes from glassy state to rubbery state. At temperatures below and above the glass transition range, however, the Young's modulus has negligible time-dependent behavior.
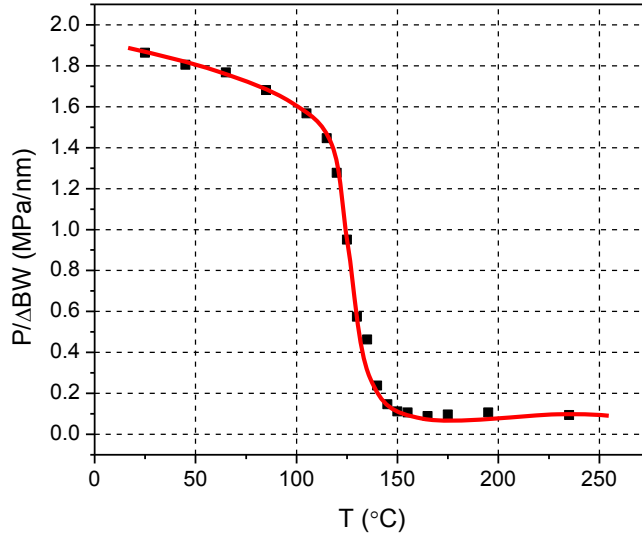
Figure 4.6 ΔBW at different temperatures from the compressive test
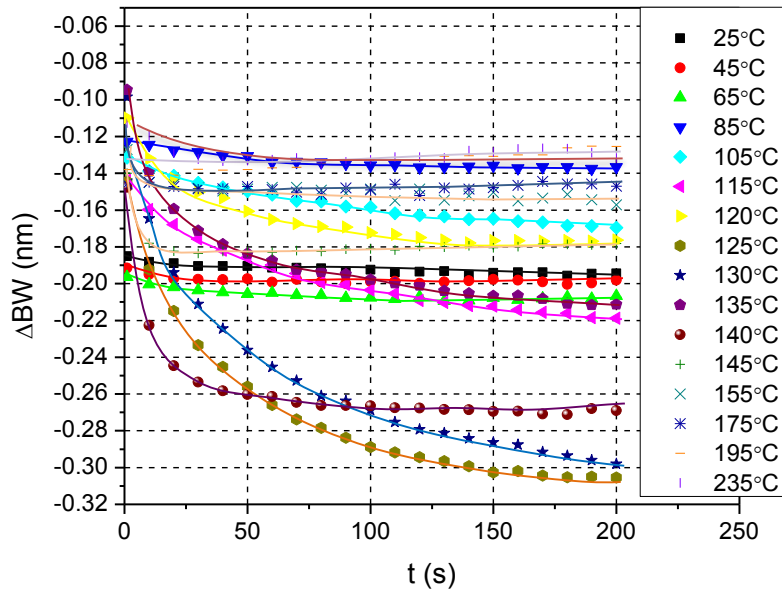
Figure 4.7 Raw data of the compressive creep test
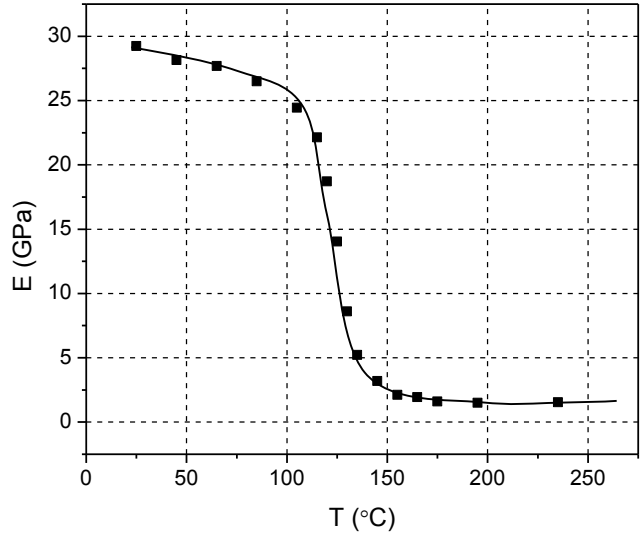
Figure 4.8 Temperature dependent Young's modulus
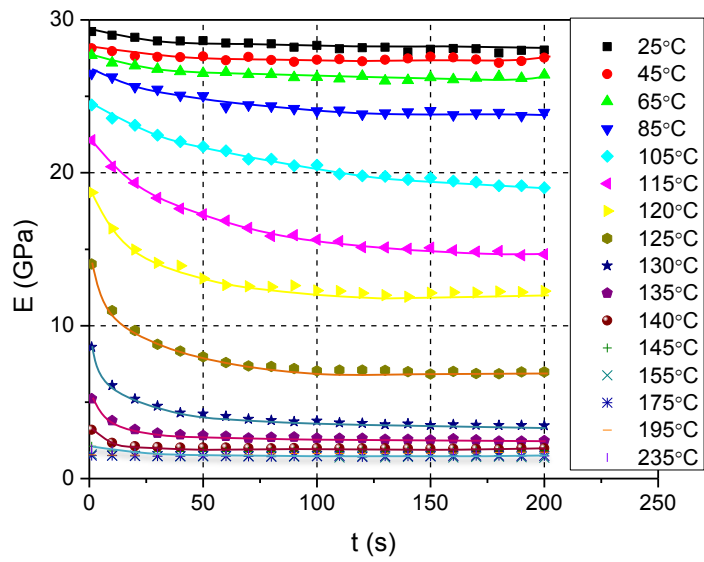
Figure 4.9 Time-temperature dependent Young's modulus

4.2.2. Time-temperature dependent bulk modulus measurement

4.2.2.1. High pressure system

Hydrostatic testing required much higher pressure than the pressure used in the curing setup (83 psi or ≈ 0.57 MPa).   A small test chamber was designed to

69

accommodate a high gas pressure for hydrostatic testing shown in Figure 4.10. The chamber was fabricated from Stainless Steel for tight tolerance required for sealing. The chamber has slightly larger diameter than the specimen, so that the specimen can sit freely in the chamber. The bottom of the mold is sealed by the side mold with small hole, allowing the fiber to penetrate. The hole is also sealed by a thin layer of Teflon tape after placing the fiber. The chamber was mounted on the same conduction heater as shown in Figure 3.32(a) to provide the temperature control. The top of the chamber is to connect to the gas pipe to provide high pressure to the chamber.

The hydrostatic pressure was provided by a custom-designed high pressure system, illustrated schematically in Figure 4.11. The Helium tank provided a gas pressure of approximately 2200 psi ($\approx$ 15. 2 MPa), which was controlled roughly by a regulator equipped with the tank. The output gas from the tank went through the main regulator (26-2015: Tescom) and was supplied to the test chamber. The main regulator was controlled by a pilot controller (ER3000: Tescom) with a transducer (100-1500: Tescom) that provided the feedback to the computer. The controller was connected to a PC which controlled and recorded the pressure. The output pressure to the test chamber was controlled with the accuracy of 1 psi ($\approx$ 6.9 KPa) and the target pressure was reached within 1s. The maximum pressure output to the test chamber was 1500 psi ($\approx$ 10.3 MPa).
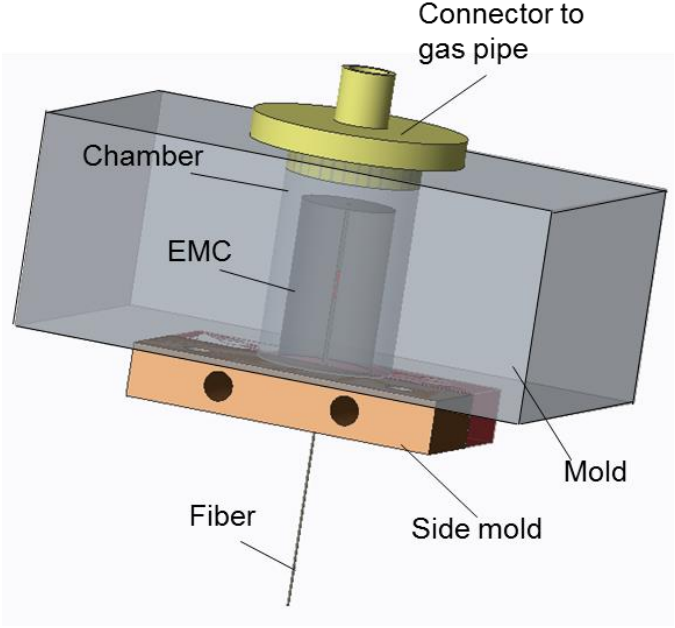
Figure 4.10 Mold of the hydrostatic test
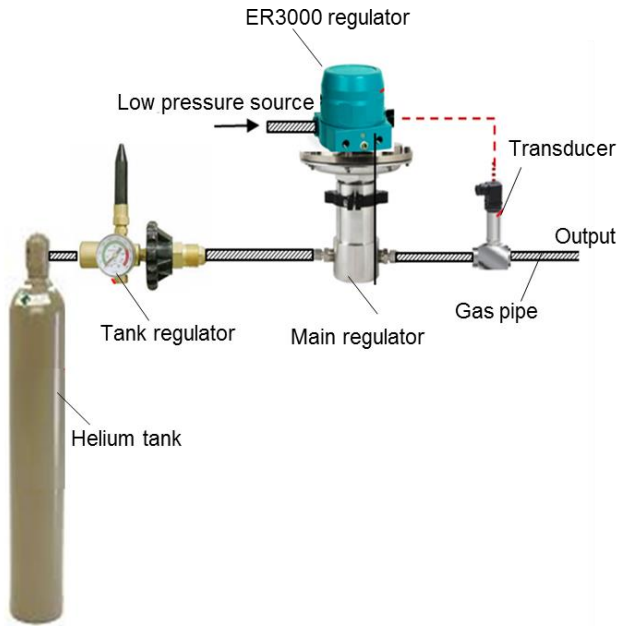
Figure 4.11 High pressure system

It is important to note that the heat is generated immediately after the targeted pressure is applied to the test chamber since the gas present in the chamber is suddenly compressed. The amount of heat generation can be estimated by [106]:

$$Q = \frac{5}{2}P_iV\left(\left(\frac{P_a}{P_i}\right)^{\frac{2}{7}} - 1\right)$$ (4.7)

where Q (J) is the heat generation, P_i (MPa) is the initial pressure, V (mm^3) is the volume of the gas in the chamber (i.e., the chamber volume – the specimen volume) and P_a (MPa) is the applied pressure.

This undesired heat produces the thermal expansion of the specimen, which offsets the hydrostatic strain of the specimen. The results obtained from the initial design of the chamber are shown in Figure 4.12, which shows the BW after the hydrostatic pressure is applied. The BW increase caused by the thermal expansion of the specimen is evident.

In practice, the thermal strain caused by $\Delta T < 0.1$ °C is negligible compared to the hydrostatic strain. Considering the specific heat ($\approx$ 1J/gK) and the thermal conductivity ($\approx$ 1W/mK [107]) of the EMC, the heat generation should be smaller than 0.5 J. Using Eq. (4.7), the corresponding air volume is determined to be 1000 mm^3 at the maximum pressure of 1500 psi (10.5 MPa). The internal volume of the final chamber was around 1800 mm^3 and the volume of the specimen was 910 mm^3; the net air volume was 890 mm^3. The effect of the heat generation was virtually negated with the internal air volume less than 1000 mm^3.
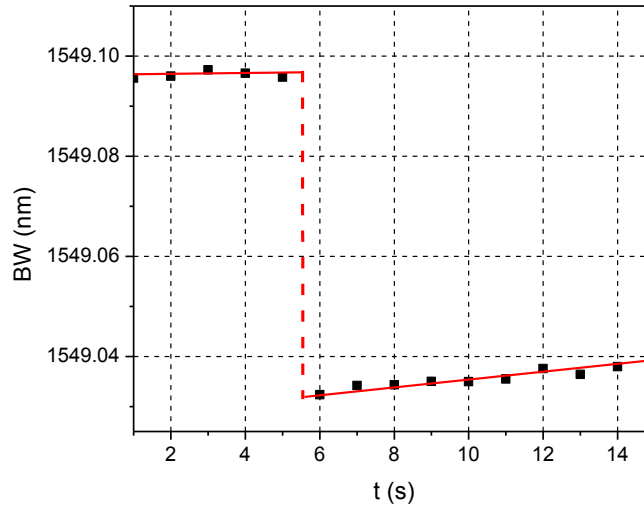
Figure 4.12 BW as a function of time after a high pressure is applied

The same specimen was subjected to hydrostatic testing using the setup shown in Figure 4.11. The representative raw data obtained from hydrostatic testing at 45°C, 125°C and 175°C are shown in Figure 4.13. In the plots, the constant BW before the pressure loading confirmed the temperature stability of the specimen. The BW dropped after the pressure was applied, and the ΔBW was documented. As expected, a similar time-dependent behavior was observed. The applied pressure normalized by BW change (ΔBW) as a function of temperature is shown in Figure 4.14. The curve illustrates the volumetric stiffness change as a function of temperature.
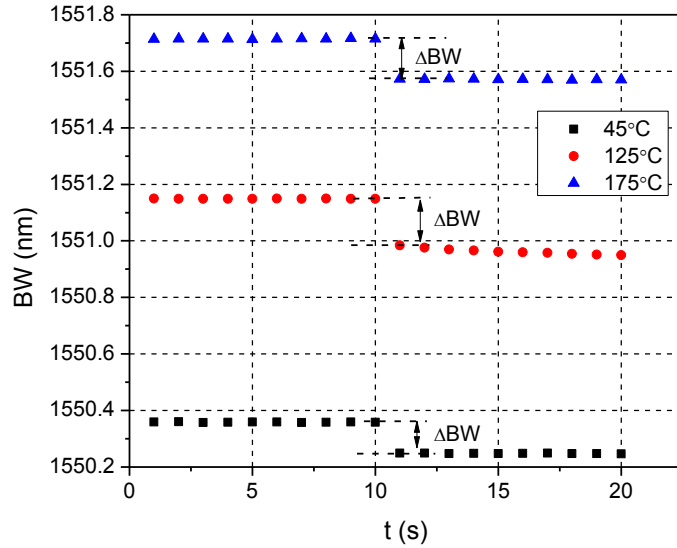
Figure 4.13 Raw data of the BW change at different temperatures
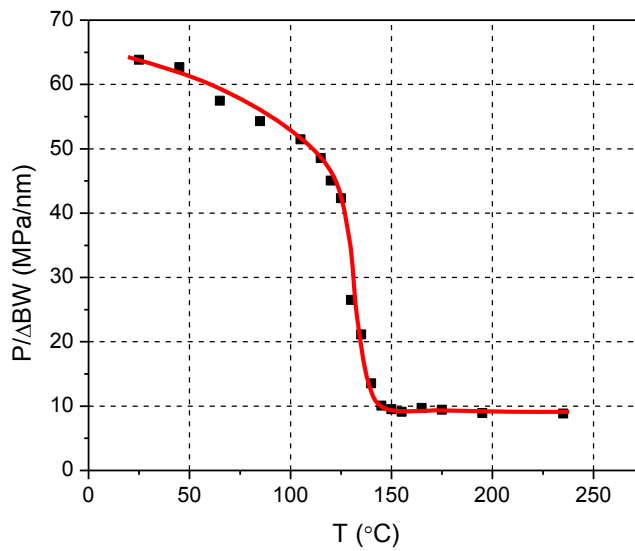
Figure 4.14 ΔBW at different temperatures from the compressive test

With the high pressure system, the time-temperature dependent raw data of the BW shift is shown in Figure 4.15. The temperature dependent bulk modulus is calculated and shown in Figure 4.16. The time-temperature dependent bulk modulus at 1s is shown in Figure 4.17. It should be noted that the pressure is released after creep

at each temperature and the elastic strain will recover instantaneous. When the temperature increases to the next step, the total strain in the specimen also increase to compensate the creep strain. The bulk modulus also shows strong time-dependent behavior over the glass transition temperature range.
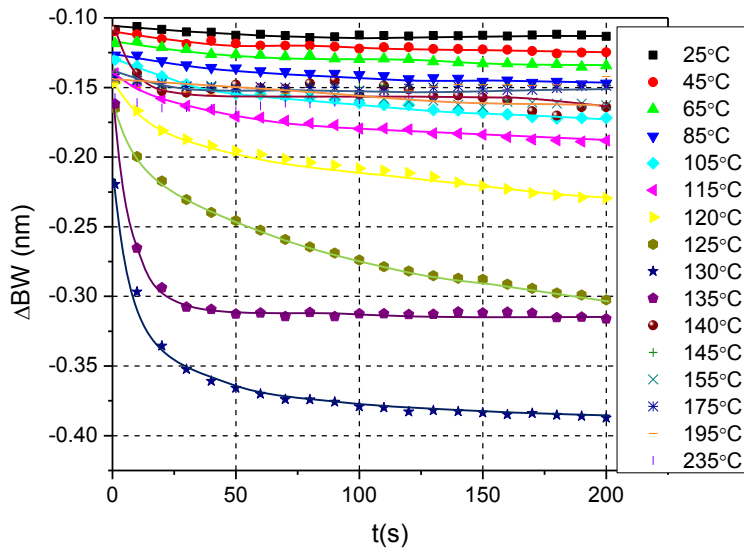
Figure 4.15 Raw data of the hydrostatic creep test
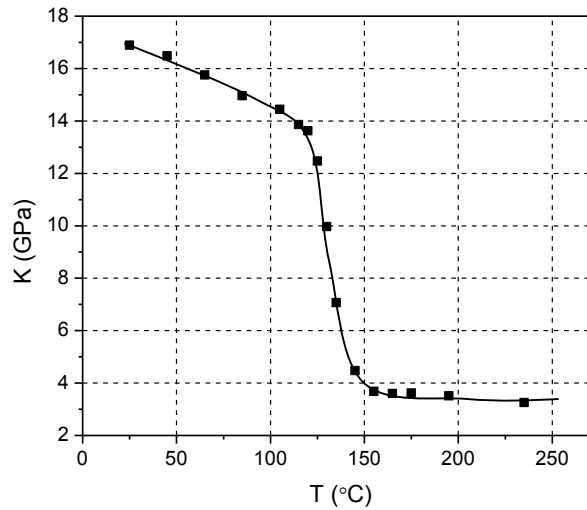
Figure 4.16 Temperature dependent bulk modulus
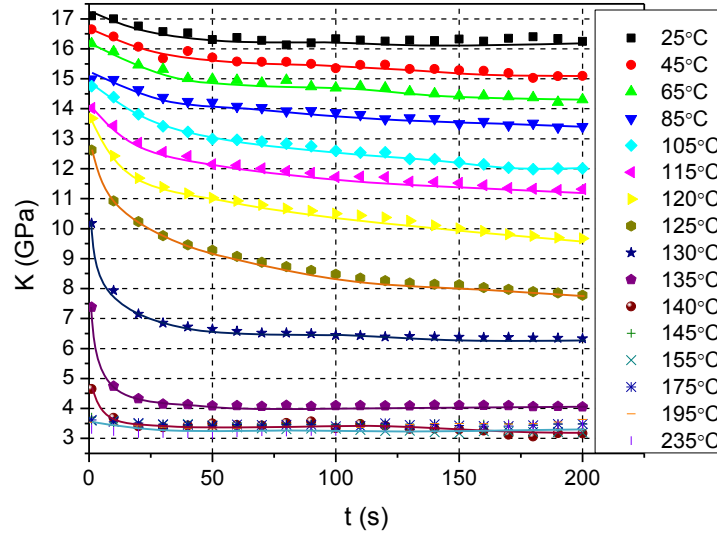
Figure 4.17 Time-temperature dependent bulk modulus

4.2.3. Temperature Dependent Properties

The shear modulus and Poisson's ratio can be calculated using Eq. (4.2). The temperature dependent elastic properties of the material are shown in Figure 4.18. The Young's modulus, bulk modulus and shear modulus decrease as a function of temperature, while the Poisson's ratio increases. The Young's modulus is larger than the bulk modulus when the Poisson's ratio is smaller than 1/3. The Poisson's ratio is around 0.21 below 100°C and 0.43 above 170°C. The shear modulus is always smaller than the Young's modulus and the bulk modulus.
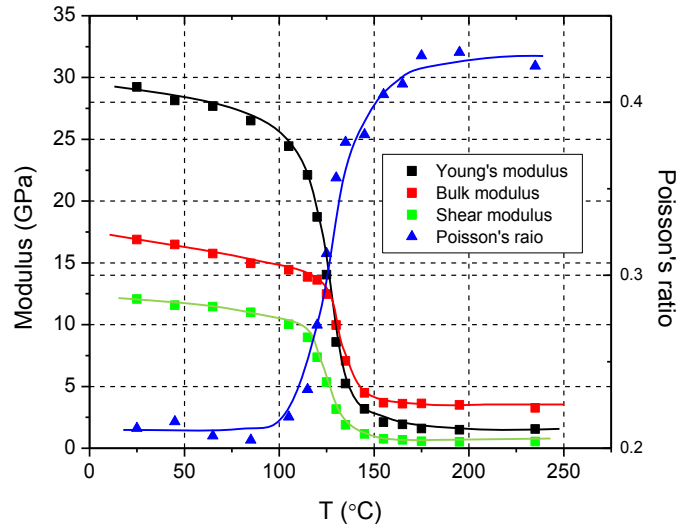
Figure 4.18 Temperature dependent elastic properties

4.2.4. Shift factors and master curve

The time temperature superposition is based on the assumption of thermorheologically simple, which means no change in relaxation mechanism occurs with temperature. As shown in Figure 4.19(a), the shape of the relaxed modulus at different temperatures is the same in the log time scale. Experimentally, only part of the curve can be measured as shown in Figure 4.19(b). These parts at different temperatures can be shifted and overlapped as shown in Figure 4.19(c). The amount of shifting is called shift factor. The process can be repeated at different temperatures and the master curve can be created.
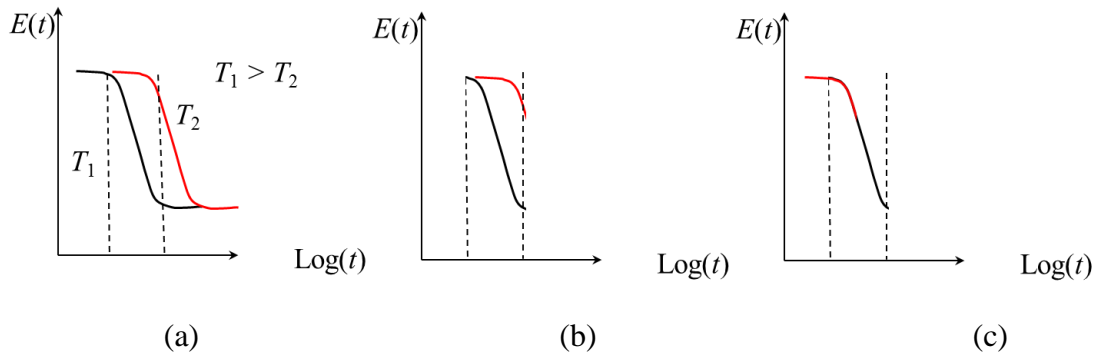
Figure 4.19 Time temperature superposition

The Young's modulus are shifted and overlapped to form the master curve as shown in Figure 4.20, where the reference temperature is 25°C. The shift factors are presented in Figure 4.21. Using the same shift factors, the master curve of the bulk modulus is created and presented in Figure 4.22, indicating that it has only one relaxation mechanism and the TRS assumption is valid for this material.
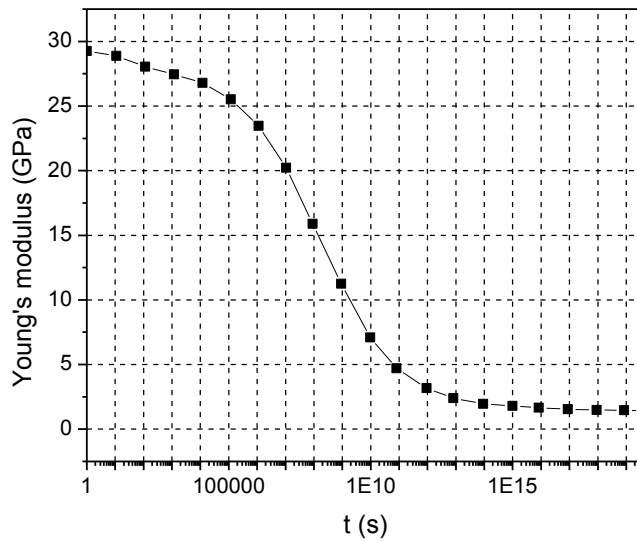
Figure 4.20 the master curve of the Young's modulus
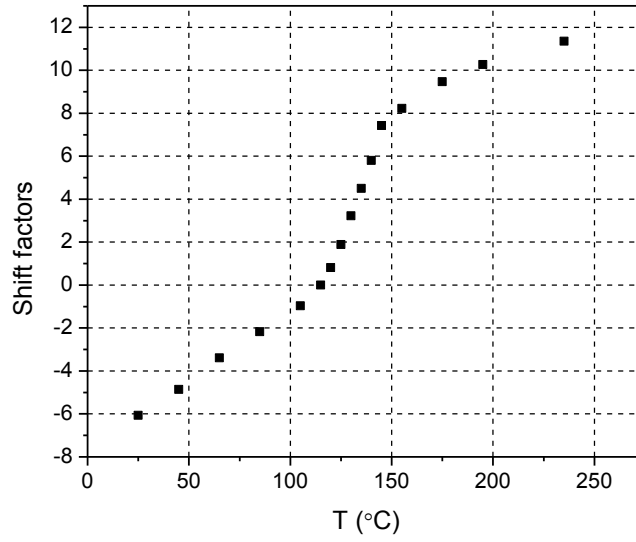
Figure 4.21 the shift factors
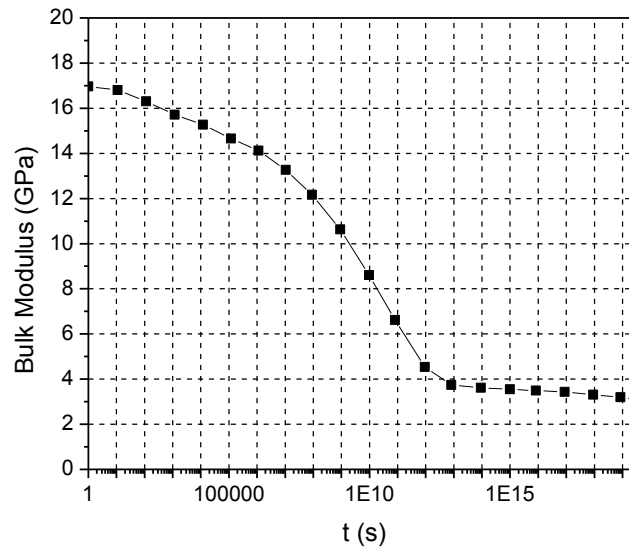
Figure 4.22 the master curve of the bulk modulus

4.2.5. Comprehensive viscoelastic model

In the FEM modelling, the shear modulus and bulk modulus will be used as inputs. The shear modulus can be calculated from the equation (4.2) and plotted in Figure 4.23. The bulk modulus and shear modulus are fitted by the prony series:

$$K(t) = K_\infty + \sum_{i=1}^{20} K_i \exp\left(-\frac{t}{\tau_i}\right)$$
$$G(t) = G_\infty + \sum_{i=1}^{20} G_i \exp\left(-\frac{t}{\tau_i}\right)$$

(4.8)

The coefficients of the prony series are listed in Table 2.

Table 2 The coefficients of the Prony series

i	τ_i(s)	K_i(GPa)	G_i(GPa)
1	1E20	0.40	0.11
2	1E19	0	0.02
3	1E18	0.2	0.04
4	1E17	0.04	0.07
5	1E16	0.05	0.16
6	1E15	0.06	0.18
7	1E14	0.08	0.11
8	1E13	0.17	0.79
9	1E12	1.80	0.99
10	1E11	2.43	2.10
11	1E10	1.97	3.58
12	1E9	1.76	4.99
13	1E8	1.16	4.71
14	1E7	1.06	4.13
15	1E6	0.54	2.21
16	7e4	0.84	1.30
17	1018	0.67	0.43
18	1015	0.29	0.50
19	34.5	0.60	1.06
20	1.3	0.12	0.23
∞		2.80	1.32

The shift factors are fitted by the piece-wise shift functions shown in Figure 4.24. The WLF function was used for the temperatures in the glass transition range

[74]; while the polynomial functions are used for the temperatures below and above glass transition temperature[67] :

$$\log a_T = 0.088(T-378)+0.0001(T-378)^2+8.36\text{e-}006(T-378)^3, T \le 378$$

$$\log a_T = \frac{-19.46(T-378)}{-169.6+T-378}, 378 \le T \le 418 \tag{4.9}$$

$$\log a_T = 0.14(T-378)+0.00125(T-378)^2\text{ -}2.5\text{e-}005(T-378)^3, T \ge 418$$
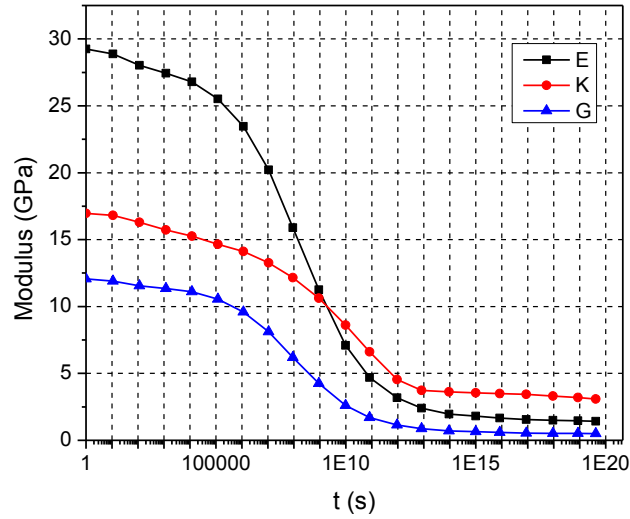
Figure 4.23 Prony series of the Young's modulus, bulk modulus and shear modulus
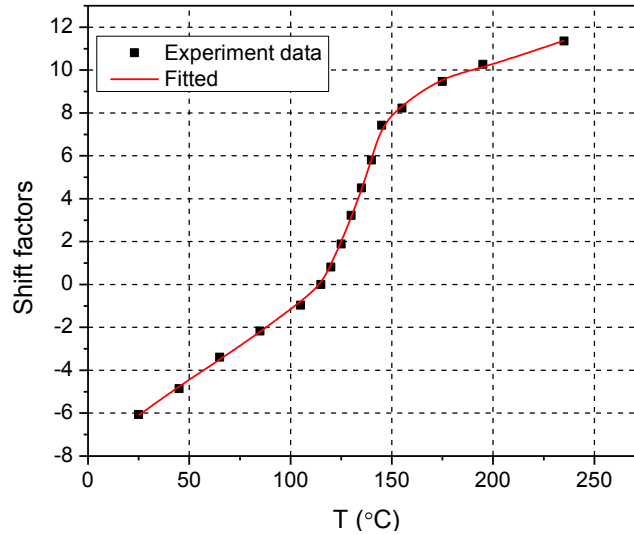
Figure 4.24 Piece-wise shift functions

81

4.2.6. Comparison between prediction and measured properties

The coefficients of the prony series and the piece-wise shift functions are used as inputs in FEM for the prediction of the experiment data. The user defined subroutine was used to apply the piece-wise shift function in ANSYS. Using the coefficients of the prony series and the shift function in FEM user subroutine, predict the experiment data by the FEM model. The predicted results at four different temperatures: below glass transition, glass transition and above glass transition, are compared with the experiment results as illustrated in Figure 4.25. The plot shows very good agreement between the predicted results and the experiment data, confirming that the measured properties are accurately represented by the master curve and the shift functions. The comprehensive viscoelastic properties can be used for the EMC modelling at various temperatures.
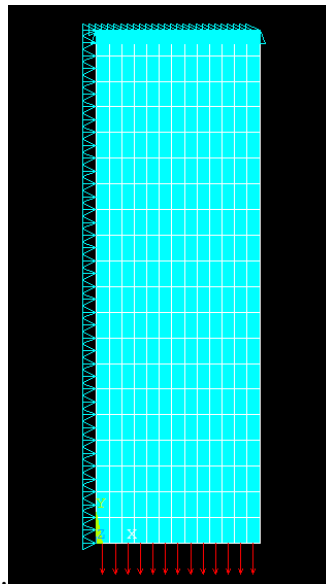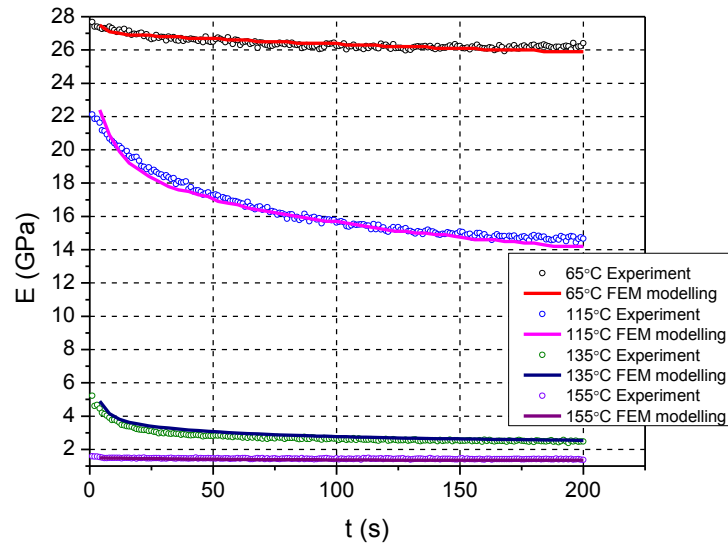
Figure 4.25 Comparison between the prediction and experiment data

4.3. Assumptions verification

4.3.1. Assumption one: Thermorheologically simple

The time-temperature superposition process is based on the thermorheologically simple (TRS) assumption. The assumption states that the shapes of the master curve are the same in the log time scale at different temperatures. This assumption is not always valid to all the polymeric materials [60, 108-111] and it is necessary to verify that this assumption is valid for the EMC material.

An extra long-term creep test was conducted at 125°C for roughly 4 hours as the long term test. The temperature was chosen to obtain the most obvious viscoelastic behavior. The time dependent Young's modulus from the long-term creep test is shown in Figure 4.26. The data was replotted in the log-time scale and is compared with the master curve in Figure 4.27. It is evident that the long term creep data overlaps with

83

the master curve very well, which confirms that the TRS assumption is valid for the advanced EMC material tested in the study.
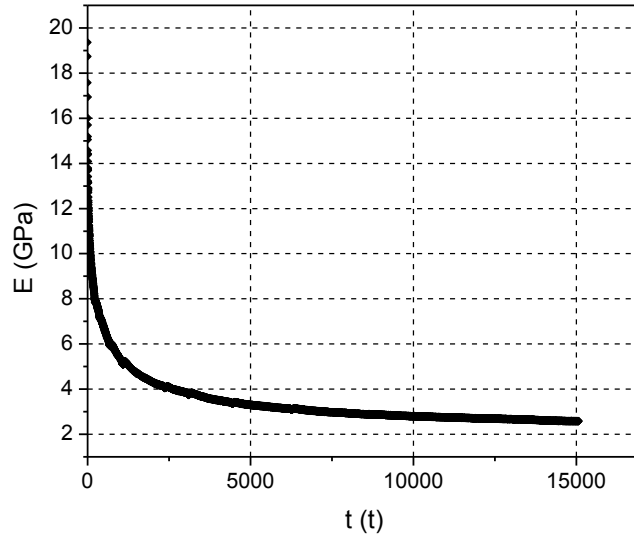
Figure 4.26 Young's modulus at long term
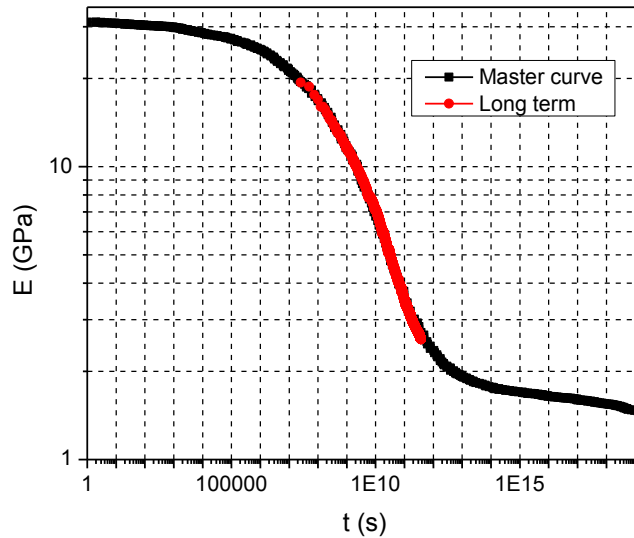
Figure 4.27 Comparison with the master curve in the log-time scale

4.3.2. Assumption two: Boltzmann superposition principle

The Boltzmann superposition principle states that "in the linear viscoelastic regime the strain response to successive stress are additive". It is the key to develop

the linear viscoelastic constitutive law. In order to verify this assumption, a supplementary experiment was conducted at 130°C with a step loading. A pressure of 0.07 MPa was applied at $t = 0$ and an additional pressure of 0.07 MPa (a total of 0.14 MPa) was applied at $t = 100$ s. The BW change measured during the whole process was documented. Based on the BSP, the strain change due to the step loading can be calculated from the equation:

$$\varepsilon(t) = J(t) \cdot \sigma + J(t - \tau) \cdot \Delta\sigma \qquad (4.10)$$

where $\varepsilon(t)$ is the strain change as a function of time; $J(t)$ is the time-dependent compliance which can be determined from the time-dependent Young's modulus; σ and $\Delta\sigma$ are the applied stress. The BW change can be calculated from $\varepsilon(t)$. The measured results are compared with the predicted values in Figure 4.28. The measured values match extremely well to the predicted values indicating the validity of Boltzmann superposition principle for the material.
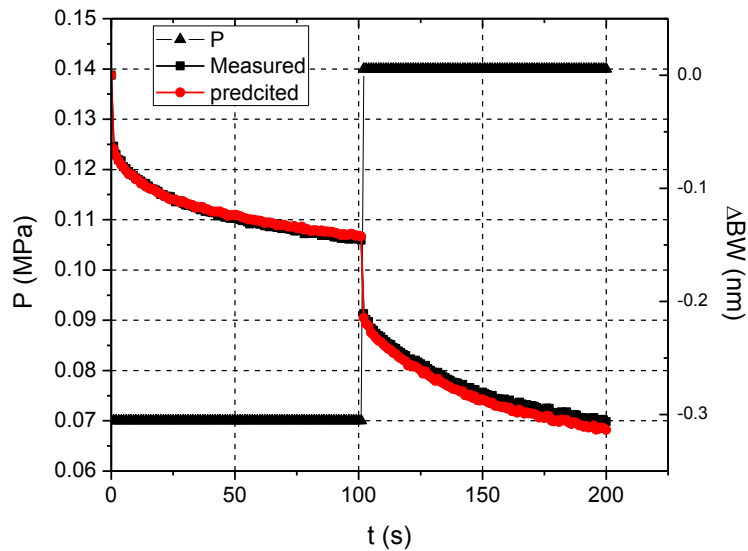
Figure 4.28 Boltzmann superposition principle validation

4.3.3. Assumption three: linear viscoelastic

In the domain of linear viscoelastic behavior, the time-dependent (or reduced) modulus should be independent of the applied stress level. In this supplementary experiment, three different stress levels are applied to the specimen at 130°C and the BW is shown in Figure 4.29(a). The Young's modulus is calculated from the BW and shown in Figure 4.29(b). The measured time dependent Young's modulus is independent of the applied stress, confirming that the linear viscoelastic assumption works for the material.

The linear viscoelastic assumption is applicable to certain strain level and after that the nonlinear viscoelastic model should be considered [112, 113]. The linear range is investigated using the specimen. The EMC shows reasonably linear behavior at the strain level until 2000 micro strain shown in Figure 4.30.
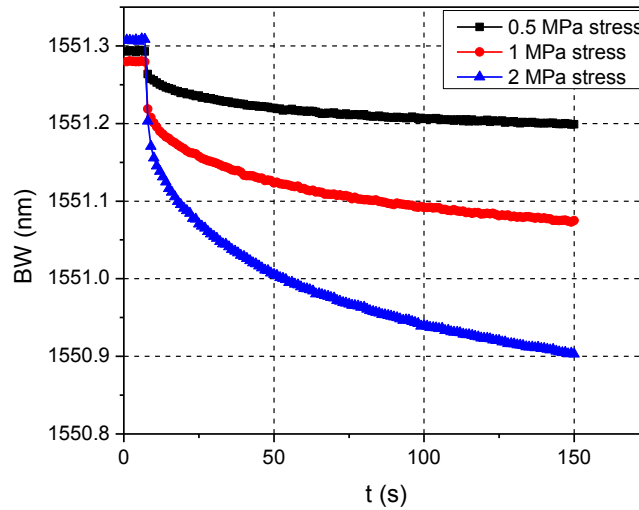
(a)
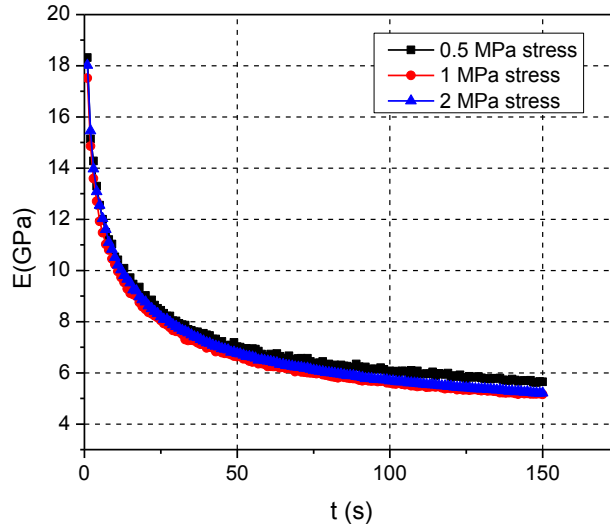
(b)

Figure 4.29 Time dependent behavior at different stress level (a) BW (b)

Young'smodulus

The linear viscoelastic assumption is applicable to certain strain level and after

that the nonlinear viscoelastic model should be considered [112, 113]. The linear range

is investigated using the specimen. The EMC shows reasonably linear behavior at the

strain level until 2000 micro strain shown in Figure 4.30.
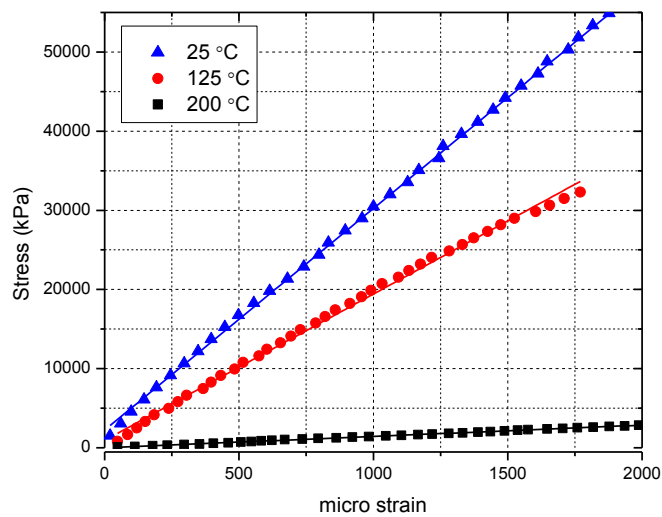
Figure 4.30 Linear limit test

4.4. Properties verification

The temperature dependent Young's modulus was verified by a three point bending test. In order to verify the time-temperature dependent properties, two optical techniques are implemented: shadow moiré to verify the temperature dependent properties and the Twyman/Green to verify the rate dependent viscoelasticity. The procedure to verify the properties are presented in this section.

4.4.1. Temperature dependent properties verification

A three point bending test was developed to verify the measured Young's modulus. The dimension of the specimen is: length $l = 25$ mm, width $w = 6.7$ mm and thickness $t = 0.8$ mm. The temperature dependent Young's modulus from the three point bending test is shown and compared with the FBG results in Figure 4.31. The results show the accuracy of the measured properties by the FBG method.
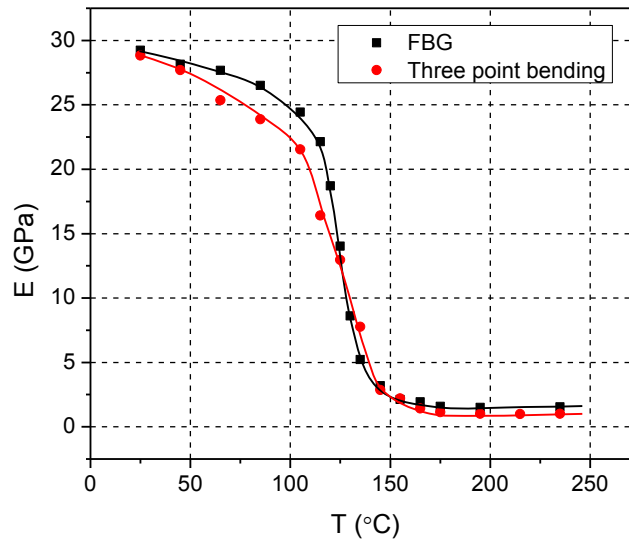
Figure 4.31 Comparison of the temperature dependent Young's modulus

4.4.2. Shadow moiré measurement

The bi-material specimen shown in Figure 4.32 with a layer of the silicon chip and EMC is used for the warpage measurement at different temperatures. The dimension of the specimen is: $l = 30\,\text{mm}$, $w = 3\,\text{mm}$, $t_{EMC} = 0.4\,\text{mm}$ and $t_{si} = 0.4\,\text{mm}$. The setup of the shadow moiré is shown in Figure 4.33. The specimen is mounted on the TEC heater with the maximum heating rate of 80°C/min. The camera is perpendicular to the specimen surface and the light source is 45° off the camera. The warpage change of the specimen is measured by the shadow moire shown in Figure 4.33. The governing equation of the shadow moire is:

$$z = gN \tag{4.11}$$

Where z is the out of plane displacement; g is the grating pitch; N is the fringe order.
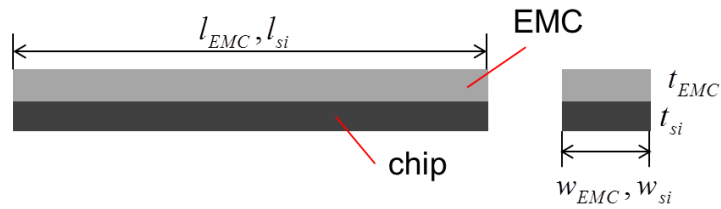
Figure 4.32 Bi-material specimen
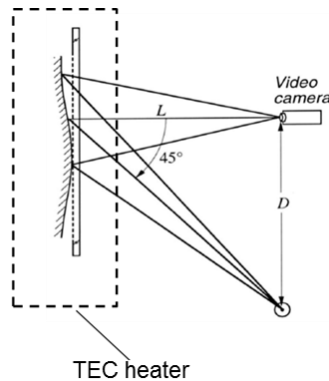
Figure 4.33 Shadow moiré setup

Heat the specimen from 25°C to 150°C with the maximum rate of the TEC, 80°C/min covering the glass transition temperature. The fast heating rate is implemented to minimize the time dependency of the properties. The warpage of the specimen is measured at every 25°C shown in Figure 4.34. The counter interval is 25 μm/fringe.
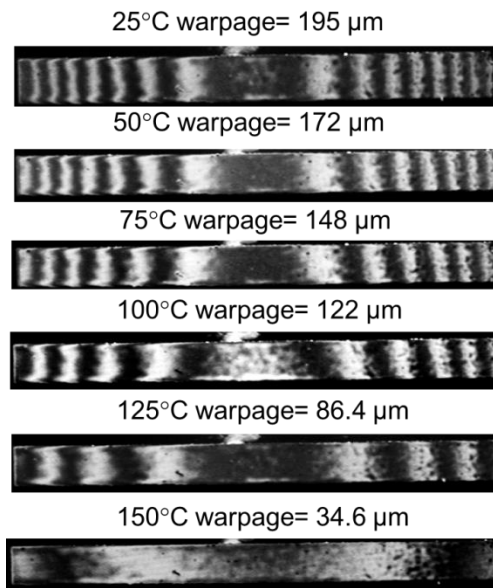
Figure 4.34 Temperature dependent warpage

The same configuration of the specimen is created in FEM and the comprehensive viscoelasticity is used for the EMC. The CTE of the EMC is measured by TMA: $CTE1 = 8$ ppm/°C, $CTE2 = 40$ ppm/°C and $T_g = 128$ °C. The input properties for the chip are: $E_{si} = 112$ GPa, $v_{si} = 0.28$, $CTE_{si} = 2.6$ ppm/°C. The predicted warpage is compared with the measured warpage in Figure 4.35.
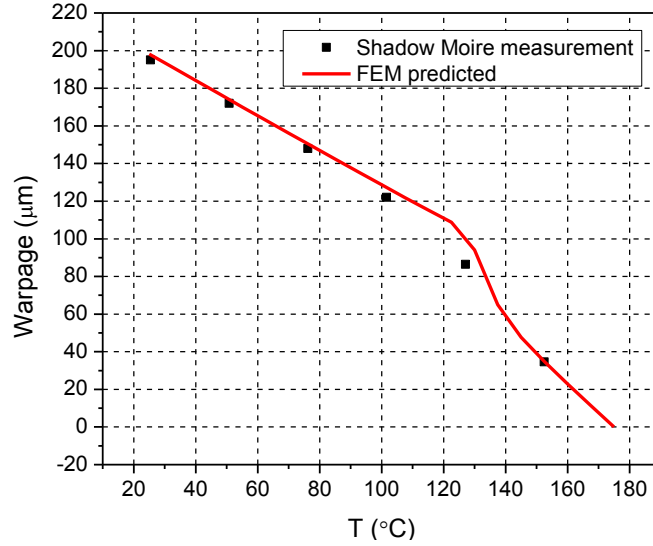
Figure 4.35 Warpage change comparison between FEM and experiment

4.4.3. Twyman/Green Measurement

Shadow moire test is not applicable to verify the rate dependent viscoelasticity due to the large counter interval (25μm/fringe) with the current specimen. Twyman/Green test is implemented to measure the rate dependent warpage with high resolution.

A bi-material specimen with different dimension is used for the T/G test: $l = 20$ mm, $w = 2$ mm, $t_{EMC} = 0.2$ mm and $t_{si} = 0.6$ mm. The setup of the T/G is shown in Figure 4.36. The specimen is placed on the conduction heater covered by a small chamber to eliminate the air during temperature change. The governing equation of the Twyman/Green test is:

$$z = \frac{\lambda}{2} N \qquad (4.12)$$

Where λ the wavelength of the light, the contour interval is 0.316 µm/fringe.

91
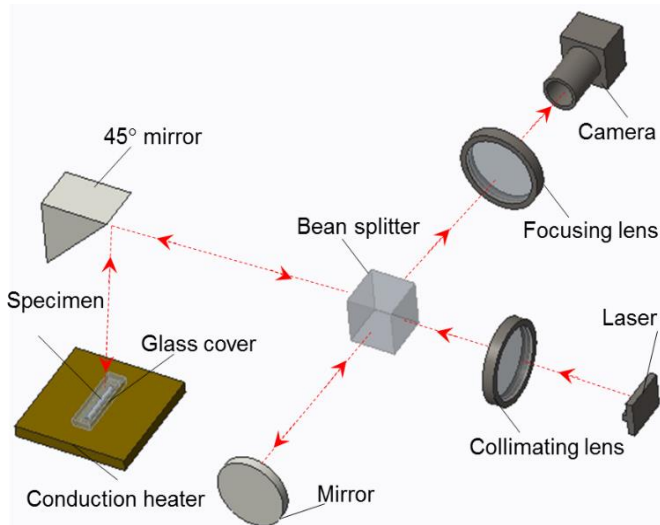
Figure 4.36 T/G setup

The temperature changes from 175°C (curing temperature) to 25°C with two different rates: 20°C/min and 1°C/min. A thermocouple is attached to heater close to the specimen. The temperature profile is shown in Figure 4.37. The representative fringes at 175°C, 135°C, 115°C, 55°C and 25°C are shown in Figure 4.38 with half specimen.
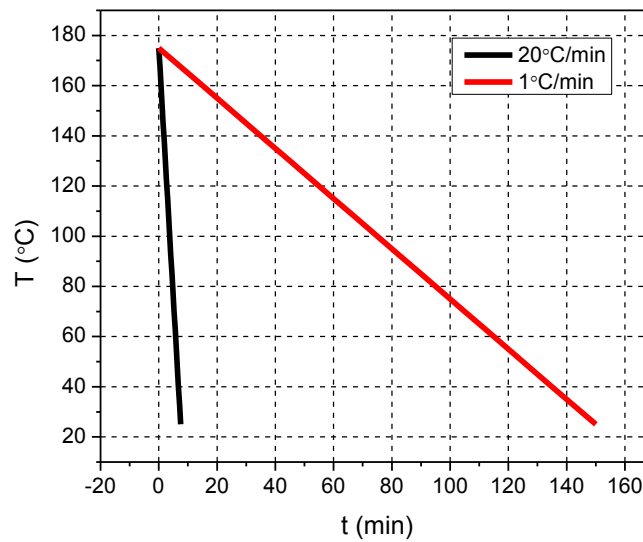
Figure 4.37 Temperature profile of the T/G test
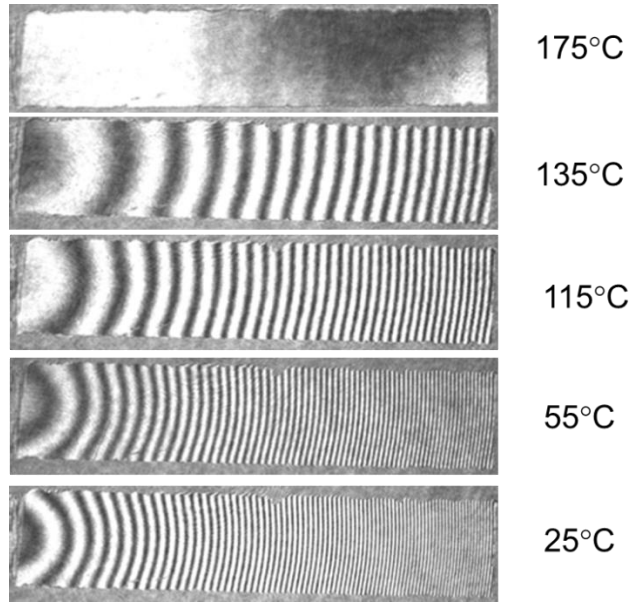
Figure 4.38 Temperature dependent fringes

The temperature dependent warpage shows clear rate dependency in Figure 4.39. The higher rate shows higher warpage due to shorter time for relaxation.
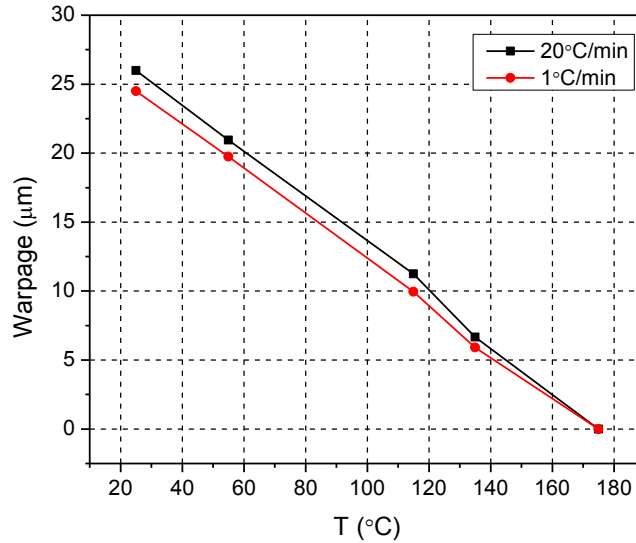
Figure 4.39 Rate dependent warpage

A FEM model is created to verify the viscoelasticity of the material. The 3D model is shown in Figure 4.40. The same temperature loading as Figure 4.37 is applied in the model. The representative contours in the model matches well to the fringes in

Figure 4.41. The rate dependent warpage matches well between the experiment and the prediction, confirming the validation of the measured properties.
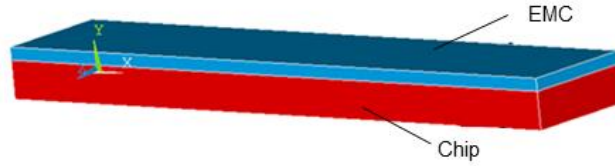
Figure 4.40 3D model of the bi-material specimen
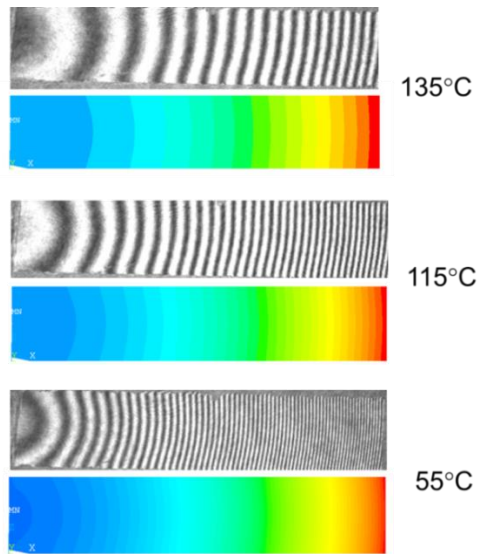
Figure 4.41 Comparison between the contours and the fringes
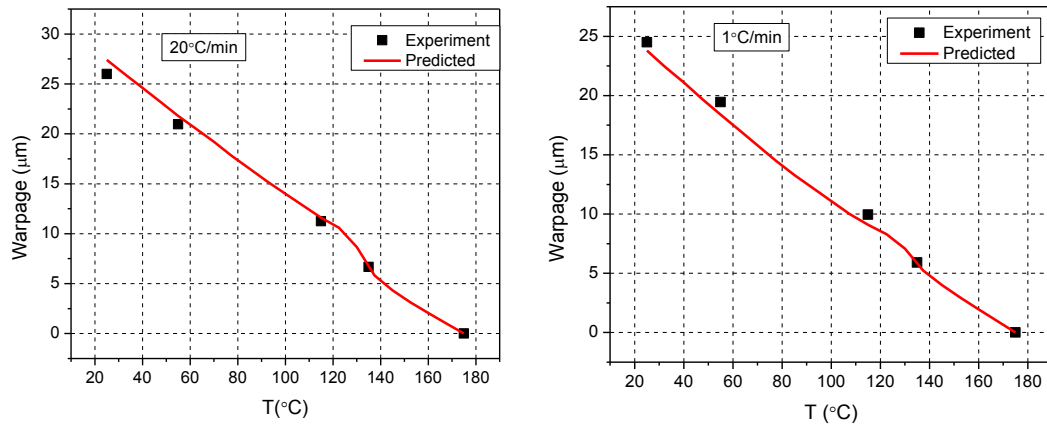
Figure 4.42 Rate dependent warpage comparison between FEM and experiment

4.5. Temperature dependent CTE and CHS

4.5.1. Infinite configuration

When the cylindrical configuration, shown in Figure 3.2, is subjected to an external strain, a part of the strain is transferred to the embedded FBG. The amount of strain measured by the FBG is strongly dependent on the ratio of the volume stiffness between the material used to fabricate the cylindrical configuration and the fiber. From the definition of the volume stiffness (defined as "volume multiplied by modulus"), the volume stiffness ratio, R_{VS}, can be defined as:

$$R_{VS} = \frac{E_s\left(r_s^2 - r_f^2\right)}{E_f \cdot r_f^2} \tag{4.13}$$

where E_s and E_f are the modulus of the material and the fiber, respectively.

The measured strain normalized by the applied strain is shown as a function of the volume stiffness ratio in Figure 4.43. As the volume stiffness ratio increases, the normalized measured strain converges to "unity" (indicated by the red line in the plot); i.e., for the configuration with the ratio greater than 200 (will be referred to as "infinite configuration"), the measured strain becomes virtually the same as the applied strain. Under this condition, the CTE or CHS of the material can be determined by using this "single" infinite configuration. To achieve this condition, some authors used a very large substrate diameter $\left(\frac{r_s}{r_f} \gg 1\right)$ [90, 114], while others took advantage of the large modulus of a substrate material $\left(\frac{E_s}{E_f} \gg 1\right)$ [92].
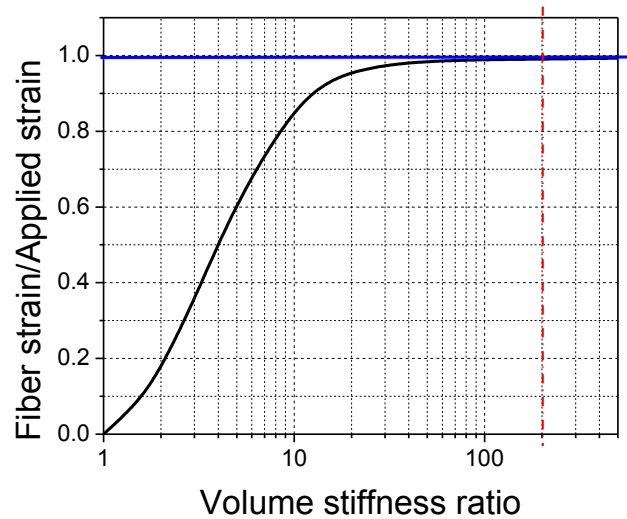
Figure 4.43 Infinite configurations

The modulus of the polymer decreases rapidly with temperature, especially above the glass transition temperature. Consequently, a very large substrate diameter will have to be used when the properties of polymers are to be determined over a wide range of temperature. It is important to note that the applicability of this large configuration is limited in practice only to polymers that produce very small heat generation; otherwise, an excessive amount of heat generated during curing would produce a large temperature gradient within the specimen, leading to non-uniform material property or undesired residual stresses.

The concept of the dual-configuration FBG sensor method [20] is adopted and advanced to measure the CTE and CHS of polymeric materials under various environmental conditions. The behavior of the infinite configuration is reconstructed numerically from the two small finite configurations that are subjected to environmental conditions. Then, the coefficients can be determined from the simple governing equation derived for the infinite configuration. The small configurations

96

negate the effect of heat generation during curing, which makes the method applicable for a wide range of polymeric materials.

4.5.2. Reconstruction of infinite configuration

The Bragg wavelength shift ratio, κ, of the infinite configuration to a finite configuration β can be defined as:

$$\kappa = \frac{\Delta\lambda_d\big|_{\beta=\infty}}{\Delta\lambda_d\big|_{\beta}} \tag{4.14}$$

By substituting Eq. (3.11) into Eq.(4.14), the ratio, κ, can be expressed as:

$$\kappa(E,\beta) = \frac{F(E_s,\infty)}{F(E_s,\beta)} \tag{4.15}$$

The coefficient κ depends only on the polymer modulus and the configuration; i.e., it remains the same regardless of the deformation state of the polymer. For a given configuration β, the coefficient κ becomes a polymer modulus dependent parameter.

The polymer modulus dependent κ values for four most practical configurations, $\beta = 20$ (2.5 mm for the 125 µm fiber), 30, 40 and 50, are shown in Figure 4.44. The polymer modulus ranges from 100 MPa to 10 GPa, which covers the most engineering polymers [29]. The typical material properties of the fiber were used for the calculation; the modulus of 73 GPa and Poisson's ratio of 0.17.

The value of κ can be determined from the plot in Figure 4.44 only when the polymer modulus is known. In the actual application, it is not always possible to determine the value of κ from the plot since the polymer modulus can change during the environmental loading.
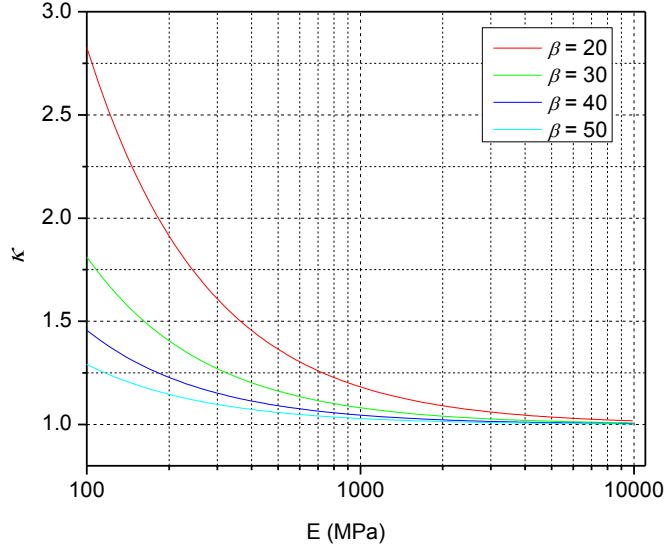
Figure 4.44 Modulus dependent κ with different configurations

In order to cope with the problem, another parameter is defined. Let us consider a smaller configuration β_2 (the first one is now called β_1 and $\beta_1 > \beta_2$). If the two configurations are subjected to the same deformations, the second parameter, which is the ratio of the BW shifts between the two configurations, can be defined as:

$$\eta = \frac{\Delta\lambda_d\big|_{\beta=\beta_1}}{\Delta\lambda_d\big|_{\beta=\beta_2}} = \frac{F(E_s,\beta_1)}{F(E_s,\beta_2)} \tag{4.16}$$

It is worth noting that this ratio is also independent of the deformation state of the polymer, but, unlike the coefficient κ, it is determined directly from the experiment.

For a given set of configurations, β_1 and β_2, η becomes a polymer modulus dependent parameter. The modulus dependent behavior of η is plotted in Figure 4.45, where various cases of β_1/β_2 ratios are shown for β_2 of (a) 10, (b) 20 and (c) 30.

98

As mentioned earlier, the coefficients κ and η are dependent only on the polymer modulus for a given set of configurations, and they are related to each other in the following way:

$$\eta = \frac{F(E_s, \beta_1)}{F(E_s, \beta_2)} = \frac{F(E_s, \beta_1)}{F(E_s, \beta_\infty)} \cdot \frac{F(E_s, \beta_\infty)}{F(E_s, \beta_2)} = \frac{\kappa|_{\beta=\beta_2}}{\kappa|_{\beta=\beta_1}} \tag{4.17}$$

An analytical relation can be defined to relate these two parameters as

$$\kappa = g(\eta) \tag{4.18}$$

The relationship between κ and η are shown in Figure 4.46, where various cases of β_1/β_2 ratios are shown for β_2 of (a) 10, (b) 20, and (c) 30.

In the actual experiment, the value of η is first determined from the experimental data using Eq. (4.15). The corresponding κ can be determined using Eq. (4.18) (or the plot in Figure 4.46). After calculating the BW shifts in the infinite configuration (i.e., $\Delta\lambda_d|_{\beta=\infty}$) using Eq.(4.14), the strain of the polymer can be finally determined from Eq. (3.11).
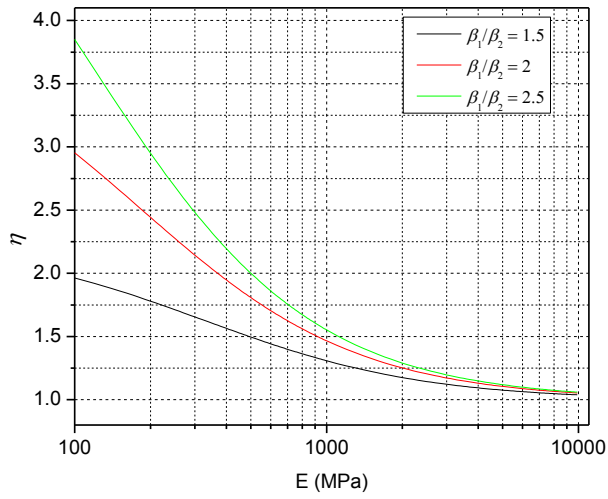
(a) $\beta_2 = 10$
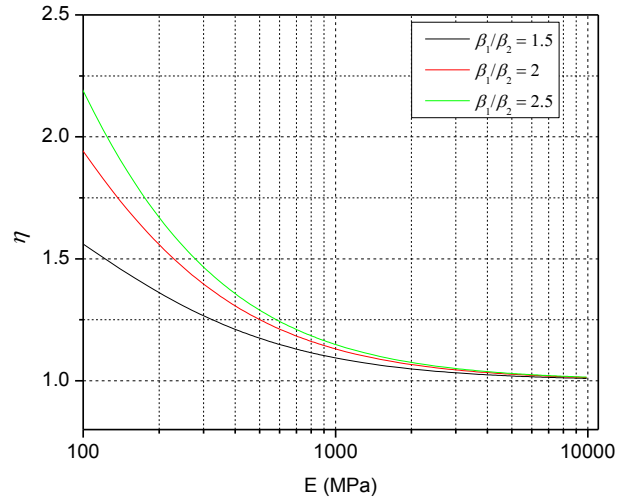
(b) $\beta_2 = 20$
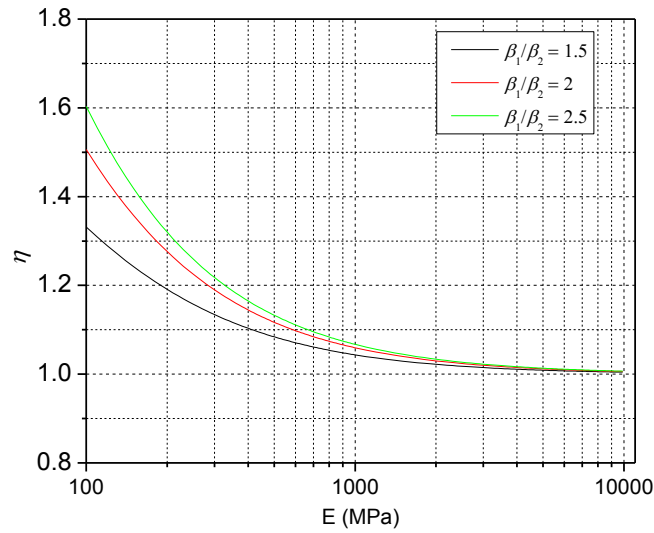
(c) $\beta_2 = 30$

Figure 4.45 Modulus dependent η with different configurations: (a) $\beta_2 = 10$, (b) $\beta_2 = 20$ and (c) $\beta_2 = 30$
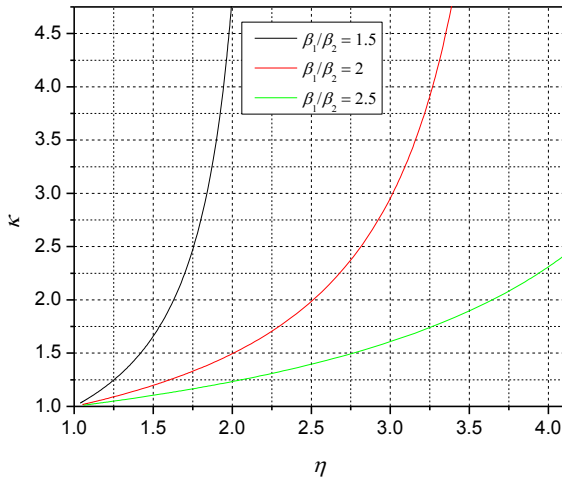
(a) $\beta_2 = 10$
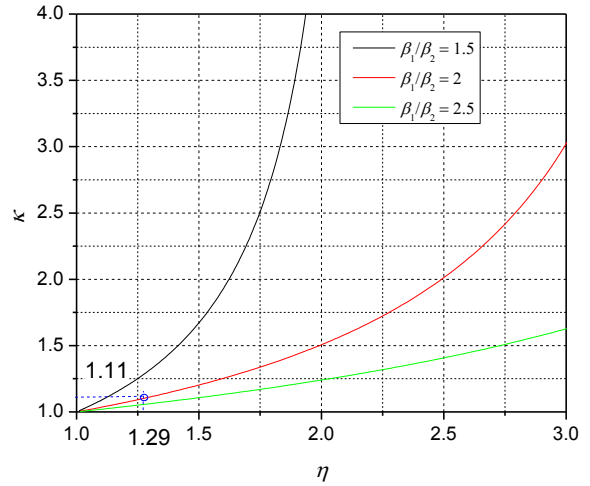
(b) $\beta_2 = 20$
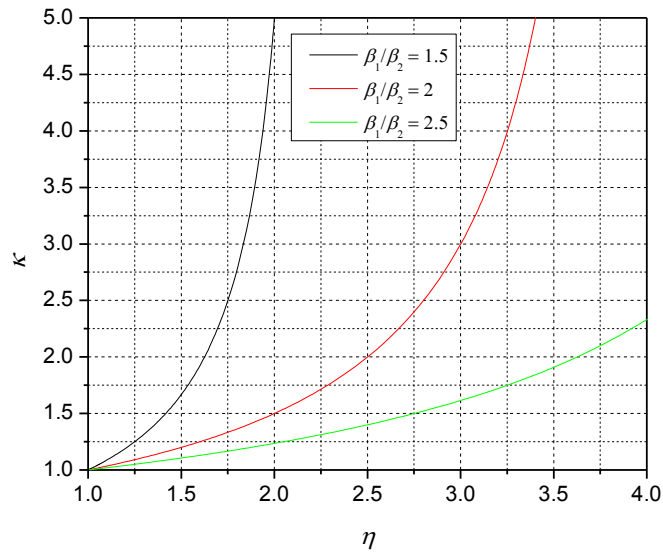
(c) $\beta_2 = 30$

Figure 4.46 Relationships between κ and η for (a) $\beta_2 = 10$, (b) $\beta_2 = 20$, and (c) β_2

$= 30$

101

4.5.3. CTE Measurement

The setup used for CTE measurement is illustrated in Figure 4.47. Two configurations were placed inside a convection oven (EC1A: Sun Systems) and the fibers are connected to the interrogator located outside the oven. The interrogator was connected to a computer for data acquisition.
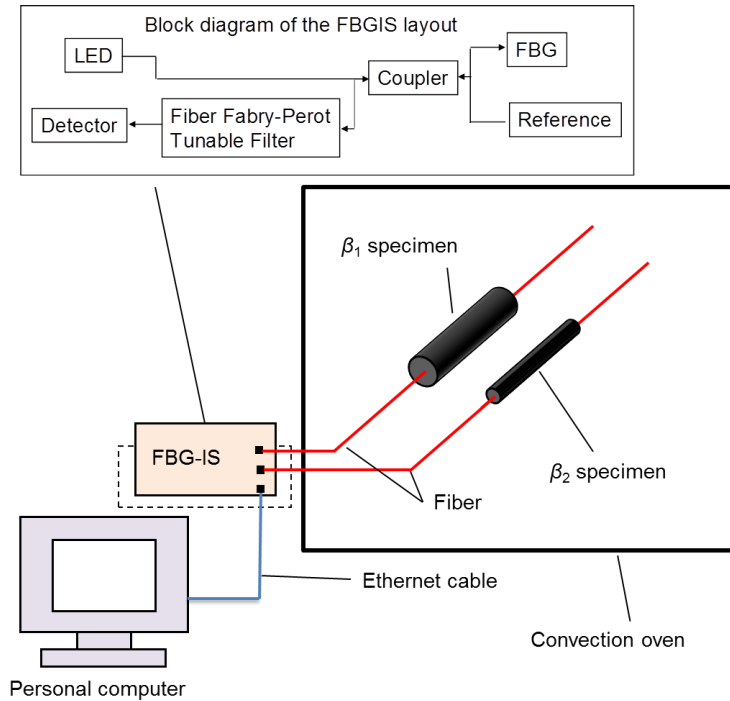
Figure 4.47 Experimental setup for CTE measurement

A block diagram of the fiber Bragg grating interrogation system (FBG-IS) layout is also shown in Figure 4.47. An LED illuminates the FBG, which reflects the light at the Bragg wavelength. The fiber Fabry-Perot tunable filter (FFP-TF) scans the reflected light from the FBG as well as the picoWave reference alternatively. The detected signals are then converted to wavelengths. The picoWave is the multi-wavelength reference of the FBG interrogation system that consists of a Fiber Fabry-Perot Interferometer, a wavelength marker of a fiber Bragg Grating, and a built-in

thermo electric controller for thermal stability. It enables real-time wavelength calibration to picometer accuracy.

Before being embedded into the polymer substrate, two FBGs were calibrated to determine the intrinsic BW shift, $\Delta\lambda_i$. The bare FBG was placed in the environmental chamber subjected to a temperature excursion and the BW shift was documented as a function of temperature. The results of the two fibers are shown in Figure 4.48. The intrinsic BW shift has a quadratic relationship with ΔT [115] and the following relationships were obtained by fitting the results with the quadratic function using the reference temperature of 175 °C:

$$\Delta\lambda_i\big|_{\beta_1} = 0.0103 \cdot (T-175) + 6.78 \times 10^{-6} (T-175)^2 \tag{4.19}$$

$$\Delta\lambda_i\big|_{\beta_2} = 0.0097 \cdot (T-175) + 8.51 \times 10^{-6} (T-175)^2 \tag{4.20}$$
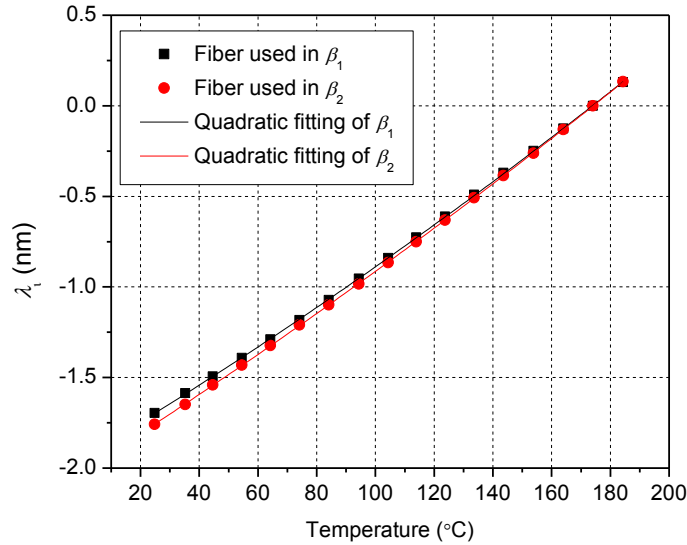
Figure 4.48 Intrinsic BW shifts of FBGs used in two configurations

After the calibration, two fiber/polymer assemblies were fabricated using silicone rubber tubes with two different inner diameters that match to $\beta_1 = 40$ and

$\beta_2 = 20$; the actual dimensions were 5 mm and 2.5 mm, respectively. The fibers were first located at the center of the tubes using an alignment fixture. Then, the polymer was injected into the tubes and cured at a curing temperature. The silicone rubber tubes were removed after the polymer cured. The procedure was presented in the paper [20].

The two assemblies were subjected to the same temperature excursion. The temperature of the specimen was measured by a thermocouple embedded in the specimen. The temperature profiles are shown in Figure 4.49. They show the identical profiles, which confirms that the specimens were at the equilibrium temperatures.
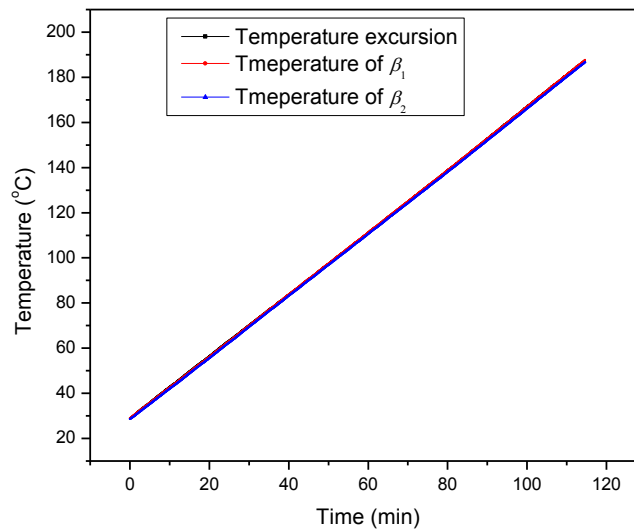
Figure 4.49 Temperatures of two configurations as a function of time

The total BW shift measured by the FBG is shown in Figure 4.50. The stress induced BW shifts were obtained by subtracting the intrinsic BW shift (Figure 4.48) from the total BW shift. The stress induced BW shifts of the two configurations are shown in Figure 4.51.

The BW shifts of the two configurations are superimposed nearly on top of each other at the initial stage of the temperature ramping (below 60 °C). For this region, the

104

parameters η and κ should be "unity" since the modulus of the material is large at low temperatures. As the modulus gradually decreases, the measured BW shift of configuration β_1 starts to deviate from that of configuration β_2. The slope of BW increase is larger in configuration β_1 because of the larger volume stiffness.
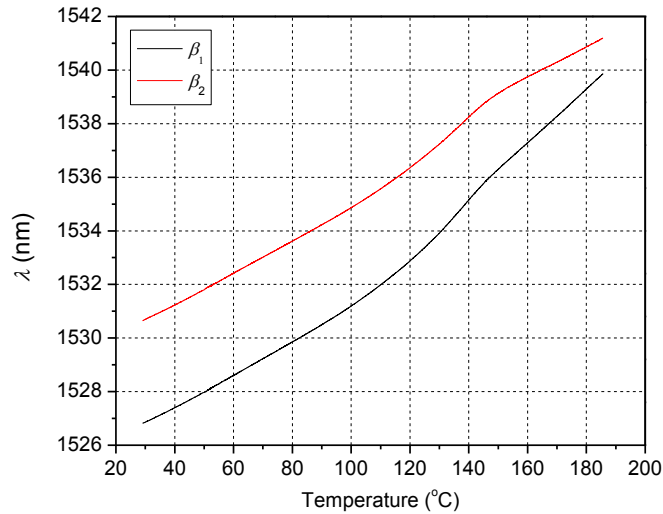
Figure 4.50 Total BW shifts of two specimens
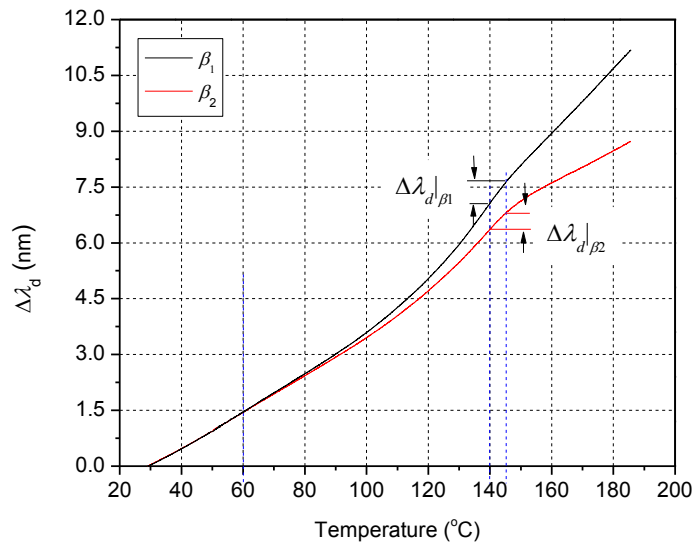
Figure 4.51 Deformation induced BW shifts

The values of η were calculated from the stress induced BW shifts using a constant interval of $\varDelta T = 5$ ℃. An example to calculate the value of η at 140 ℃ is illustrated in Figure 4.51. The BW shift of β_1 caused by increasing the temperature from 140 ℃ to 145 ℃ is $\varDelta \lambda_d\big|_{\beta_1} = 0.557$ nm. The corresponding BW shift of β_2 is $\varDelta \lambda_d\big|_{\beta_2} = 0.43$ nm. Then, the ratio produces the value of η as

$$\eta = \frac{\varDelta \lambda_d\big|_{\beta_1}}{\varDelta \lambda_d\big|_{\beta_2}} = 1.29$$

The value of κ for β_1 and β_2 is determined from Figure 4.46(b); it is 1.11. The complete temperature dependent parameters, η and κ, are plotted in Figure 4.52. Using the value of κ in Figure 4.52 and Eq. (4.14), the BW shifts in the infinite configuration (i.e., $\varDelta \lambda_d\big|_{\beta=\infty}$) were calculated. The final result is shown in Figure 4.53.
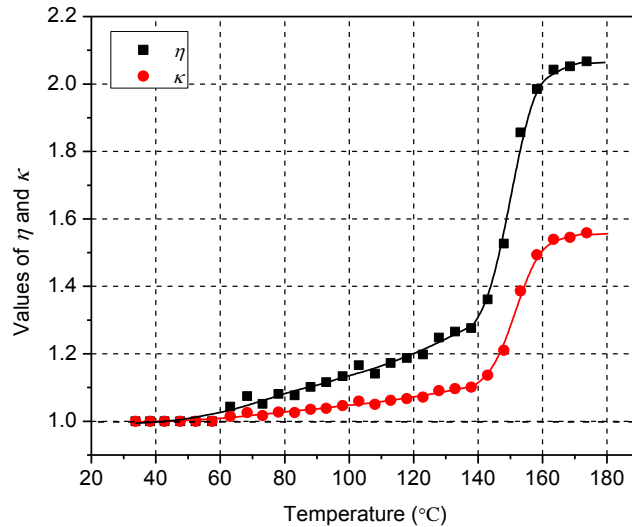
Figure 4.52 Values of η determined from the experimental results; and the corresponding κ values determined from Figure 4.46 (b)
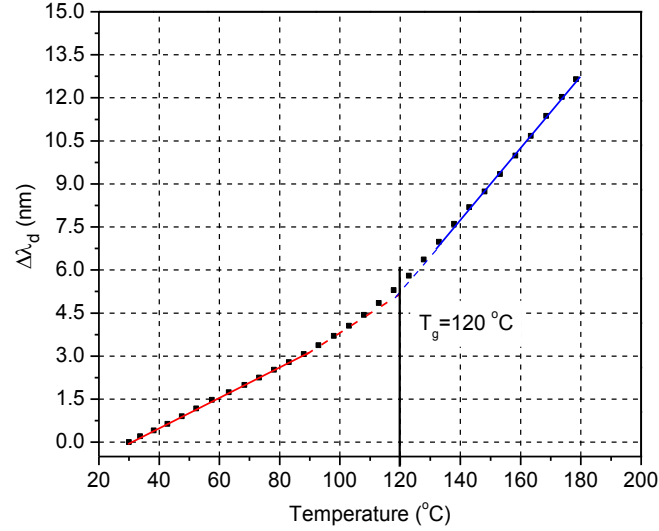
Figure 4.53 BW shift reconstructed for the infinite configuration

The polymer strain caused by thermal expansion can be expressed as

$$\Delta\varepsilon_s(T) = \left(\alpha_s - \alpha_f\right)\Delta T \tag{4.21}$$

where α_s is the CTE of the polymer. Then, from Eq. (3.11) and Eq. (4.21), the CTE of polymer can be calculated as:

$$\alpha_s(T) = \frac{\Delta\varepsilon_s(T)}{\Delta T} + \alpha_f = \frac{\Delta\lambda_d(T)}{\lambda\,(1-P_k)\Delta T} + \alpha_f \tag{4.22}$$

The slopes before and after the glass transition were determined from Figure 4.53; they were 0.0512 nm/°C and 0.128 nm/°C, respectively. Using Eq. (4.22) the CTE are determined to be:

$$\alpha_1 = \frac{0.0512}{1540\cdot(1-0.216)} + 0.55\cdot 10^{-6} = 42.5\cdot 10^{-6}\,/^\circ C$$

$$\alpha_2 = \frac{0.128}{1540\cdot(1-0.216)} + 0.55\cdot 10^{-6} = 106\cdot 10^{-6}\,/^\circ C$$

where the intrinsic properties of the fiber are $\lambda = 1540$ nm and $P_k = 0.216$ [29]. The glass transition temperature can be defined at the inflection point of the BW shift curve and it was determined to be 120 °C.

4.5.4. CHS measurement

The experimental setup for CHS measurement is shown in Figure 4.54. An environment chamber (SH-241: ESPEC) provides the required stable moisture condition, and the moisture weight gain is measured by a high precision balance (PI-225D: Denver Instrument) that offers a resolution of 0.01 mg.

The CHS was measured only at room temperature since it has been known that the CHS of polymer is virtually constant below glass transition temperature [89]. It is important to remember that the modulus of the underfill is very large (6 GPa) at room temperature. As can be seen clearly from Figure 4.50, both configurations mimic the behavior of the infinite configuration below 60 °C; i.e., $\kappa \approx 1$. Consequently, only β_1 configuration was used for CHS measurement.

In the experiment, an extra specimen (the same configuration without the fiber; referred to as a reference specimen) was prepared for moisture weight gain measurement to avoid damaging the fiber during frequent weight measurements. The full spectrum was measured before baking as show in Figure 4.55. Both specimens were then baked at 125 °C for 48 hours until the weight change in the reference specimen was not noticeable. Then, the dry weight was measured (m_{dry} = 308 mg). The BW at the dry condition was also measured at room temperature ($\lambda_d^{dry} = 1538.719$ nm). The full BW spectra of the specimen obtained before and after baking are shown

in Figure 4.55. The BW change during the baking process was $\Delta \text{BW}_{baking} = 1.36$ nm, which was significant and should not be ignored.
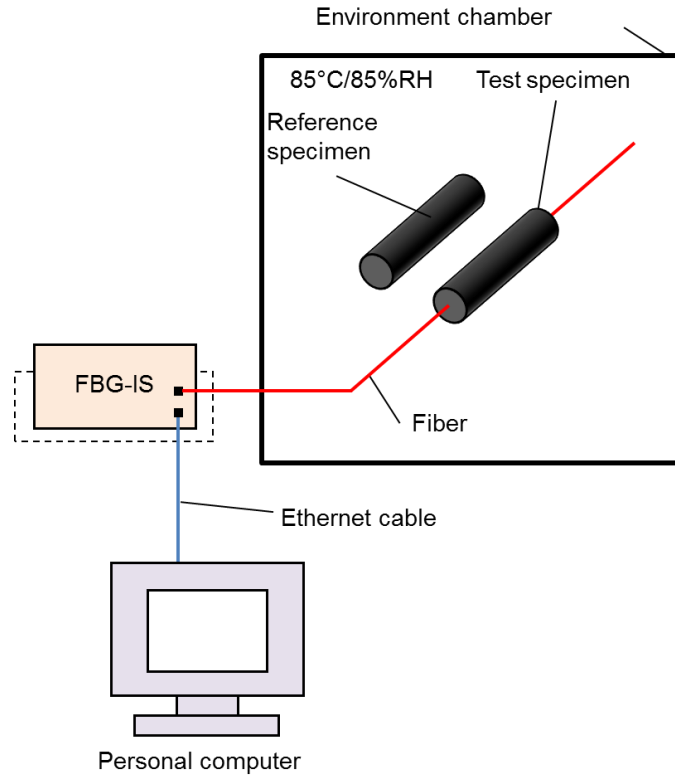
Figure 4.54 Experimental setup for CHS measurement

The reference specimen and the test specimen were placed in the environment chamber (Figure 4.54) and they were subjected to 85 ℃/85%RH. The weight gain of the reference specimen, m_{wet}, was measured periodically. Then, the moisture content (%) was calculated from

$$C = \frac{m_{wet} - m_{dry}}{m_{dry}} \times 100\% \tag{4.23}$$

The complete moisture weight gain history of the reference specimen is shown in Figure 4.56. The specimen was saturated at around 120 hours, and the saturated moisture weight gain was $C_{sat} = 1.07\%$.
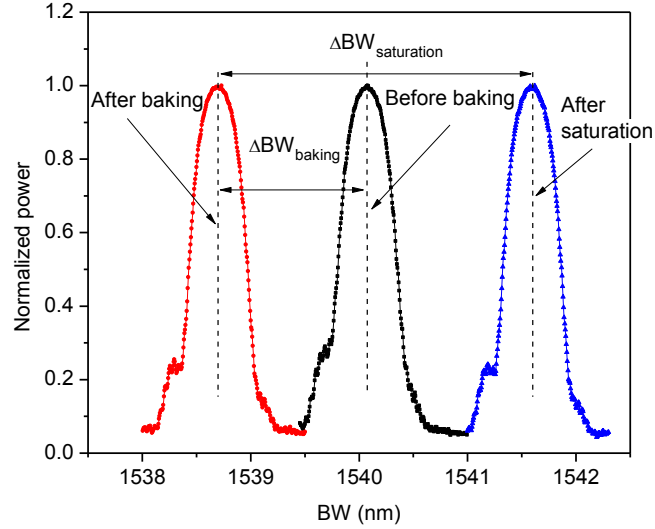
Figure 4.55 Full BW spectrum of the β_1 configuration obtained during the moisture test

The BW was measured after moisture saturation. The full spectrum is also shown in Figure 4.55; $\lambda_d^{sat} = 1541.607$ nm. The net BW change caused by the hygroscopic swelling strain is expressed as

$$\Delta\lambda_d = \lambda_d^{sat} - \lambda_d^{dry} = \lambda(1-P_k)\Delta\varepsilon_s^h \tag{4.24}$$

where λ_d^{sat} is the BW shift at the moisture saturation and $\Delta\varepsilon_s^h$ is the hygroscopic strain of the polymer. Then, the CHS, χ_s, can be determined as

$$\chi_s = \frac{\Delta\varepsilon_s^h}{C} = \frac{\Delta\lambda_d}{\lambda(1-P_k)\cdot C} \tag{4.25}$$

The initial BW after baking is 1538.719 nm. The saturated BW was 1541.607 nm, which yielded the BW increase of 2.888 nm. Using the well-known linear relationship between the hygroscopic swelling strain and the moisture concentration [88, 89, 116-118], the CHS was determined from Eq. (4.25) as

$$\chi_s = \frac{1541.607 - 1538.719}{1540 \cdot (1 - 0.216) \cdot 1.071\%} = 0.223\% \, \varepsilon_h \, / \%C$$
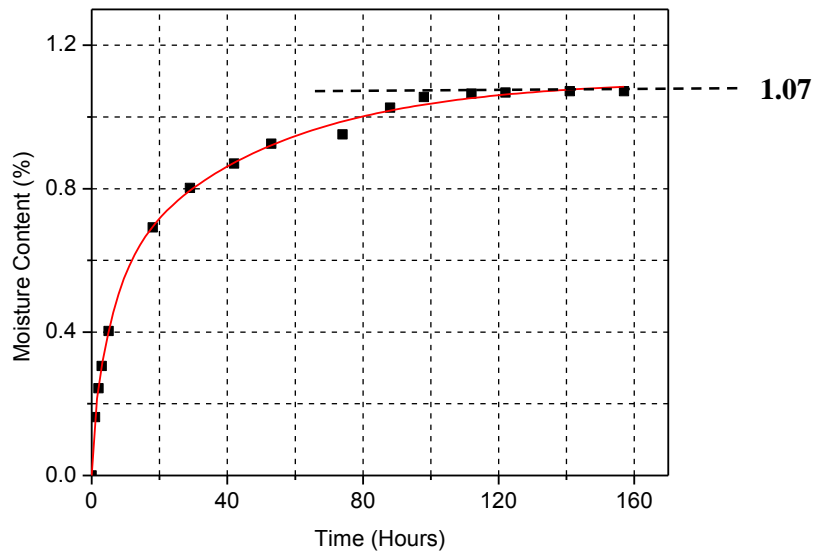
Figure 4.56 Moisture absorption history of the reference specimen

4.5.5. Discussion

The CTE of the tested polymer was also measured by a TMA (TMA-7: Perkin Elmer) for verification. The raw data obtained from TMA for testing is shown in Figure4.57. The CTE values were 41.2 ppm/ °C and 109 ppm/ °C for below and above glass transition temperature, respectively. The glass transition temperature was also determined to be 124 °C. By comparing with the results measured by FBG, the

differences (less than 3%) fall in the typical measurement uncertainty range including the inherent material variability.
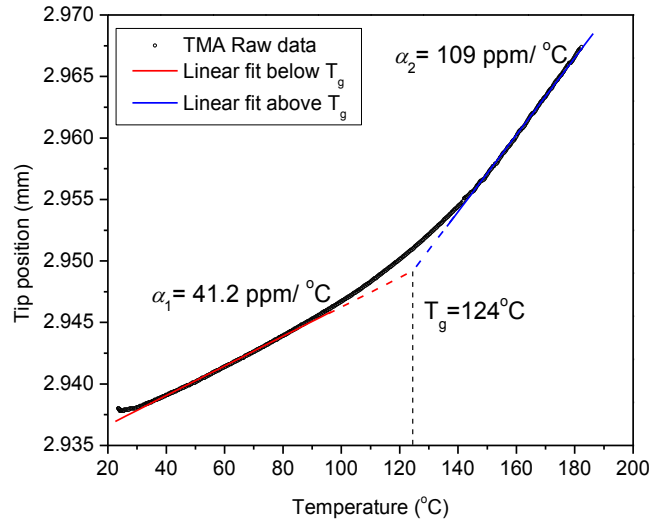
Figure4.57 Measurement of CTE by TMA

In the CHS measurement, the saturated weight gain and the BW change are required for calculation. In order to verify the experimental procedure, the same procedure was repeated with a different configuration, $\beta = 25.4$. The experimental raw data are shown in Figure4.58. The total BW shift was 2.807 nm, which resulted in $\chi_s = 0.22\% \varepsilon_h / \%C$. The difference was within 2% and the results confirmed good repeatability of the measurement.

The CHS value reported in this paper was obtained from the linear relationship between the hygroscopic swelling strain and the moisture concentration. For some epoxy materials, this linear relationship may not be valid [93]. The proposed technique should be practiced with caution when it is utilized to measure the CHS of those materials; an additional moisture weight gain history is needed to determine the moisture concentration-dependent CHS [93].
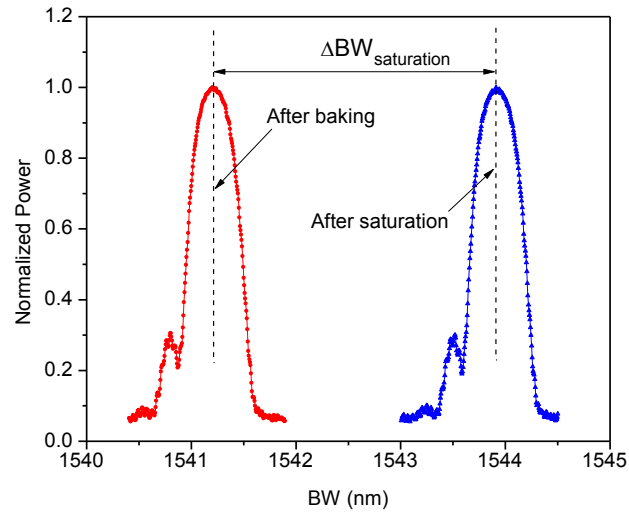
Figure4.58 Full BW spectrum of the smaller configuration ($\beta = 25.4$) obtained during the moisture test

4.5.6. Summary

An experimental technique utilizing the concept of the dual-configuration FBG sensor method was proposed to measure the CTE and CHS of polymeric materials, and it was implemented with a medium filler ratio underfill material. The behavior of the infinite configuration was reconstructed numerically from the two small finite configurations that were subjected to environmental conditions. Then, the CTE and CHS were determined from the simple governing equation that provided a direct relationship between the measured strains and the two coefficients. The small configurations negated the effect of heat generation during curing, which made the method applicable for a wide range of polymeric materials. The measurement accuracy and repeatability were confirmed by a commercial tool and an experiment with a different configuration.

4.6. Summary of the Chapter

The cylindrical specimen with the FBG sensor embedded in the center was used to characterize the comprehensive viscoelastic properties of the polymer. An instantaneous uniaxial compressive loading was applied to the specimen and repeated at different temperatures. The temperature dependent Young's modulus was determined by the initial jump of the Bragg wavelength. And the time temperature Young's modulus was determined by the time dependent BW. The temperature range changes from room to the solder reflow temperature. The time-temperature dependent bulk modulus was determined by applying hydrostatic gas pressure to the specimen. A high pressure system was developed to accommodate the high pressure requirement of the test. The temperature and time dependent bulk modulus was measured at the same temperature range as the Young's modulus. The heat generation issue during the gas compressive was addressed by controlling the free volume in the chamber.

The time-temperature dependent Young's modulus and bulk modulus are shifted and overlapped to create master curve. A single set shift factors were used for both the Young's modulus and bulk modulus. The master curve of the shear modulus was calculated from the bulk modulus and Young's modulus. The mater curve of the bulk modulus and shear modulus are fitted by the prony series and the shift factors are fitted by the piece-wise shift functions. The coefficients of the prony series and the shift functions are used as material inputs in FEM to predict the behavior of the material at different temperatures.

The assumptions associated with the linear viscoelasticity were verified by supplementary experiments. Three assumptions were investigated:

Thermorheologically simple (TRS); Boltzmann superposition principle (BPS); linear viscoelasticity. The TRS assumption was verified by superposing the long term and short term time dependent data at different temperatures. The BPS assumption was verified by applying step loading and the measured behavior to the predicted results. The linear viscoelasticity was verified by comparing the time dependent Young's modulus at different stress levels.

The measured properties were verified by independent experiments. A three point bending test was conducted to verify the temperature dependent Young's modulus. The Shadow moire and Twyman/Green were used to verity the measured viscoelastic properties of the material.

The temperature dependent CTE is determined by creating the infinite configuration from the two small configurations of the specimen. The CHS is measured by a single configuration. The measured properties are verified by the TMA and another independent experiment.

Chapter 5 Contributions and Future Work

5.1. Thesis Contributions

The thermo-mechanical properties of the polymeric materials for the warpage and residual stress prediction in microelectronics packaging were characterized by the FBG based technologies. The most significant contributions made in this dissertation are:

a) A novel setup was developed to characterize the curing properties of the silicone elastomer material. To the best knowledge of the author, the silicone curing properties are not available in the literature. This technique will enable the packaging design engineer to quickly evaluate the curing induced residual stress in the potted components.

b) A two-step curing procedure was proposed to improve the existing technique for underfill curing properties measurement. The procedure ensures the free curing of the underfill after the gelation point. The measured curing properties can be used for the evaluation of the residual stress in the flip chip layer of the package.

c) An effective system to characterize the curing properties of the EMC material was developed. The system accommodates the high temperature and high pressure curing condition of the EMC. The measured effective chemical shrinkage of the EMC can be utilized for the warpage evaluation of the various molded packages.

d) The comprehensive viscoelastic properties of the EMC material were determined by the single configuration. The time-temperature dependent Young's modulus was determined by the compressive creep test. The time-temperature

dependent bulk modulus was measured by hydrostatic gas pressure. The gas pressure was used by taking advantage of the high sensitivity of the FBG sensor. The piece-wise shift function were proposed and implemented in the FEM using user-defined subroutine.

e) The assumptions associated with the linear viscoelasticity were investigated by experiments. The experiments proved that assumptions are valid for the EMC material. The proposed experiments provide an effective way to verify the validity of the assumption for certain materials.

f) A bi-material specimen was created and subjected to various thermal loading to verify the measured viscoelastic properties. The temperature rate dependent warpage was measured by Twyman/Green, which shows clear viscoelastic behavior of the material

g) The infinite configuration was numerically constructed to determine the temperature dependent CTE and CHS of the polymer material.

h) The single configuration is proposed to measure the thermos-mechanical properties including: curing shrinkage, viscoelasticity and the temperature dependent CTE. The technique provides an effective and efficient way to characterize the properties for the warpage and residual stress prediction.

5.2. Future Work

The cylindrical specimen with the FBG sensor embedded in the center can be used for the characterization of other properties:

a) Curing dependent viscoelasticity

In order to determine the warpage and residual stress evolution during curing of the polymeric materials, the curing dependent viscoelasticity should be measured accurately. The cylindrical specimen with the polymer cured to certain extent can be made. And the conversion dependent viscoelasticity can be measured by the partially cured specimen. The challenge is to control the curing extent accurately and maintain the curing extent during the viscoelastic properties characterization.

b) Thermal conductivity and specific heat

The sensor embedded in the specimen can also be used as a temperature sensor. By applying temperature loading to the specimen and the monitoring the temperature change in the center of the specimen, the thermal conductivity can be estimated. The challenge is to control the boundary condition accurately so that the model can mimic the experiment to determine the thermal properties.

c) Properties degradations

The cured specimen can be subjected to various thermal and moisture conditions of the accelerated test. The sensor embedded in the center of the specimen can monitor the strain change. The properties degradations can be determined from the specimen.

Appendix I: Analytical solution

The stress distribution in the fiber and polymer can be expressed as:

$$\sigma_{rr}(r) = \frac{E_f}{1+\nu_f}\left[\frac{C_{1f}}{1-2\nu_f} - \frac{C_{2f}}{r^2}\right] + \frac{E_f\nu_f c}{(1+\nu_f)(1-2\nu_f)}, \quad 0 \le r \le r_f$$

$$\sigma_{\theta\theta}(r) = \frac{E_f}{1+\nu_f}\left[\frac{C_{1f}}{1-2\nu_f} + \frac{C_{2f}}{r^2}\right] + \frac{E_f\nu_f c}{(1+\nu_f)(1-2\nu_f)}, \quad 0 \le r < r_f$$

$$\sigma_{zz}(r) = \frac{2E_f}{1+\nu_f}\frac{C_{1f}}{1-2\nu_f} + \frac{2E_f\nu_f^2 c}{(1+\nu_f)(1-2\nu_f)} + E_f c, 0 \le r < r_f$$

$$u(r) = C_{1f}r + \frac{C_{2f}}{r}, \quad 0 \le r \le r_f$$

$$\sigma_{rr}(r) = \frac{E_p}{1+\nu_p}\left[\frac{C_{1p}}{1-2\nu_p} - \frac{C_{2p}}{r^2}\right] + \frac{E_p\nu_p c}{(1+\nu_p)(1-2\nu_p)}, \quad r_f \le r \le r_p$$

$$\sigma_{\theta\theta}(r) = \frac{E_p}{1+\nu_p}\left[\frac{C_{1p}}{1-2\nu_p} + \frac{C_{2p}}{r^2}\right] + \frac{E_p\nu_p c}{(1+\nu_p)(1-2\nu_p)}, \quad r_f < r \le r_p$$

$$\sigma_{zz}(r) = \frac{2E_p}{1+\nu_p}\frac{C_{1p}}{1-2\nu_p} + \frac{2E_p\nu_p^2 c}{(1+\nu_p)(1-2\nu_p)} + E_p c, \quad r_f \le r \le r_p$$

$$u(r) = C_{1p}r + \frac{C_{2p}}{r}, \quad r_f \le r \le r_p$$

(A.1)

where σ_{zz}, σ_{rr} and $\sigma_{\theta\theta}$ are the axial, radial and hoop stress components, respectively; E, ν and r are the modulus, Poisson's ratio and radius, where the subscripts, f and p, denote the fiber and polymer; $u(r)$ is the radial displacement; the coefficients C_{1p}, C_{2p}, C_{1f}, C_{2f} and c are the unknown constants that can be determined from the boundary conditions.

Applying the following boundary conditions:

$$u(0) = 0$$

$$u_f(r_f) = u_p(r_f)$$

$$\sigma_{rr}^p(r_p) = P_2 \qquad\qquad (A.2)$$

$$\sigma_{rr}^p(r_f) = \sigma_{rr}^f(r_f)$$

$$\frac{\int_0^b 2\sigma_{zz}(r)\,r\,dr}{r_p^{\,2}} = P_1$$

The coefficients in Eq. (A.1) can be calculated as:

$$C_{1p} = \frac{CE - BF}{AE - BD}$$

$$c = \frac{CD - AF}{BD - AE}$$

$$C_{2p} = \left(\frac{C_{1p}}{(1-2\nu_p)(1+\nu_p)} + \frac{\nu_p C_0}{(1-2\nu_p)(1+\nu_p)} - \frac{P_1}{E_p} \right)(1+\nu_p)\,r_p^{\,2} \qquad (A.3)$$

$$C_{1f} = C_{1p} + \frac{C_{2p}}{r_p^{\,2}}$$

$$C_{2f} = 0$$

where

$$A = \frac{E_p}{(1+\nu_p)(1-2\nu_p)}\left(\frac{r_p^{\,2}}{r_f^{\,2}} - 1\right) + \frac{E_f}{(1+\nu_f)(1-2\nu_f)}\left(1 + \frac{r_p^{\,2}}{r_p^{\,2}(1-2\nu_p)}\right)$$

$$B = \frac{E_p \nu_p}{(1+\nu_p)(1-2\nu_p)}\left(\frac{r_p^{\,2}}{r_f^{\,2}} - 1\right) + \frac{E_f \nu_f}{(1+\nu_f)(1-2\nu_f)}\left(1 + \frac{r_p^{\,2}}{r_f^{\,2}(1-2\nu_p)}\frac{\nu_p}{\nu_f}\right)$$

$$C = \left(1 + \frac{E_f}{(1+\nu_f)(1-2\nu_f)}\frac{(1+\nu_p)}{E_p}\right)\frac{r_p^{\,2}}{r_f^{\,2}}P_2$$

$$D = \frac{2E_p \nu_p}{(1+\nu_p)(1-2\nu_p)}\left(\frac{r_p^{\,2}}{r_f^{\,2}} - 1\right) + \frac{2E_f \nu_f}{(1+\nu_f)(1-2\nu_f)}\left(1 + \frac{r_p^{\,2}}{r_f^{\,2}(1-2\nu_p)}\right)$$

$$E = \frac{2E_p \nu_p^{\,2}}{(1+\nu_p)(1-2\nu_p)}\left(\frac{r_p^{\,2}}{r_f^{\,2}} - 1\right) + \frac{2E_f \nu_f}{(1+\nu_f)(1-2\nu_f)}\left(\nu_f + \frac{\nu_p r_p^{\,2}}{r_f^{\,2}(1-2\nu_p)}\right) + E_f + E_p\left(\frac{r_p^{\,2}}{r_f^{\,2}} - 1\right)$$

$$F = \frac{2E_f \nu_f}{(1+\nu_f)(1-2\nu_f)E_p}(1+\nu_p)\frac{r_p^{\,2}}{r_p^{\,2}}P_2 + \frac{r_p^{\,2}}{r_f^{\,2}}P_1$$

(A.4)

Appendix II

Young's modulus calculation

```
%unit: mm-N-MPa-s
clc
clear all

P1=;
P2=0;
Delta_BW=;
options = optimset('TolFun',1e-20,'TolX', 1e20, 'MaxFunEvals',
100000, 'Display', 'on', 'MaxIter', 10000);
E=fsolve(@(x) E_cal(P1,0,delta_BW,x),1e6,options)

Function y=E_cal(P1,P2,delta_BW, E)
```

Bulk modulus calculation

```
%unit: mm-N-MPa-s
clc
clear all

P1=;
P2=;
delta_BW=;
E=;
options = optimset('TolFun',1e-20,'TolX', 1e20, 'MaxFunEvals',
100000, 'Display', 'on', 'MaxIter', 10000);
K=fsolve(@(x) K_cal(P1,P2,delta_BW,E,x),1e6,options)

Function y=K_cal(P1,P2,delta_BW, E, K)

----------------------------------------------------
a=0.125;  % fiber diameter
b=8.8;    % EMC diameter
beta=b/a; % Configuration
E_f=73000; % Fiber modulus
v_f=0.17;  % Fiber Poisson's ratio
P_11=0.121; % Optical constant
P_12=0.27;  % Optical constant
n=1.457;    % Optical constant
BW0=1550;   % Initial BW
E_p=E;      % Young's modulus of EMC
v_p=0.3;
A=E_p/(1+v_p)/(1-2*v_p)*(beta^2-1)+E_f/(1+v_f)/(1-
2*v_f)*(1+beta^2/(1-2*v_p));
B=E_p*v_p/(1+v_p)/(1-2*v_p)*(beta^2-1)+E_f*v_f/(1+v_f)/(1-
2*v_f)*(1+beta^2/(1-2*v_p)*v_s/v_f);
C=(1+E_f/(1+v_f)/(1-2*v_f)*(1+v_p)/E_p)*beta^2*P2;
D=2*E_p*v_p/(1+v_p)/(1-2*v_p)*(beta^2-1)+2*v_f*E_f/(1+v_f)/(1-
2*v_f)*(1+beta^2/(1-2*v_p));
```

```
E=2*E_p*v_p^2/(1+v_p)/(1-2*v_p)*(beta^2-1)+2*v_f*E_f/(1+v_f)/(1-
2*v_f)*(v_f+beta^2*v_p/(1-2*v_p))+E_f+E_p*(beta^2-1);
F=2*E_f*v_f/(1+v_f)/(1-2*v_f)/E_p*(1+v_p)*beta^2*P2+b^2/a^2*P1;
C_1s=(C*E-B*F)/(A*E-B*D);
C_0=(C*D-A*F)/(B*D-A*E);
C_2s=(C_1s/(1-2*v_p)+C_0*v_p/(1-2*v_p)-P1/E_p*(1+v_p))*b^2;
C_1f=C_1s+C_2s/a^2;
strain_z=C_0;
strain_r=C_1f;
stress_f_r=E_f*C_1f/(1+v_f)/(1-2*v_f)+E_f*v_f*C_0/(1+v_f)/(1-2*v_f);
stress_s_r_a=E_p*C_1s/(1+v_p)/(1-2*v_p)-
E_s*C_2s/a^2/(1+v_p)+E_p*v_p*C_0/(1+v_p)/(1-2*v_p);
stress_f_z=2*v_f*E_f*C_1f/(1+v_f)/(1-
2*v_f)+2*v_f^2*E_f*C_0/(1+v_f)/(1-2*v_f)+E_f*C_0;
stress_s_z=2*v_p*E_p*C_1s/(1+v_p)/(1-
2*v_p)+2*v_p^2*E_p*C_0/(1+v_p)/(1-2*v_p)+E_p*C_0;
F_z=stress_f_z*a^2+stress_s_z*(b^2-a^2)-P2*b^2;
stress_s_r=E_p*C_1s/(1+v_p)/(1-2*v_p)-
E_p*C_2s/a^2/(1+v_p)+E_p*v_p*C_0/(1+v_p)/(1-2*v_p);
delta_BW=1/E_f*((1-n^2/2*(P_12-(P_11+P_12)*v_f))*stress_f_z-
(2*v_f+n^2/2*((1-v_f)*P_11+(1-3*v_f)*P_12))*stress_f_r)*BW0;  % BW
change
```

Reference

[1]   K. Oota and M. Saka, "Cure shrinkage analysis of epoxy molding compound," *Polymer Engineering & Science,* vol. 41, pp. 1373-1379, 2001.

[2]   "Impact of Green Mold Compounds on First-and Second-Level Interconnect Reliability," 2013.

[3]   G. Kelly, C. Lyden, W. Lawton, J. Barrett, A. Saboui, H. Pape, and H. J. Peters, "Importance of molding compound chemical shrinkage in the stress and warpage analysis of PQFPs," *Components, Packaging, and Manufacturing Technology, Part B: Advanced Packaging, IEEE Transactions on,* vol. 19, pp. 296-300, 1996.

[4]   T. Y. Tee and Z. Zhong, "Integrated vapor pressure, hygroswelling, and thermo-mechanical stress modeling of QFN package during reflow with interfacial fracture mechanics analysis," *Microelectronics Reliability,* vol. 44, pp. 105-114, 2004.

[5]   J. W. Kong, J.-K. Kim, and M. M. Yuen, "Warpage in plastic packages: effects of process conditions, geometry and materials," *Electronics Packaging Manufacturing, IEEE Transactions on,* vol. 26, pp. 245-252, 2003.

[6]   K. Mahan, Y. Sun, B. Han, S. Han, and M. Osterman, "Adhesion and Puncture Strength of Polyurethane Coating Used to Mitigate Tin Whisker Growth," *Journal of electronic packaging,* vol. 136, p. 031004, 2014.

[7]   M.-Y. Tsai, Y.-C. Chen, and S. R. Lee, "Correlation between measurement and simulation of thermal warpage in PBGA with consideration of molding compound residual strain," *Components and Packaging Technologies, IEEE Transactions on,* vol. 31, pp. 683-690, 2008.

[8]   L. Li, K. Hubbard, and J. Xue, "Improving board assembly yield through PBGA warpage reduction," in *Electronic Packaging Technology & High Density Packaging, 2009. ICEPT-HDP'09. International Conference on*, 2009, pp. 949-953.

[9]   J. Kim, S. Lee, J. Lee, S. Jung, and C. Ryu, "Warpage Issues and Assembly Challenges Using Coreless Package Substrate."

[10]   N. Vijayaragavan, F. Carson, and A. Mistry, "Package on Package warpage-impact on surface mount yields and board level reliability," in *Electronic Components and Technology Conference, 2008. ECTC 2008. 58th*, 2008, pp. 389-396.

[11]   P. Sun, V. C.-K. Leung, B. Xie, V. W. Ma, and D. X.-Q. Shi, "Warpage reduction of package-on-package (PoP) module by material selection & process

optimization," in *Electronic Packaging Technology & High Density Packaging, 2008. ICEPT-HDP 2008. International Conference on*, 2008, pp. 1-6.

[12] Y. L. Tzeng, N. Kao, E. Chen, J. Y. Lai, Y. P. Wang, and C. Hsiao, "Warpage and stress characteristic analyses on package-on-package (POP) structure," in *Electronics Packaging Technology Conference, 2007. EPTC 2007. 9th*, 2007, pp. 482-487.

[13] G. Caswell, "Challenges With Package on Package (PoP) Technology," 2012.

[14] L.-C. Hong and S.-J. Hwang, "Study of warpage due to PVTC relation of EMC in IC packaging," *Components and Packaging Technologies, IEEE Transactions on,* vol. 27, pp. 291-295, 2004.

[15] W. Zhu, G. Li, W. Sun, F. Che, A. Sun, C. Wang, H. Tan, B. Zhao, and N. Chin, "Cure shrinkage characterization and its implementation into correlation of warpage between simulation and measurement," in *Thermal, Mechanical and Multi-Physics Simulation Experiments in Microelectronics and Micro-Systems, 2007. EuroSime 2007. International Conference on*, 2007, pp. 1-8.

[16] G. Hu, J.-E. Luan, and S. Chew, "Characterization of chemical cure shrinkage of epoxy molding compound with application to warpage analysis," *Journal of electronic packaging,* vol. 131, p. 011010, 2009.

[17] J. De Vreugd, K. M. Jansen, L. J. Ernst, and C. Bohm, "Prediction of cure induced warpage of micro-electronic products," *Microelectronics Reliability,* vol. 50, pp. 910-916, 2010.

[18] K. M. Jansen, C. Qian, L. J. Ernst, C. Bohm, A. Kessler, H. Preu, and M. Stecher, "Modeling and characterization of molding compound properties during cure," *Microelectronics Reliability,* vol. 49, pp. 872-876, 2009.

[19] M. Amagai and Y. Suzuki, "A study of package warpage for package on package (PoP)," in *Electronic Components and Technology Conference (ECTC), 2010 Proceedings 60th*, 2010, pp. 226-233.

[20] Y. Wang, L. Woodworth, and B. Han, "Simultaneous measurement of effective chemical shrinkage and modulus evolutions during polymerization," *Experimental mechanics,* vol. 51, pp. 1155-1169, 2011.

[21] Y. Sun, Y. Wang, C. Jang, B. Han, and K. Choi, "Generalized Hybrid Modeling to Determine Chemical Shrinkage and Modulus Evolutions at Arbitrary Temperatures," *Experimental mechanics,* pp. 1-8, 2013.

[22] N. Srikanth, "Warpage analysis of epoxy molded packages using viscoelastic based model," *Journal of materials science,* vol. 41, pp. 3773-3780, 2006.

[23] S. G. Croll, "Residual stress in a solventless amine-cured epoxy coating," *Journal of Coatings Technology,* vol. 51, pp. 49-55, 1979.

[24] M. Lai, K. Friedrich, J. Botsis, and T. Burkhart, "Evaluation of residual strains in epoxy with different nano/micro-fillers using embedded fiber Bragg grating sensor," *Composites Science and Technology,* vol. 70, pp. 2168-2175, 2010.

[25] S. Shh, M. Krguller, and M. Sarigaphuti, "Effects of shrinkage-reducing admixtures on restrained shrinkage cracking of concrete," *ACI Materials Journal,* vol. 89, 1992.

[26] M. H. Meuwissen, H. A. de Boer, H. L. Steijvers, P. J. Schreurs, and M. G. Geers, "Residual stresses in microelectronics induced by thermoset packaging materials during cure," *Microelectronics Reliability,* vol. 44, pp. 1985-1994, 2004.

[27] C. Ober and G. Barclay, "Liquid Crystalline Thermosets As Materials For Microelectronics," in *MRS Proceedings*, 1991, p. 281.

[28] A. F. Lewis, "Dynamic mechanical behavior during the thermosetting curing process," *Polymer Engineering & Science,* vol. 3, pp. 201-209, 1963.

[29] Y. Wang, B. Han, D. Kim, A. Bar-Cohen, and P. Joseph, "Integrated measurement technique for curing process-dependent mechanical properties of polymeric materials using fiber bragg grating," *Experimental mechanics,* vol. 48, pp. 107-117, 2008.

[30] A. Spoelstra, G. Peters, and H. Meijer, "Chemorheology of a highly filled epoxy compound," *Polymer Engineering & Science,* vol. 36, pp. 2153-2162, 1996.

[31] K. I. Y. Chien, J. Zhang, L. Rector, and M. Todd, "Low Warpage Molding Compound Development for Array Packages," in *Electronics Systemintegration Technology Conference, 2006. 1st*, 2006, pp. 1001-1006.

[32] S.-S. Deng, S.-J. Hwang, and H.-H. Lee, "Warpage Prediction and Experiments of Fan-Out Waferlevel Package During Encapsulation Process," 2013.

[33] H. Ishida and H. Y. Low, "A study on the volumetric expansion of benzoxazine-based phenolic resin," *Macromolecules,* vol. 30, pp. 1099-1106, 1997.

[34] S. J. Hwang and Y. S. Chang, "Isobaric cure shrinkage behaviors of epoxy molding compound in isothermal state," *Journal of Polymer Science Part B: Polymer Physics,* vol. 43, pp. 2392-2398, 2005.

[35] V. Fano, I. Ortalli, S. Pizzi, and M. Bonanini, "Polymerization shrinkage of microfilled composites determined by laser beam scanning," *Biomaterials,* vol. 18, pp. 467-470, 1997.

[36] A. W. Snow and J. P. Armistead, "A simple dilatometer for thermoset cure shrinkage and thermal expansion measurements," *Journal of applied polymer science,* vol. 52, pp. 401-411, 1994.

[37] W. Cook, M. Forrest, and A. Goodwin, "A simple method for the measurement of polymerization shrinkage in dental composites," *Dental Materials,* vol. 15, pp. 447-449, 1999.

[38] C. L. Thomas and A. J. Bur, "In-situ monitoring of product shrinkage during injection molding using an optical sensor," *Polymer Engineering & Science,* vol. 39, pp. 1619-1627, 1999.

[39] A. Hudson, S. Martin, M. Hubert, and J. Spelt, "Optical measurements of shrinkage in UV-cured adhesives," *Journal of electronic packaging,* vol. 124, pp. 352-354, 2002.

[40] H. Yu, S. Mhaisalkar, and E. Wong, "Cure shrinkage measurement of nonconductive adhesives by means of a thermomechanical analyzer," *Journal of electronic materials,* vol. 34, pp. 1177-1182, 2005.

[41] D. Karalekas, I. M. Daniel, J. T. Gotro, and T.-M. Wang, "Determination of chemical cure shrinkage in composite laminates," *Journal of Composites, Technology and Research,* vol. 12, pp. 172-176, 1990.

[42] A. A. Stolov, T. Xie, J. Penelle, and S. L. Hsu, "Simultaneous measurement of polymerization kinetics and stress development in radiation-cured coatings: A new experimental approach and relationship between the degree of conversion and stress," *Macromolecules,* vol. 33, pp. 6970-6976, 2000.

[43] K. Jansen, J. de Vreugd, and L. Ernst, "Analytical estimate for cure-induced stresses and warpage in flat packages," in *Thermal, Mechanical and Multi-Physics Simulation and Experiments in Microelectronics and Microsystems (EuroSimE), 2011 12th International Conference on*, 2011, pp. 1/4-4/4.

[44] G. Hu, S. Chew, and J.-E. Luan, "Characterization of chemical cure shrinkage of epoxy molding compound with application to warpage analysis," *Journal of electronic packaging,* vol. 131, p. 011010, 2009.

[45] C. Li, K. Potter, M. R. Wisnom, and G. Stringer, "In-situ measurement of chemical shrinkage of MY750 epoxy resin by a novel gravimetric method," *Composites Science and Technology,* vol. 64, pp. 55-64, 2004.

[46] J. Lange, S. Toll, J.-A. E. Månson, and A. Hult, "Residual stress build-up in thermoset films cured above their ultimate glass transition temperature," *Polymer,* vol. 36, pp. 3135-3141, 1995.

[47]   K. Kim and H. Hahn, "Residual stress development during processing of graphite/epoxy composites," *Composites Science and Technology,* vol. 36, pp. 121-132, 1989.

[48]   T. Curiel and G. Fernlund, "Deformation and stress build-up in bi-material beam specimens with a curing FM300 adhesive interlayer," *Composites part A: applied science and manufacturing,* vol. 39, pp. 252-261, 2008.

[49]   K. Jansen, L. Wang, D. Yang, C. van't Hof, L. Ernst, H. Bressers, and G. Zhang, "Constitutive modeling of moulding compounds [electronic packaging applications]," in *Electronic Components and Technology Conference, 2004. Proceedings. 54th*, 2004, pp. 890-894.

[50]   C. T. McKee, J. A. Last, P. Russell, and C. J. Murphy, "Indentation versus tensile measurements of Young's modulus for soft biological tissues," *Tissue Engineering Part B: Reviews,* vol. 17, pp. 155-164, 2011.

[51]   S. L. Simon, G. B. Mckenna, and O. Sindt, "Modeling the evolution of the dynamic mechanical properties of a commercial epoxy during cure after gelation," *Journal of applied polymer science,* vol. 76, pp. 495-508, 2000.

[52]   M. Zarrelli, I. K. Partridge, and A. D'Amore, "Warpage induced in bi-material specimens: Coefficient of thermal expansion, chemical shrinkage and viscoelastic modulus evolution during cure," *Composites part A: applied science and manufacturing,* vol. 37, pp. 565-570, 2006.

[53]   Y. K. Kim and S. R. White, "Stress relaxation behavior of 3501-6 epoxy resin during cure," *Polymer Engineering & Science,* vol. 36, pp. 2852-2862, 1996.

[54]   Y.-J. Lin, S.-J. Hwang, H.-H. Lee, and D.-Y. Huang, "Modeling of viscoelastic behavior of an epoxy molding compound during and after curing," *Components, Packaging and Manufacturing Technology, IEEE Transactions on,* vol. 1, pp. 1755-1760, 2011.

[55]   I. Emri, "Rheology of solid polymers," *Rheology Reviews,* vol. 2005, p. 49, 2005.

[56]   L. Brinson and W. Knauss, "Thermorheologically complex behavior of multi-phase viscoelastic materials," *Journal of the Mechanics and Physics of Solids,* vol. 39, pp. 859-880, 1991.

[57]   N. K. Dutta, N. R. Choudhury, J. Matisons, and G. Edward, "Prediction of viscoelastic behaviour of thermorheologically complex polymeric materials," *Journal of reinforced plastics and composites,* vol. 20, pp. 399-408, 2001.

[58]   D. Fesko and N. Tschoegl, "Time-temperature superposition in thermorheologically complex materials," in *Journal of Polymer Science Part C: Polymer Symposia*, 1971, pp. 51-69.

[59] B. Harper and Y. Weitsman, "Characterization method for a class of thermorheologically complex materials," *Journal of Rheology (1978-present),* vol. 29, pp. 49-66, 1985.

[60] E. Klompen and L. E. Govaert, "Nonlinear viscoelastic behaviour of thermorheologically complex materials," *Mechanics of Time-Dependent Materials,* vol. 3, pp. 49-69, 1999.

[61] S. Jazouli, W. Luo, F. Brémand, and T. Vu-Khanh, "Nonlinear creep behavior of viscoelastic polycarbonate," *Journal of materials science,* vol. 41, pp. 531-536, 2006.

[62] A. Amirkhizi, J. Isaacs, J. McGee, and S. Nemat-Nasser, "An experimentally-based viscoelastic constitutive model for polyurea, including pressure and temperature effects," *Philosophical magazine,* vol. 86, pp. 5847-5866, 2006.

[63] L. Ernst, G. Zhang, K. Jansen, and H. Bressers, "Time-and temperature-dependent thermo-mechanical modeling of a packaging molding compound and its effect on packaging process stresses," *Journal of electronic packaging,* vol. 125, pp. 539-548, 2003.

[64] D.-L. Chen, P.-F. Yang, and Y.-S. Lai, "A review of three-dimensional viscoelastic models with an application to viscoelasticity characterization using nanoindentation," *Microelectronics Reliability,* vol. 52, pp. 541-558, 2012.

[65] H. F. Brinson and L. C. Brinson, *Polymer engineering science and viscoelasticity*: Springer, 2008.

[66] J. de Vreugd, K. Jansen, A. Xiao, L. Ernst, C. Bohm, A. Kessler, H. Preu, and M. Stecher, "Advanced viscoelastic material model for predicting warpage of a QFN panel," in *Electronic Components and Technology Conference, 2008. ECTC 2008. 58th*, 2008, pp. 1635-1640.

[67] S.-H. Chae, J.-H. Zhao, D. R. Edwards, and P. S. Ho, "Characterization of Viscoelasticity of Molding Compounds in Time Domain," in *ASME 2009 InterPACK Conference collocated with the ASME 2009 Summer Heat Transfer Conference and the ASME 2009 3rd International Conference on Energy Sustainability*, 2009, pp. 435-441.

[68] J. Liang, R. Li, and S. Tjong, "Effects of glass bead size and content on the viscoelasticity of filled polypropylene composites," *Polymer testing,* vol. 19, pp. 213-220, 2000.

[69] R. Hagen, L. Salmén, H. Lavebratt, and B. Stenberg, "Comparison of dynamic mechanical measurements and T g determinations with two different instruments," *Polymer testing,* vol. 13, pp. 113-128, 1994.

[70]   R. Maksimov and É. Plume, "Predicting the creep of unidirectional reinforced plastic with thermorheologically simple structural components," *Mechanics of Composite Materials,* vol. 18, pp. 737-744, 1983.

[71]   A. Sarhadi, J. H. Hattel, and H. N. Hansen, "Precision Glass Molding: Validation of an FE Model for Thermo-Mechanical Simulation," *International Journal of Applied Glass Science,* vol. 5, pp. 297-312, 2014.

[72]   D. J. O'Brien, N. Sottos, and S. R. White, "Cure-dependent viscoelastic Poisson's ratio of epoxy," *Experimental mechanics,* vol. 47, pp. 237-249, 2007.

[73]   D. J. Pooler, "The temperature dependent non-linear response of a wood plastic composite," Washington State University, 2001.

[74]   M. L. Williams, R. F. Landel, and J. D. Ferry, "The temperature dependence of relaxation mechanisms in amorphous polymers and other glass-forming liquids," *Journal of the American Chemical Society,* vol. 77, pp. 3701-3707, 1955.

[75]   F. Schwarzl and F. Zahradnik, "The time temperature position of the glass-rubber transition of amorphous polymers and the free volume," *Rheologica Acta,* vol. 19, pp. 137-152, 1980.

[76]   I. Sher, B. Han, and A. Bar-Cohen, "Modified coupled-mode model for thermally chirped polymer Bragg gratings," *Applied optics,* vol. 49, pp. 2079-2084, 2010.

[77]   W. Van Driel, J. Janssen, G. Zhang, D. Yang, and L. Ernst, "Packaging Induced Die Stresses—Effect of Chip Anisotropy and Time-Dependent Behavior of a Molding Compound," *Journal of Electronic Packaging,* vol. 125, pp. 520-526, 2003.

[78]   M. Sadeghinia, K. Jansen, and L. Ernst, "Characterization and modeling the thermo-mechanical cure-dependent properties of epoxy molding compound," *International Journal of Adhesion and Adhesives,* vol. 32, pp. 82-88, 2012.

[79]   I. Emri and T. Prodan, "A measuring system for bulk and shear characterization of polymers," *Experimental mechanics,* vol. 46, pp. 429-439, 2006.

[80]   Y. Sun, Y. Wang, C. Jang, B. Han, and K. Choi, "Generalized Hybrid Modeling to Determine Chemical Shrinkage and Modulus Evolutions at Arbitrary Temperatures," *Experimental mechanics,* vol. 53, pp. 1783-1790, 2013.

[81]   Y. Sun, Y. Wang, Y. Kim, and B. Han, "Dual-Configuration Fiber Bragg Grating Sensor Technique to Measure Coefficients of Thermal Expansion and Hygroscopic Swelling," *Experimental mechanics,* vol. 54, pp. 593-603, 2014.

[82]   P. Sun, V.-K. Leung, B. Xie, V. Ma, and D.-Q. Shi, "Warpage reduction of package-on-package (PoP) module by material selection & process optimization," in *Electronic Packaging Technology & High Density Packaging, 2008. ICEPT-HDP 2008. International Conference on*, 2008, pp. 1-6.

[83]   D. Karalekas, J. Cugnoni, and J. Botsis, "Monitoring of process induced strains in a single fibre composite using FBG sensor: A methodological study," *Composites part A: applied science and manufacturing,* vol. 39, pp. 1118-1127, 2008.

[84]   Y. Sun, H. Lee, and B. Han, "Measurement of Temperature-Dependent Elastic Constants of Epoxy Molding Compound by Fiber Bragg Grating Sensor Method," *Experimental Mechanics,* Submitted 2016.

[85]   N. Tanaka, Y. Okabe, and N. Takeda, "Temperature-compensated strain measurement using fiber Bragg grating sensors embedded in composite laminates," *Smart materials and structures,* vol. 12, p. 940, 2003.

[86]   M. Mulle, R. Zitoune, F. Collombet, P. Olivier, and Y.-H. Grunevald, "Thermal expansion of carbon–epoxy laminates measured with embedded FBGS–Comparison with other experimental techniques and numerical simulation," *Composites part A: applied science and manufacturing,* vol. 38, pp. 1414-1424, 2007.

[87]   L. Yu-Lung and C. Han-Sheng, "Measurement of thermal expansion coefficients using an in-fibre Bragg-grating sensor," *Measurement Science and Technology,* vol. 9, p. 1543, 1998.

[88]   N. A. David, P. M. Wild, and N. Djilali, "Parametric study of a polymer-coated fibre-optic humidity sensor," *Measurement Science and Technology,* vol. 23, p. 035103, 2012.

[89]   T. Yeo, D. Eckstein, B. McKinley, L. Boswell, T. Sun, and K. Grattan, "Demonstration of a fibre-optic sensing technique for the measurement of moisture absorption in concrete," *Smart materials and structures,* vol. 15, p. N40, 2006.

[90]   M. Harsch, J. Karger-Kocsis, and F. Herzog, "Monitoring of cure-induced strain of an epoxy resin by fiber Bragg grating sensor," *Journal of applied polymer science,* vol. 107, pp. 719-725, 2008.

[91]   H.-I. Kim, J.-S. Yoon, H.-B. Kim, and J.-H. Han, "Measurement of the thermal expansion of space structures using fiber Bragg grating sensors and displacement measuring interferometers," *Measurement Science and Technology,* vol. 21, p. 085704, 2010.

[92]   V. Murukeshan, P. Chan, L. Ong, and L. Seah, "Cure monitoring of smart composites using fiber Bragg grating based embedded sensors," *Sensors and Actuators A: Physical,* vol. 79, pp. 153-161, 2000.

[93]   M. Lai, J. Botsis, J. Cugnoni, and D. Coric, "An experimental–numerical study of moisture absorption in an epoxy," *Composites part A: applied science and manufacturing,* vol. 43, pp. 1053-1060, 2012.

[94]   W. W. Morey, G. Meltz, and W. H. Glenn, "Fiber optic Bragg grating sensors," in *OE/FIBERS'89*, 1990, pp. 98-107.

[95]   A. D. Kersey, M. A. Davis, H. J. Patrick, M. LeBlanc, K. Koo, C. Askins, M. Putnam, and E. J. Friebele, "Fiber grating sensors," *Journal of lightwave technology,* vol. 15, pp. 1442-1463, 1997.

[96]   K. O. Hill and G. Meltz, "Fiber Bragg grating technology fundamentals and overview," *Journal of lightwave technology,* vol. 15, pp. 1263-1276, 1997.

[97]   R. Gafsi and M. A. El-Sherif, "Analysis of induced-birefringence effects on fiber Bragg gratings," *Optical Fiber Technology,* vol. 6, pp. 299-323, 2000.

[98]   Y. Sun, Y. Wang, Y. Kim, and B. Han, "Dual-Configuration Fiber Bragg Grating Sensor Technique to Measure Coefficients of Thermal Expansion and Hygroscopic Swelling," *Experimental mechanics,* pp. 1-11, 2013.

[99]   Y. Eom, L. Boogh, V. Michaud, P. Sunderland, and J. A. Månson, "Time-cure-temperature superposition for the prediction of instantaneous viscoelastic properties during cure," *Polymer Engineering & Science,* vol. 40, pp. 1281-1292, 2000.

[100]   M. Costa, E. Botelho, and M. Rezende, "Monitoring of cure kinetic prepreg and cure cycle modeling," *Journal of materials science,* vol. 41, pp. 4349-4356, 2006.

[101]   M. L. Gasperi, "Life prediction model for aluminum electrolytic capacitors," in *Industry Applications Conference, 1996. Thirty-First IAS Annual Meeting, IAS'96., Conference Record of the 1996 IEEE*, 1996, pp. 1347-1351.

[102]   E. Parsa, H. Huang, and A. Dasgupta, "Multi-physics simulations for combined temperature/humidity loading of potted electronic assemblies," *Microelectronics Reliability,* vol. 54, pp. 1182-1191, 2014.

[103]   N. Kinjo, M. Ogata, K. Nishi, and A. Kaneda, "Epoxy molding compounds as encapsulation materials for microelectronic devices," in *Speciality Polymers/Polymer Physics*, ed: Springer, 1989, pp. 1-48.

[104] Y. Sun, H. Lee, and B. Han, "Comprehensive Viscoelastic Analysis of Advanced Epoxy Molding Compound: Experimental Characterization and Modeling," *Submitted,* 2016.

[105] X. Tao, L. Tang, W.-c. Du, and C.-l. Choy, "Internal strain measurement by fiber Bragg grating sensors in textile composites," *Composites Science and Technology,* vol. 60, pp. 657-669, 2000.

[106] I. Prigogine, "Introduction to thermodynamics of irreversible processes," *New York: Interscience, 1967, 3rd ed.,* vol. 1, 1967.

[107] P. Procter and J. Solc, "Improved thermal conductivity in microelectronic encapsulants," in *Electronic Components and Technology Conference, 1991. Proceedings., 41st*, 1991, pp. 835-842.

[108] L. C. Brinson, "Time-temperature response of multi-phase viscoelastic solids through numerical analysis," California Institute of Technology, 1990.

[109] W. G. Knauss and I. Emri, "Volume change and the nonlinearly thermo-viscoelastic constitution of polymers," *Polymer Engineering & Science,* vol. 27, pp. 86-100, 1987.

[110] W. Knauss and W. Zhu, "Nonlinearly viscoelastic behavior of polycarbonate. I. Response under pure shear," *Mechanics of Time-Dependent Materials,* vol. 6, pp. 231-269, 2002.

[111] W. G. Knauss and I. Emri, "Non-linear viscoelasticity based on free volume consideration," *Computers & Structures,* vol. 13, pp. 123-128, 1981.

[112] H. Dal and M. Kaliske, "Bergström–Boyce model for nonlinear finite rubber viscoelasticity: theoretical aspects and algorithmic treatment for the FE method," *Computational Mechanics,* vol. 44, pp. 809-823, 2009.

[113] D. B. Adolf, R. S. Chambers, and J. M. Caruthers, "Extensive validation of a thermodynamically consistent, nonlinear viscoelastic model for glassy polymers," *Polymer,* vol. 45, pp. 4599-4621, 2004.

[114] Y. Wang, N. Chen, B. Yun, Z. Wang, C. Lu, and Y. Cui, "Effects of distributed birefringence on fiber Bragg grating under non-uniform transverse load," *Optics & Laser Technology,* vol. 40, pp. 1037-1040, 2008.

[115] K. J. Kim, A. Bar-Cohen, and B. Han, "Thermo-optical modeling of polymer fiber Bragg grating illuminated by light emitting diode," *International Journal of Heat and Mass Transfer,* vol. 50, pp. 5241-5248, 2007.

[116] E. Stellrecht, B. Han, and M. G. Pecht, "Characterization of hygroscopic swelling behavior of mold compounds and plastic packages," *Components and Packaging Technologies, IEEE Transactions on,* vol. 27, pp. 499-506, 2004.

[117] E. Stellrecht, B. Han, and M. Pecht, "Measurement of the hygroscopic swelling coefficient in mold compounds using moiré interferometry," *Experimental Techniques,* vol. 27, pp. 40-44, 2003.

[118] C. Jang, S. Yoon, and B. Han, "Measurement of the hygroscopic swelling coefficient of thin film polymers used in semiconductor packaging," *Components and Packaging Technologies, IEEE Transactions on,* vol. 33, pp. 340-346, 2010.